2017

Degradation Resistant Surface Enhanced Raman Spectroscopy Substrates

Ryan D. Scherzer
University of North Florida

Degradation Resistant Surface Enhanced Raman Spectroscopy Substrates

By

Ryan Dale Scherzer

A Thesis submitted to the Department of Mechanical Engineering

In partial fulfillment of the requirements for the degree of

Master of Science in Mechanical Engineering

UNIVERSITY OF NORTH FLORIDA

COLLEGE OF COMPUTING ENGINEERING AND CONSTRUCTION

August 2017

This Thesis titled Degradation Resistant Surface Enhanced Raman Spectroscopy Substrates is approved:

_____   _____

Dr. Stephen Stagon

_____   _____

Dr. Paul Eason

_____   _____

Dr. Lev Gasparov

Accepted for the Mechanical Engineering Department:

_____   _____

Dr. Murat Tiryakioglu
Director

Accepted for the College of Computing, Engineering, and Construction:

_____   _____

Dr. Mark Tumeo
Dean

Accepted for the University:

_____   _____

Dr. John Kantner
Dean of the Graduate School

DEDICATION

This thesis is dedicated to memory of Nancy Scherzer

and to my friends and family

for their love and support through this adventure.

ACKNOWLEDGMENTS

TABLE OF CONTENTS

Page

LIST OF TABLES

LIST OF FIGURES

ABSTRACT

Raman spectroscopy is employed by NASA, and many others, to detect trace amounts of substances. Unfortunately, the Raman signal is generally too weak to detect when very small, but non-trivial, amounts of molecules are present. One way around this weak signal is to use surface enhanced Raman spectroscopy (SERS).

When used as substrates for SERS, metallic nanorods grown using physical vapor deposition (PVD) provide a large enhancement factor to the Raman signal, as much as 10^{12}. However, Silver (Ag) nanorods that give high enhancement suffer from rapid degradation as a function of time and exposure to harsh environment. Exposure to harsh environments is an enormous issue for NASA; considering all environments experienced during space missions will be drastically different from Earth regarding atmosphere pressure, atmosphere composition, and environmental temperature. Au and Ag nanorods suffer from a thermochemical kinetic phenomenon where the surface atoms diffuse and cause the nanostructures to coalesce towards bulk structure. When in bulk, SERS enhancement is lost and the substrate becomes useless.

A stable structure for SERS detection is designed through engineering the barriers to surface diffusion. Aluminum (Al) nanorods are forced to undergo surface diffusion through thermal annealing and form rough mounds with a stable terminating oxide layer. When Ag is deposited on top of this Al structure, it becomes kinetically bound and changes to physical structure become impeded. Using this paradigm, samples are grown with varied lengths of Ag and are then characterized using scanning electron microscopy (SEM) and Ultraviolet-Visible spectroscopy. The performance of the samples are then tested using

SERS experiments for the detection of trace amounts of rhodamine 6G, a 'gold standard' analyte. Characterization shows the effectiveness of the Raman substrates remains stable up to 500°C.

Transitioning to basic scientific investigation, next is to strive to isolate the individual impacts of chemical and physical changes to the Ag nanostructure and how they affect the Raman signal. Substrates are compared over the course of a month long experiment to determine the effects of vacuum storage and addressing the effects of chemical adsorbance. Additionally, this was attempted by comparing the signal degradation of Ag nanorods to that of Au, which is known to be chemically inert, allowing for the separation of chemical and physical effects. Although Ag and Au have similar melting points, Ag physically coarsened significantly more. FTIR also showed significant chemical contamination of the Ag, but not Au. A hypothesis is proposed for future investigations into the chemical changes and how they are coupled with and promote the physical changes in nanostructures.

Overall, the novel SERS substrate engineered here may enable the detection of trace amounts of molecules in harsh environments and over long timescales. Conditions such as those found on space missions, where substrates will experience months or years of travel, high vacuum environments, and environments of extreme temperatures.

INTRODUCTION

The National Aeronautics and Space Administration (NASA) has been sending rovers to Mars to explore the surface and to look for signs of water and life. One of their top goals is to search the cosmos for concrete signs of life. Among the proposed methods is to have rovers perform surface enhanced Raman spectroscopy (SERS) on the planet surfaces, looking for organic molecules that signal the presence current or past life or the existence of the building blocks of life. However, this is currently impossible due to the degradation over time that traditional SERS substrates experience.

The overarching goal of this research has been to develop new technology for space missions, with the ultimate deliverable of providing NASA with guidance to develop a degradation resistant surface enhanced Raman spectroscopy substrate. The research performed in this thesis was sponsored by a grant from the National Aeronautics & Space Administration through the University of Central Florida's NASA FLORIDA SPACE GRANT CONSORTIUM and Space Florida, for the development of a SERS substrate that could be used during space missions, where they could experience high vacuum environments and extreme temperatures.

For this thesis, two approaches have been devised to use SERS in space or on remote celestial bodies: 1) produce substrates on site; 2) send manufactured substrates from Earth with the mission. Manufacturing substrates on site becomes a massive logistical problem, as it involves a massive amount of energy to produce the substrates through vaporization techniques. Energy is an important and heavily managed resource off of Earth. Unfortunately, the necessary energy is too great and the alternative is to manufacture

substrates on earth and send them, with the rest of the equipment, on the months to multiple yearlong travel. SERS substrates commonly used in literature do not fare well over long periods of time, or when they experience a temperature higher than ambient on Earth, approximated at 35°C. Additionally, the novel research in this thesis show that conventional SERS substrates also degrade under vacuum.

In this novel research, the first attempts to develop a degradation resistant SERS substrate utilized Aluminum (Al) nanorods. These substrates had a thin oxide layer on the surface that resisted the physical degradation mechanisms, but could not withstand extreme temperatures. They also proved to not be ideal SERS substrates as the Raman signal was drowned out by fluorescence. Annealing these substrates at 500°C for 24 hours led to extreme surface restructuring and the formation of a rough island film, which were named 'nanoseeds'; these are then utilized to engineer a surface structure to decrease surface mobility of additional metal deposited on top. The designed substrate consisted of the annealed Al seeds with additional Ag deposited on top. The intention was that the Al seeds prevent the coarsening of the Ag back into bulk by decreasing diffusion of the Ag through creating a rough path and increased surface area. The samples were then heated to 500°C to force the structures to a lower, more stable, energy state. As designed, the Ag remained as discreet nanoparticles and remained SERS active. After demonstrating that the structures could withstand elevated temperatures, the next problems to address were maintaining enhancement over extended periods of time and under vacuum using a custom, in-house built vacuum storage system. Both of these were addressed with a month long experiment comparing the storage of the substrates in air and under vacuum. Both methods

showed promising results, but still exhibit some decay in the Raman signal over the course of the month, although, the new engineered substrate faired 50% better than those in the literature.

A second portion of the work focused on gaining a new scientific understanding of the degradation of SERS substrates which employ nanomaterials. The final set of experiments was an attempt to determine if the loss in signal over the course of the previous experiments was a result of a chemical degradation or a physical one. This final experiment involved a month-long study comparing Ag nanorods and Au nanorods, which should be chemically inert, that were stored in air. The experiments showed that the Au nanorods remained chemically pure and undergo no observable physical changes while the Ag rods undergo both. As a result of this, a new hypothesis was formed, suggesting that the chemical and physical changes are coupled for Ag.

This thesis documents the research, experiments, and conclusions of the aforementioned studies. Chapters 1 through 3 begin with a brief introduction into the technique of Raman spectroscopy and explains the physics behind the Raman signal, which originates from the vibrations of the molecule under investigation and light scattering. Next, the physics behind the surface enhancement phenomena is explained. Finally, the physical review lands on the definition of electromagnetic enhancement and provides an in depth look at its cause, the physical phenomena known as surface plasmon resonance.

The Chapters 4 and 5, which bridges from background to the novel research presented by this thesis. The second section covers the substrates traditionally used in SERS and their major shortcomings, specifically the physical degradation observed in

literature. Additionally, some of the alternative methods devised in the literature to overcome the physical degradation issues are reviewed. Section two then leads into the classical fabrication of SERS substrates with physical vapor deposition, how nanorods are grown through glancing angle deposition, and the characterization techniques used to analyze the substrates produced in the presented research.

Finally, Chapter 6 presents the novel research of this study. In Chapter 6, a new degradation resistant SERS substrates and the respective characterization is presented. This engineered substrate began with the use of annealed Al nanorods as a base to promote morphological stability and enforce degradation resistance. Next, varied amounts of SERS active Ag are deposited and characterized. Testing was then performed, measuring their resilience to surface diffusion by annealing the entire sample in air. Next, the structure's performance was put to the test through a month-long experiment of storing substrates under vacuum and in ambient to determine effectiveness of vacuum storage and the effects of chemical adsorption on the Raman signal. Moving onto the second, and more scientific experiment, Ag and Au nanorods were fabricated and had their physical and chemical stability characterized and performance as SERS substrates measured over the course of 28 days.

CHAPTER 1: RAMAN SPECTROSCOPY

Raman spectroscopy is a useful, nondestructive characterization technique that measures the scattering of light of a monochromatic laser after interactions with an analyte molecule. The scattered light is what makes up the Raman signal produced through Raman spectroscopy. A majority of the variations in Raman spectroscopy follow the same method of measuring a monochromatic light scattering off the analyte.

There are numerous methods/variations of Raman Spectroscopy: Raman Spectroscopy (RS), Surface Enhanced Raman Spectroscopy (SERS), Surface Enhanced Resonant Raman Spectroscopy (SERRS), Tip Enhanced Raman Spectroscopy (TERS) [1], BiAnalyte Raman Spectroscopy (BiASERS) [2], Single Molecule (SMSERS) [3], and many others. In most cases, these are just variations to the method of gathering data, or to the analyte being observed. Conventional Raman spectroscopy has been used in chemistry, physics, and engineering for many decades. More recently, more development has gone into SERS, where the molecule being observed is on a surface that is able to enhance the scattering effect through various phenomena called Surface Enhancements (SE) [4]. All types of all Raman spectroscopy are performed using a monochromatic light source, an analyte molecule, the substrate the molecule is on, and a photodetector. [4]

The wavelength and power of the light source are chosen depending on the molecule being observed and the desired effects. [4, 5] Typical wavelengths are in the visible spectrum, with the most recent literature using wavelength of 532nm [6]. Less commonly used wavelengths reach into the ultraviolet for various applications such as ultraviolet resonant molecules or substrates [7-12]. If the wavelength is tuned correctly the

molecule can resonate with the light's frequency, this effect is utilized is resonant Raman spectroscopy methods [4]. As for the power, a stronger source will lead to a stronger signal, but it can cause the destruction of the analyte or even degradation of the enhancing surface [4, 5]. Typically the power measured at the substrate with a laser power meter and is measured at the microwatt to milliwatt range.

The most important part of Raman spectroscopy is the analyte being observed, considering the purpose of performing Raman spectroscopy is to observe a molecule. Every molecule will exhibit its own unique Raman signal as the Raman scattering is related to the molecules' shape and chemical bonds; this relationship will be discussed in depth in a later section. Nearly every molecule can be observed and identified through Raman spectroscopy. There are a few exceptions, where the Raman signal is overpowered by fluorescence, the signal is too weak to read, measure effectively, or the analyte is too unstable to withstand the environment or irradiation necessary to measure it. Another important exception is molecule with an inversion center symmetry. Most of the vibrational modes will be both Raman and infrared active. However, modes involving inversion center will exhibit Raman activity or infrared activity, not both. [4-6, 13-16].

The second most important aspect of Raman spectroscopy is the surface the analyte molecule is on and its surrounding medium, since the interactions between the incident light, surface, and molecule is the source on the signal enhancement [4-6].

Typical Raman Spectroscopy Setup

Figure 1 shows a typical Raman spectroscopy setup. If we follow the photons used in Raman spectroscopy, we start at a light source emitting photons of a single wavelength. In the literature, most labs use a solid state laser (532nm) as they are relatively inexpensive and readily available. The photons from the laser interact with the molecule and substrate's surface, leading to events called "scattering". The incident photons can either remain at the same energy level that they started at, or gain/lose some energy [4, 5, 7, 8]. If a photon changes its energy level, its wavelength and associated "color" change as well. A majority of the photons are unchanged (90-99%), this leads to a typically weak signal from the scattered photons [5]. Possible scattering events are Raleigh (elastic), scattering where the photons leave with no net change in energy or Stokes/Anti-Stokes (inelastic) scattering [5]. The Raman spectrometer then filters out the Raleigh scattered light and spreads the Stokes scattered photons with a diffraction grating. Then a charged coupled device (CCD) measures the number of photons at each of the scattered wavelengths [5]. The signal produced by the spectrometer is measured in arbitrary units as counts per wavenumber; this is proportional to the number of photons that have been shifted to different wavelengths [4, 5].
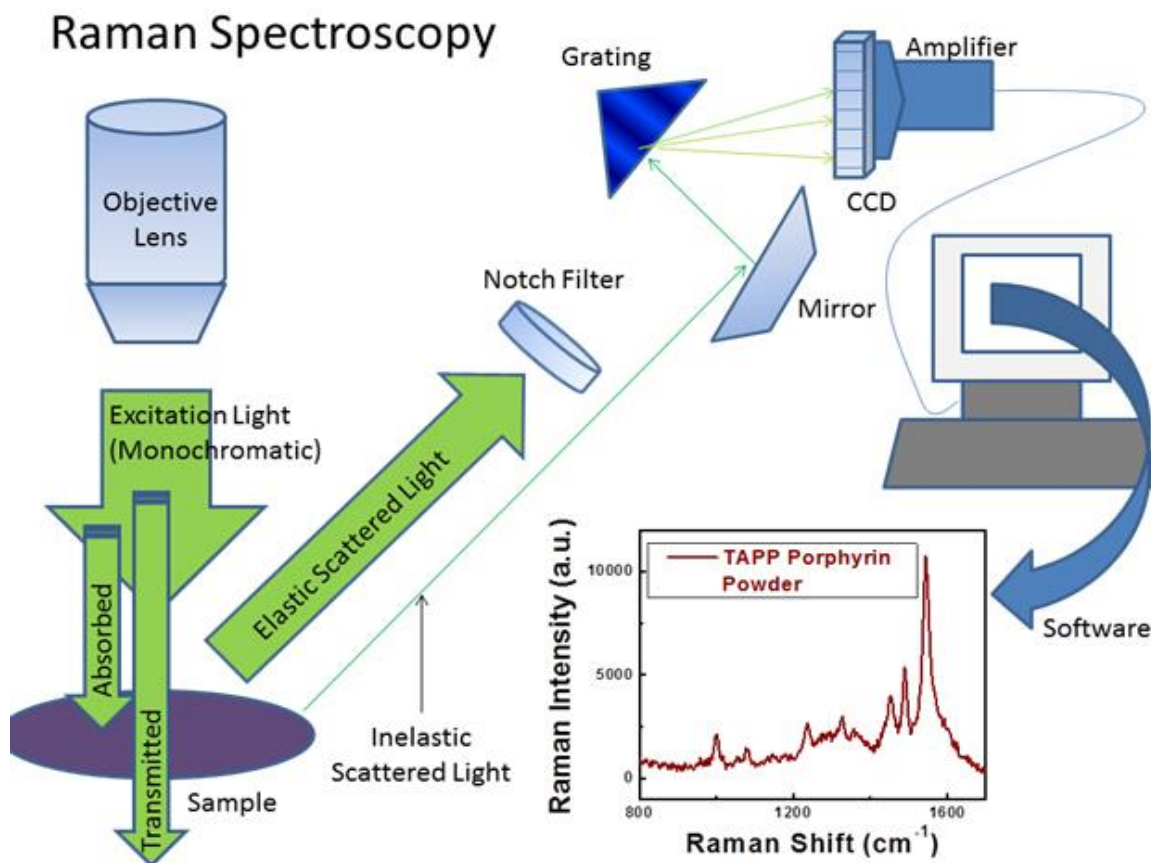
Figure 1: Raman Spectroscopy Photon Path [9]

Applications

Raman spectroscopy has plentiful applications, including chemical detection, biomolecule sensing [7, 9, 13-15, 20-22], single molecule detection [2,14,16, 18, 23-28], monitoring of chemical reactions [10], detection of chemicals in water and soil [11], tumor detection [12], and many more.

Comparison to FTIR/Fluorescence Spectroscopy

There are spectroscopy techniques other than Raman spectroscopy. Some of the commonly used techniques are Fourier Transform Infrared (FTIR) and fluorescence spectroscopy [4, 5]. While similar to each other, there are some key differences between them [4, 5]. Where Raman uses a molecules polarizability and molecular vibrations to measure the wavelength shift in scattered light, FTIR uses changes in dipole moment and measures the wavelengths absorbed by the molecule [4, 5]. One of the downsides to FTIR that Raman can accomplish is distinguishing between single, double, and triple bonds between atoms [4, 5]. On the other hand, Raman signals can be lost due to fluorescence and FTIR is not affected by fluorescence [4, 5].

Another technique is fluorescence spectroscopy. Fluorescence and Raman look almost the same when comparing the physics behind their respective phenomena [4, 5]. Both involve the interaction of a molecule and an incident photon, then a change in energy of the photon [4, 5]. The difference between them is what happens to the photon. In Raman, the photon imparts some of its energy into the molecule and leaves at a different energy level [4, 5]. In fluorescence the photon is absorbed into the molecule and re-emitted as a different energy level as the molecule relaxes back to ground state [4, 5].

Vibrational Modes

The observed peaks in the Raman signal are dependent on the analyte molecule [4, 5, 6]. When the monochromatic laser shines onto a molecule, it causes vibrational modes in the bonds between the atoms [1, 4]. The number of possible vibration modes is proportional to the number of atoms in the molecule (N), the number can be found using 3N-6. These modes are the molecular bonds/structures stretching, twisting, or bending towards and away from each other [1,4]. There can be hundreds of modes in a large molecule and each mode requires a specific amount of energy to be imparted into each bond [4]. The energy to cause these vibrations is taken from the incident photons, causing the inelastic scattering observed during Raman spectroscopy [4]. As each vibrational mode requires a specific amount of energy and the incident light is monochromatic, the scattered wavelengths of light and their intensities (Raman peaks) can be associated to a specific vibrational mode(s) [4].

Assigning a molecule's Raman peaks to vibrational modes can be a very involved process, becoming increasingly arduous as the molecule becomes larger and more complex [1]. The method to calculate assignments is to use high-level density functional theory (DFT) calculations and back them up with experimental values using IR and Raman Spectroscopy [1, 4]. In short, DFT is a mathematical model used to simulate the electronic structure of atoms and molecules. The entire process of assigning vibrational modes and Raman peaks is very complex and it is necessary to use computational programs to perform the quantum chemical calculations for large, complex molecules [1, 4]. One journal article, [1], walks through the steps they took to calculate vibrational assignments for the

commonly used Raman analyte, Rhodamine 6G. Rhodamine 6G has the empirical name of {xanthylium,9-[2-(ethoxycarbonyl)phenyl]-3,6-bis-(ethylamino)-2,7-dimethyl-,chloride}, but is commonly referred to as R6g or Rh6g [1]. This molecule is commonly used to test the effectiveness of SERS substrates as it has been extensively studied in literature, readily available, and inexpensive.

The initial step is to calculate the molecular structure of the molecule, specifically the bond lengths and angles found in the molecule to gain an understanding of the molecules structure in 3-dimensions [1]. These calculations are performed by the DFT program [4]. The program uses a rough estimate for the atomic locations, in Angstroms, as an input [4]. It then goes through a "geometry optimization" algorithm. The program finds the lowest energy states for the atoms based on their location and outputs the optimized locations for the atoms, this is a tedious iterative process [4]. If the geometry is not optimized correctly the vibrational calculations can result in a negative frequency [4].

Second, all possible modes of vibration the molecule can exhibit are calculated numerically, this includes bonds stretching, folding, twisting, and bending in all possible combinations, the rings breathing, beating, stretching, and twisting [1]. The various vibrational modes of the rings are differences in the timing and direction of the different atoms in the ring. For example, all of the atoms can be vibrating towards the center and away at the same time (beating), or the atoms can be moving in the opposite direction from the neighboring atoms (breathing). Generally, the number of possible vibrational modes is 3N-6 where N is the number of atoms in the molecule. R6G has 65 atoms and 189 possible vibrational modes. Some of the vibrational modes have similar vibrational

frequencies and will contribute to the same Raman peak, while others are often ignored due to having frequencies too far from the range being observed [1].

The next step is to calculate the energy required for each individual vibrational mode and compare to observed IR and Raman Spectra. Some of the vibrational modes can only be observed in IR or Raman, not both [1]. Some of the modes cannot be observed at all, even though values for IR and Raman appear in calculations, this would be because some of the vibrational modes do not provide enough of a discernable signal are drowned out by the background noise of the experiment or by fluorescence [1]. Calculated values for various vibrational modes of R6G that were provided by Watanabe can be found in Appendix A.

Additionally, the spectral response observed is affected by the resonance conditions of the experiment, and even molecule/surface interactions [1]. An example of the resonance condition effects can be seen in Figure 2. Large changes in specific Raman bands or even the appearance of new bands can occur when incident irradiation causes the electrons to become excited and transition between different electron states [1]. This is heavily dependent on the matching of the incident wavelength and the frequency of resonance.
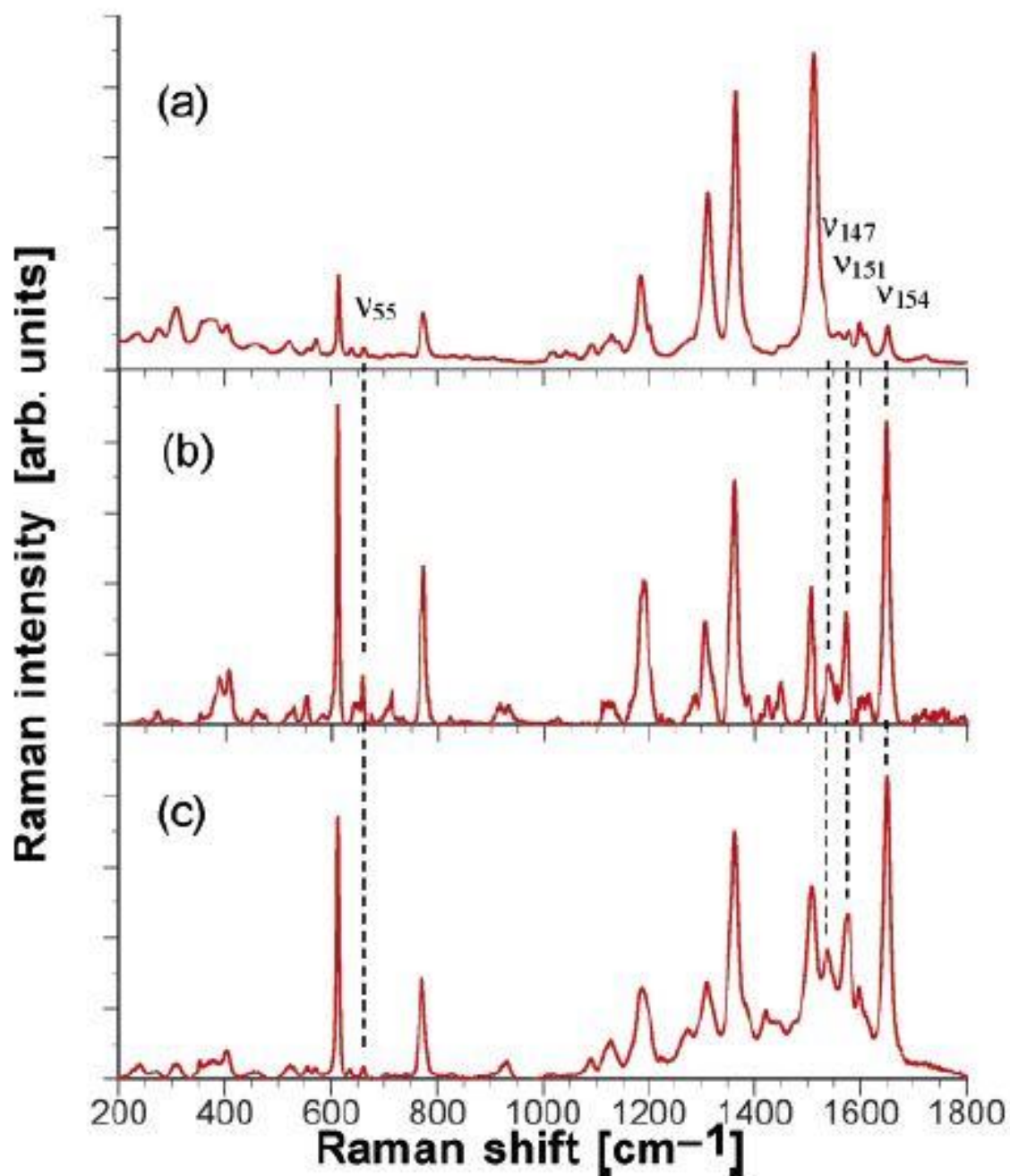
Figure 2: Raman spectra of R6G with different resonance scenarios. a) off resonance at 1064nm, b) resonance Raman scattering at 488nm, c) surface-enhanced resonance Raman scattering at 488nm on colloidal Ag. Various vibrational modes are depicted (v_x) [1].

Light Scattering

When a photon interacts with a molecule or surface, it can either be transmitted, reflected/scattered, or absorbed [4, 5]. The scattering/reflection can involve the gain or loss of energy, or the conservation of energy within the photon, depending on the elasticity of the interaction [4, 5]. Figure 3 shows a visualization of the change of energy level during scattering. While most of the incident photons are elastically scattered, or just reflected without any change in energy, it is the in-elastically scattered photons that are important to Raman spectroscopy [4, 5]. The Raman signal is comprised of the number of photons that have been scattered to different wavelengths by interactions with the molecule and substrate [4, 5]. What causes the change in wavelength is a change in energy of the incident photon [4, 5].

Just like in conventional dynamics, there is the conservation of energy and conservation of momentum. During inelastic collisions between objects, energy and momentum are transferred between the objects. The same happens when photons interact with the SERS substrate and analyte molecules [4, 5]. Some of the energy of the incident photon is transferred to the molecule, causing an excitement in the electrons of the molecule, which in turn cause various vibrational modes to occur [4, 5].

The electron excitement is equivalent to the energy change in the incident photon [4, 5]. The specific amount of energy exchanged depends on the specific vibrational mode the photon induces [4, 5, 1]. This leads to the formation of virtual energy states in the electrons, where they have more energy than their ground state, but not enough to raise to higher orbital. This extra energy is what causes the vibration of the molecule to occur [4,

5]. The virtual energy state forces the atomic bonds to slightly stretch and relax repeatedly while being bombarded with the incident radiation [4, 5].

When scattering happens under resonant conditions, the molecule is in an electromagnetic field enhanced by the surface plasmon resonance (SPR) phenomena. SPR is the oscillation of free electrons of the surface and induces a stronger electromagnetic field at the substrate's surface. When under resonant conditions, the molecule's electrons can transition to higher energy states. The resonant conditions allow for more scattering and more intense vibrational modes to form, leading to a much stronger, or enhanced, Raman signal [4, 5].
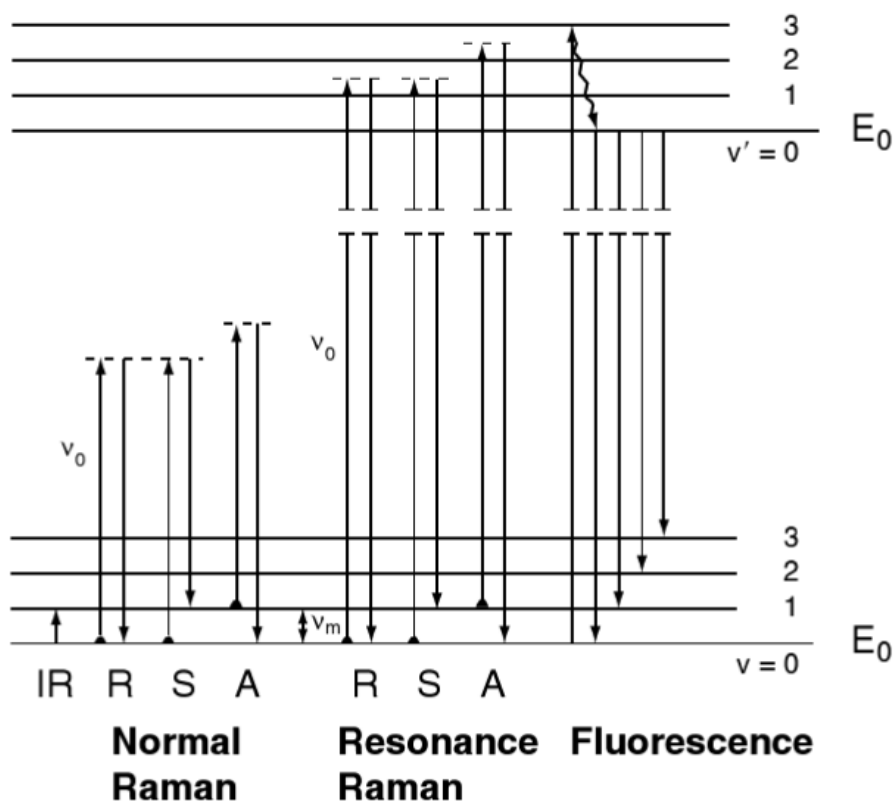
Figure 3: Energy Levels of Raman Scattering. Changes in electron energy level for interactions with Infrared (IR), Rayleigh (R), Stokes (S), and Anti-Stokes (A) scattering. Differences between Normal Raman, Raman with Resonance effects, and Fluorescence are pictured [4]

This entire process is complex to begin with, but becomes even more complex when the interactions between the scattered light and the enhancing surface are considered [4, 5]. Figure 4 is a simplified depiction of these interactions. Some of the photons are absorbed by the surface and induce a localized surface plasmon resonance, which in turn increases the amount of scattering that occurs by increasing the molecule's apparent Raman cross section [4, 5]. This entire process becomes even more complex as the scattered photons can then interact with the SERS surface and be absorbed, or reflected off of the surface and interact with the molecule again [4, 5].
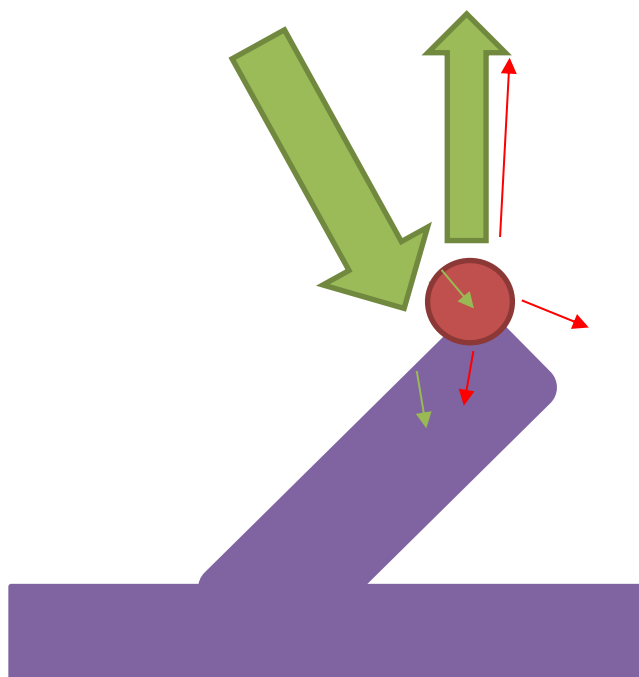
Figure 4: Not to scale representation of the interactions between the incident light, scattered light, and a surface (purple)/molecule (Dark red circle). Large green arrows are the incident and Rayleigh (Elastic) scattered light. Small green arrows are incident light absorbed by the molecule/surface. Small red arrows are the Stokes and Anti-Stokes (Inelastic) scattered light, some of the light is absorbed by the surface or emitted away from the detector.

CHAPTER 2: SURFACE ENHANCEMENT

Raman spectroscopy can attribute its versatility and strong signals to a group of phenomena called surface enhancement (SE) [2, 4-6, 23, 31-34]. SERS is aptly named for the increase in magnitude of the Raman signal that originates from the molecules interactions with the surface it rests on. This enhancement effect can be observed when the substrate is a rough surface with nano and/or micro scale features [4, 13, 14]. The cause of this enhancement effect has been heavily disputed since its discovery and was initially attributed to more molecules resting on the increased surface area of the rough surface [4, 6]. This postulation was thrown out and replaced with the observation of increased photon scattering cross section of the molecules [4, 6]. With this change came a proposal for single molecule detection [3,4]. The enhancement phenomena is still not fully understood, and theoretical maximum enhancement factors are said to be anywhere from 10^4 to 10^{14} from the combination of molecule resonance, surface resonance, and molecule/surface interactions. [4, 5] There is also the idea of a chemical enhancement originating from direct interactions between the molecule and the surface [4].

Almost all of the literature concurs that the enhancement effect is predominantly from electromagnetic effects, with only a small portion believing that a chemical effect is also present. This electromagnetic enhancement arises from a combination of interactions from the exciting, or incident, electromagnetic field and the re-emitted, or Raman field [2, 4].

The enhancement effects are complex and rely on a large number of variables: the wavelength, polarization, and incident angle of the excitation laser, the material, geometry,

orientation, and surround medium of the substrate, the different Raman vibrational modes of the analyte molecule, and the adsorption efficiency, concentration, distance from the surface, and the orientation of the analyte molecule [2, 4, 5, 31, 33, 36]..

The Various Methods of Reporting Enhancement Factors

There seems to be a significant amount of controversy and lack of standardization in the SERS field, from acronyms and names for phenomena and techniques, to how to report the findings, as seen in many of the references[2, 5, 7-15, 20-30, 33, 37-49]. One important example is the method of determining and reporting enhancement factors. There are many reported means of determining the enhancement factor of Raman substrates, but there are two main methods, both of which have multiple ways to calculate the measurements [4]. The two methods of measuring the enhancement factor of a substrate is to average the enhancement over the entire substrate or as a "single molecule" enhancement factor (SMEF) taken at a single point on the surface [4]. Some of the methods of reporting enhancement factor in literature are:

- An analytical EF (AEF), comparing the intensity of the Raman signal on the SERS substrate to the intensity of the signal in the surround medium without the SERS substrate [4].

- The SERS Substrate EF (SSEF), which compares the SERS intensity per average number of molecules adsorbed on the surface to the Raman intensity per the average number of molecules in the scattering volume [4].

- Orientation-averaged SMEF (OASMEF), which is an averaged multiple single molecule measurements at all possible molecule orientations [4].

- Polarization-Averaged SSEF (PASSEF), taking an average enhancement over different incident polarizations [4].

- The standardized SMEF (StdSMEF), which requires the analyte molecule to have an isotropic Raman tensor and to exhibit no chemical enhancement [4].

Even with so many methods of finding a substrate's enhancement factor, it still heavily depends on numerous variables, such as the number of molecules adsorbed, the orientation of the molecules, and the location of the molecule on the nanostructure [2, 4]. This makes it difficult to exactly replicate the experimental conditions and thus difficult to compare different substrates by their enhancement factor.

To summarize, enhancement factors for experiments cannot be compared unless substrates can be manufactured to have exact geometry, molecules can be adsorbed in the same known orientation, all other parameters can be kept similar between non-SERS, and SERS experiments, and non-SERS measurements are performed correctly. One method to get around this and to compare effectiveness of substrates is to compare their signal-to-noise ratio, a comparison between the magnitude of Raman peaks and the background noise. This looks at how strong the measured signal is compared to the background noise, allowing different substrates to be compared without involving the complex enhancement factor [2, 4].

Electromagnetic Enhancement

The most important aspect of surface enhanced Raman spectroscopy is the electromagnetic enhancement effect [31]. In Raman spectroscopy, the analyte molecule sits on the enhancing surface and both are irradiated with an incident electromagnetic field, usually visible light [31]. When a molecule is excited by an electromagnetic field of a specific frequency, the field induces a dipole in the molecule that oscillates at the same frequency of the field, this is visualized in Figure 5 a [31]. This oscillation will radiate power proportional to the incident power, an example is seen in Figure 5 b [31]. What happens during the surface enhancement phenomena is modification to the electromagnetic field (local field enhancement), modification to the radiative properties of the dipole molecule (radiation enhancement), and the possibility of modification to the polarizability of the molecule (chemical enhancement) [31].
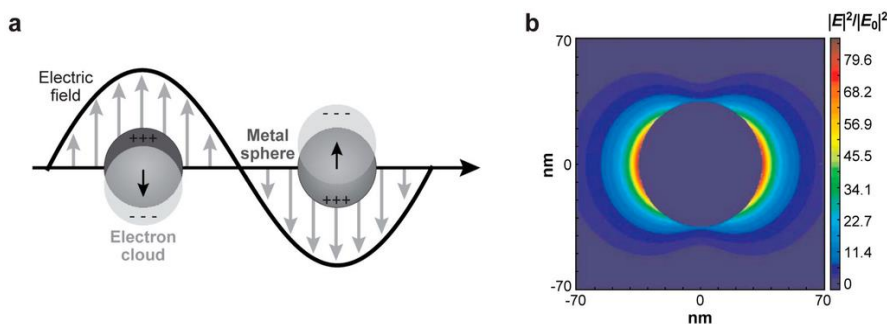
Figure 5: Electromagnetic Enhancement. a. The incident electromagnetic field induced a dipole in the molecule through the oscillation of the free electrons. b. depiction of the ratio between local induced electromagnetic field and the incident field. Stronger induced field is close to the surface. [5]

Local Field Enhancement

In literature, the most discussed enhancement effect is the local field enhancement $(M_{Loc}(\omega))$ [4, 5]. This effect is caused by the surface plasmon resonance of the substrate's

surface and can alter the electromagnetic field at the surfaced by orders of magnitudes when compared to the incident field [4, 5]. The difference between the local and incident fields is mainly determined by the frequency of the surface plasmon resonance [4, 5].

$$M_{Loc}(\omega) = \frac{|E_{Loc}(\omega)|^2}{|E_{Inc}|^2}$$

The local enhancement effect can also be enhanced even further by the gap effect, where the local field of two close surfaces interact and compound on each other [4, 5]. This leads to what are known as "hot-spots," or areas of significant field enhancements on a SERS substrate [4, 5].

Radiation Enhancement

An additional effect seen in surface enhancement is radiation enhancement (M_{Rad}), also known as modified spontaneous emission [4]. Spontaneous emission is when an excited electron relaxes to a lower energy state and releases the energy difference as a photon [4]. This extra energy comes from the oscillations in the dipole molecule [4]. As the molecule oscillates at a set amplitude depending on the incident wavelength, any additional energy adsorbed by the molecule is instantly reemitted [4]. In most real cases, the emitted radiation will interact with a surface and will be absorbed by the surface (non-radiative emission) or reflected [4]. Reflected emissions increase the amount of signal detected. However, if the molecule is within a few nanometers of the surface, the strong local electromagnetic field at the surface will modify the amount of energy the molecule experiences [4]. This can cause changes in the radiated power an excited dipole reemits in certain directions. The radiated power can either be enhanced or quenched, when

compared to power that would be radiated if the molecule was in free space instead of resting on an enhancing surface [4]:

$$M_{Rad} = \frac{P_{Rad}}{P_0}$$

Strangely, the radiation enhancement is not an effect on the emitted radiation, but is actually an effect on the emission process itself [4]. Some problems arise depending on the orientation/polarization of the dipole compared to the enhancing surface [4]. Since the radiative emission from the dipole is not isotropic in all directions, it is possible that the dipole does not radiate towards the Raman detector or it radiates towards the surface [4]. Depending on the surface material, the emitted radiation could be absorbed by the surface instead of ideally being reflected [4]. Therefore, if the dipole does not emit towards the detector, or the surface absorbs the radiation, it can appear that the electromagnetic field is quenched instead of enhanced [4].

Chemical Enhancement

The idea of a chemical enhancement comes from the possibility of the analyte molecule to chemically interact with the metallic surface forming something called a charge transfer [2, 4]. There are a few types of chemical enhancement situations: Type I is where there is no covalent bond between the molecule and surface, but the presence of the metal alters the electron distribution which in turn changes the polarizability of the molecule [2, 4]. Type II is a covalent bond (complex) or an electrolytic ionic bond between the molecule and surface which leads to significant changes to the molecules polarizability since the bond with the metal allows for new electron states to form [2, 4]. Finally, Type

III is a theory similar to type II where the energy difference between any two of the molecules highest occupied electron state (HOMO), lowest unoccupied electron state (LUMO), or the metal surfaces Fermi level is matched by the energy of the incident photon [2, 4].

Chemical enhancement is not thought to significantly contribute to the Raman enhancement [4]. Additionally, when chemical enhancement is observed the enhancement factor is usually on a scale of 10^1 [4]. When the compared to electromagnetic enhancement, which has been reported to be higher than 10^{10}, the chemical enhancement is insignificant to the overall enhancement [4].

CHAPTER 3: SURFACE PLASMON RESONANCE

Surface plasmons are thought to be the cause of many surface enhancement effects, however there is little literature exploring the surface plasmon phenomena in detail [2, 4]. Surface plasmons are usually described only as 'the oscillations of conduction band electrons', and without much more detail [2, 4] as seen in the following references: [12,15,17,29,31-36,40,50-55].

The available literature also uses a wide variety of terms to describe surface plasmons, making it difficult to accurately assess the current research on what is known/theorized about surface plasmons and their electromagnetic enhancement effects [2, 4]. In fact, referring to surface plasmons when talking about SERS is technically wrong. One must reference the type of surface plasmon formed at the enhancing surface. There are a number of different types of plasmons (Propagating, localized, radiating, non-radiating, bound, virtual, or evanescent) [4]; the type observed/formed depends on the incident conditions (incident angle of light, light wavelength, real and imaginary dielectric functions of the surface and surrounding medium, surface geometry) [4]. However, in the case of the nanostructures utilized in SERS, the surface plasmons formed are going to be localized due to the noncontiguous surface structure.

Surface Plasmons

The term surface plasmon arrives when looking at a metallic surface [36]. The free, conduction band electron 'cloud' at a metallic surface is considered a plasma and can

oscillate if excited [36].. To get a metallic surface's electrons to oscillate, they need to form as something called a plasmon-polaritron, this is when the plasmon is coupled to an incident photon [36]. The surface material must exhibit resonance with the incident light in order for a photon to couple with a plasmon [36]. The surface resonance happens when the real part of the dielectric function (ϵ') at the incident wavelength is approximately negative two times the dielectric constant of the surrounding medium [36]. This scenario allows the incident energy to be effectively stored in the surface material without dissipating rapidly, as the real part can be considered a materials ability to store incident energy and the imaginary part is the ability to dissipate the energy [36]. The intensity, or quality factor, of the resonance is dictated by the imaginary part of the surface's dielectric function [36].

Useful properties for plasmons are a real dielectric function value between -20 and -1 and a small imaginary dielectric function value or a quality factor greater than two. The higher the quality factor the better the material [36]. Figure 6 shows the real and imaginary parts of Au and Ag dielectric functions.
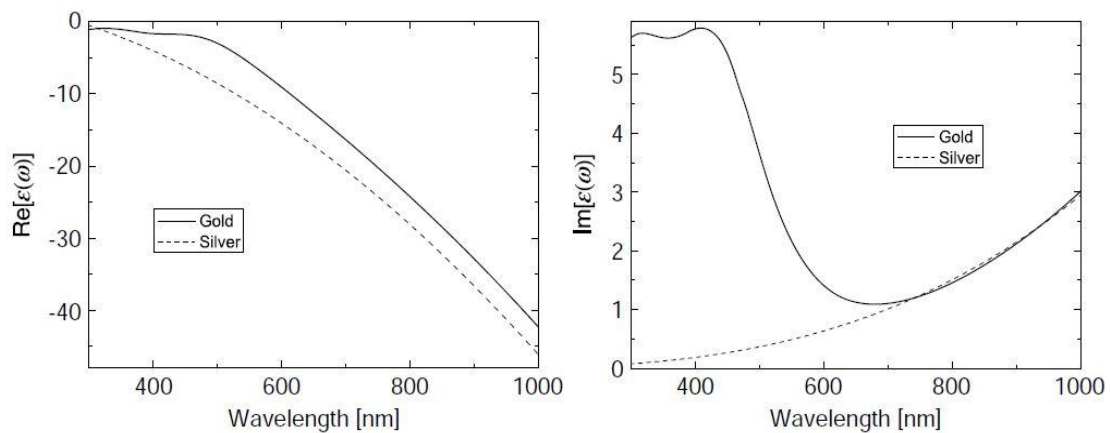
Figure 6: Real (left) and imaginary (right) parts of Ag and Ag dielectric functions [4]

Shape effects

In most real world cases of surface plasmons on a metallic surface there will not be a uniformity on the surface [4, 14, 15, 16]. With nano-sized features the surface plasmon propagation is disrupted and the electromagnetic modes can only exist at specific wavelengths as opposed to an existence at a continuous range of wavelengths on a perfect surface [4]. Additionally, when looking at the surfaces of nano-scale particles, their geometries affect the formation of plasmon resonance(s) [4, 14, 15, 16]. It is a good idea to start looking at a fully symmetric sphere; the diameter of the sphere affects the wavelength for surface plasmon resonance to form [4, 14, 15, 16]. The larger the radius, the more red shifted the wavelength becomes when comparing to a smaller sphere, additionally the absorption peak seen for the sphere broadens [4, 14, 15, 16]. This happens to a point where the sphere becomes useless as a SERS sensor as it absorbs most of the scattered radiation [4, 14, 15, 16]. Non symmetrical shapes become more complex as each different axis has a specific resonant wavelength [4, 14, 15, 16]. An easy way to visualize and approximate the resonance of relatively simple shapes such as ellipsoids and cylindrical shapes is to imagine they are a stretched sphere [41]. As a sphere is stretched along a single axis, its length along that axis is increased and thus resonance for that axis is red-shifted [41]. One way to think about how the resonance shifts for an axis during the stretching is: 'pointy ends' (prolate) lead to a red-shift and 'flat ends' (oblate) lead to blue-shift [41]. Figure 7 shows how the prolate or oblate features affect the resonance wavelength. Another effect is that the electromagnetic enhancement drastically increases

as an object becomes more prolated, meaning as the shape becomes sharper, the stronger

the resonance can be [41].
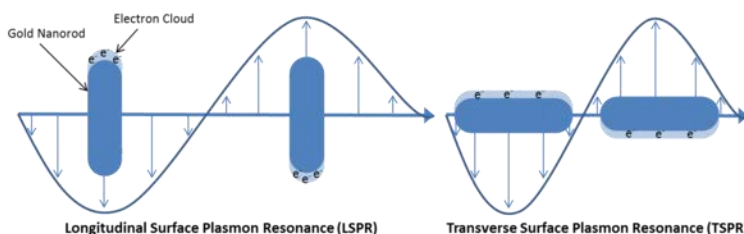
Figure 7: Surface Plasmon Resonance of Nanorods. The formation of transverse and longitudinal resonances require different wavelengths. The prolated longitudinal axis wavelength is red-shifted when compared to the oblated transverse axis [17].

Gap effect

Not only do the size and shape of the metallic particle affect its resonance and

electromagnetic enhancement, so does the presence of additional particles [55]. Figure 8

demonstrates the stronger electromagnetic field formed from the close proximity of

multiple particles. When two metallic surfaces are close to each other, their

electromagnetic enhancement fields interact with each other and form a hybridized

enhancement field and new local plasmon resonance [55]. These new plasmon

resonances are referred to as coupled-LSP and form from the coupling of the resonance

of the individual particles [55]. This hybridization is analogous to the hybridization of

atomic orbitals during covalent bonding [55]. The coupling of resonances leads to a red-

shift of the wavelength with the amount shifted depends on how strongly the two fields

interact with each other [55]. A very important variable in the coupling is the distance

between the particles [55]. Since their individual EM fields are stronger closer to the

surface, it makes sense that the closer the particles are the stronger the interaction will be [55].
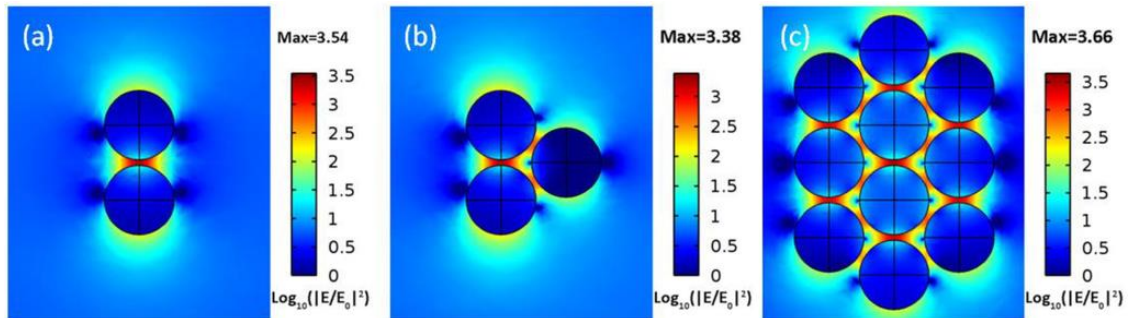
Figure 8: Depiction of the gap effect. As additional particles come into close proximity of each other, the localized electromagnetic field becomes stronger than a single particle [18].

Material effects

The most important variable in the formation of surface plasmons is the material the surface is made from and the surrounding medium [34]. More specifically these variables are: the value of the dielectric function for the surface at the wavelength being observed, dielectric constant of the surround medium, and their difference [34]. The importance of this difference comes from the circumstances necessary for nearly perfect absorbance at the specified wavelength. Normally, metals are almost perfect reflectors [34]. However, when the right wavelength of light is incident at the necessary angle at the boundary between the metallic surface and surrounding medium of the correct dielectric values, the energy of the incident photons will be coupled to the surface plasmons and form surface plasmon-polaritrons and resonate [34].

CHAPTER 4: TRADITIONAL SUBSTRATES

Since the discovery of the SERS phenomena, the most common substrates used have been Ag or Ag colloids, which are nano-scale metallic spheres suspended in solution [4]. As more labs researched Raman spectroscopy, other substrates were developed. Chemically roughened surfaces, nanostructures, metals other than Ag and Ag eventually made their way into the literature [4,33]

Traditionally, SERS substrates are made from Ag and Ag colloids because of the near ideal optical properties of the metals and the relative ease in fabricating a colloid solution [35]. These colloids are usually produced through a reduction reaction and stabilized with a stabilizing agent [33]. The most common reaction used is a citrate reduction, which provides its own stabilization agent [33]. The material used most in the literature is Ag [33]. . Even though Ag generally has a stronger enhancement, Ag is more stable, does not react as easily, and the binding mechanisms of Ag are more understood than Ag [33]. These all add up to the ease of attaching binding molecules to Ag particles making Ag a more versatile substrate for Raman spectroscopy [33].

Other planar substrates have also been used. Chemically roughened films, evaporative deposition, lithography techniques, and many other techniques have been used to fabricate planar or 2d Raman substrates [4]. These planar substrates remove the complexities of three dimensions and mixing dynamics that are found with colloidal solutions, and can be fabricated in ways to tightly control the size and shape of the surface [4].

Substrate Stability

This subsection will mainly consist of various papers on the broad subject of the stability of Raman substrates and some different phenomena that lead to Raman signal and substrate degradation. The two main types of stability are thermal and chemical stability. Various types of thermal stability include grain growth, residual stress relaxation, phase transitions, and diffusion processes [19] including effects from elevated temperatures, surface diffusion, and coalescence. Whereas, chemical stability refers to oxidation and chemical adsorption on the surface

Surface diffusion

One of the most obvious methods of degradation is the physical restructuring of a particle as it undergoes surface diffusion [20]. Observing nanoparticles with scanning electron microscopy (SEM), one can quantify particles change shape over the course of days or weeks [20]. They go through a process called surface diffusion, where the surface atoms freely move and reorder themselves in a lower energy state than they started at. In order to fully understand the process a nanoparticle goes through during surface diffusion, Link, et. al. irradiated Ag nanoparticles with femtosecond laser pulses [20]. The irradiation imparts energy into the nanoparticle, less than would be required to transition the metal to a liquid phase [20]. Link, et. al. observed that the slight increase of internal energy leads to the surface diffusion process, starting from internal point defects that propagate to planar defects and eventually the reordering to a lower surface energy structure as seen in Figure 9 [20].
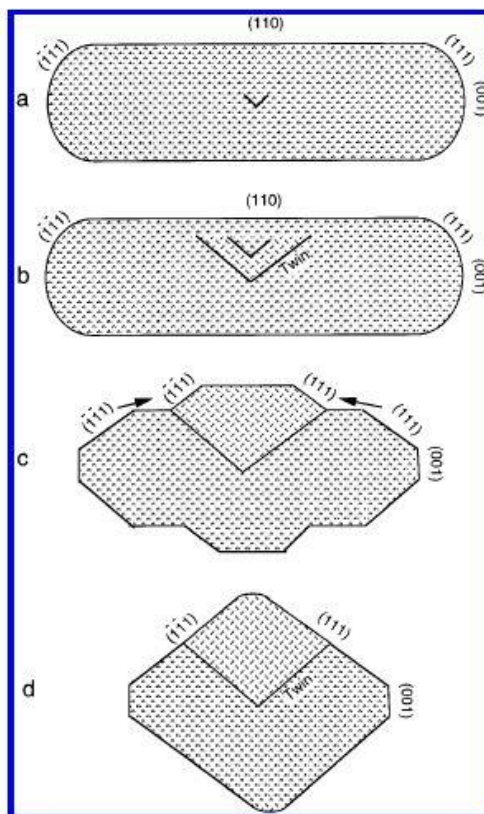
Figure 9: Crystal restructuring of Au nanorod. a) Point defect inside of nanorod. b) Point defect propagates to twin/stacking faults. c) Surface diffusion reorients crystal structure to propagate planar faults. d) Complete surface diffusion. [20]

Coalescence

In addition to surface diffusion, particles can undergo a coalescence process. Coalescence is where the particles aggregate and bind together [21]. Sometimes multiple particles may go through a process known as Ostwald ripening, where the smaller particles are absorbed into larger ones [21]. Two concurrent events that would lead to coalescence are surface diffusion which cause neighboring particles to touch and grow into each other. Or the particles detach from their substrate and undergo Brownian motion, random moving until they run into each other [21]. The particles touch and coalesce, driven by the desire to reduce their combined surface to volume ratio or their free surface energy [21]. While

the coalescence process is ideal from the thermodynamic standpoint, it requires some additional energy to initiate the process and to sustain the process [21]. After coalescence begins, some of the surface energy lost is used to sustain the process. However, as the number of atoms diffusing increases, the energy released cannot maintain the coalescence process [21]. Without a higher ambient temperature also feeding energy into the coalescence process, the particles can be left partial coalesced, such as in Figure 10 [21]
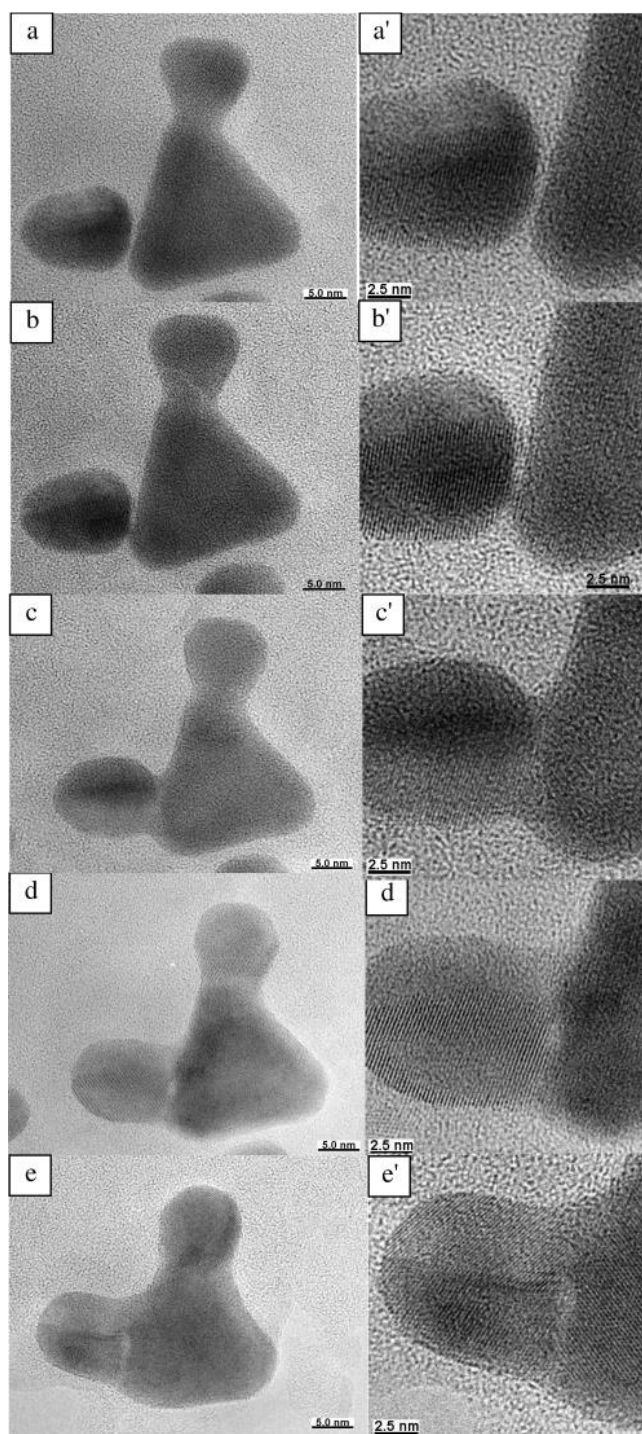
Figure 10: Yacaman, et al's TEM images depicting Au nanoparticles coalescing through Ostwald ripening, smaller particles are absorbed into the larger particle. Partial coalescence is depicted in image e. [21]

There becomes a relationship between the coalescence process and the shape of the particles involved [22]. As the coalescence process is driven by the desire to minimize surface energy, it makes sense that shapes with large surface to volume ratios or high energy crystallographic planar surfaces restructure faster. [22]

Oxidation

Chemical instability is another key downside to nanostructures. Due to their large surface to volume ratio, and their high amount of free surface energy, nanostructures can be very reactive [23]. This can prove to be detrimental to applications such as SERS. For the case of Ag, structures will oxidize up to 422K (~150°C) [23]. This temperature is where the partial pressure of O_2 at the Ag surface is close enough to the dissociation pressure of Ag_2O to allow decomposition of the O_2 and Ag. [23] Following this logic, lowering the pressure at the Ag surface would lower the temperature required for O_2 dissociation. [23]

Elevated Temperature

There is a commonality between all of these degradation methods; they are all thermo-chemical processes, meaning that the rate of which they occur is heavily related to the temperature during the process [24]. In one experiment by Beavers, et. al., a critical temperature for the degradation of Ag nanostructures was observed. In their experiments, the authors fabricated two kinds of substrates. The only difference between the substrates was a break in vacuum in-between fabrication steps [24]. To observe the effects of thermal

degradation, the team heated the substrates for a few minutes and observed any loss in Raman intensity [24]. Their findings show that the substrates exposed to O_2 in-between fabrication steps exhibit a significant loss in signal at only 60C for 5 minutes [24]. The substrates with no vacuum break during fabrication were able to withstand up to 100C for 30 minutes before a significant loss in Raman Signal [24]. However, as seen in Figure 11, heating these substrates to 125°C for 5minutes has a causes significant surface diffusion and signal loss; heating to 150°C for 5 minutes has extreme surface diffusion and a nearly complete loss of signal [24]. This critical degradation at 150°C coincides with the temperature of O_2 dissociation from Ag. It is a possibility that the presence of Oxygen on the surface significantly contributes to the surface degradation processes.
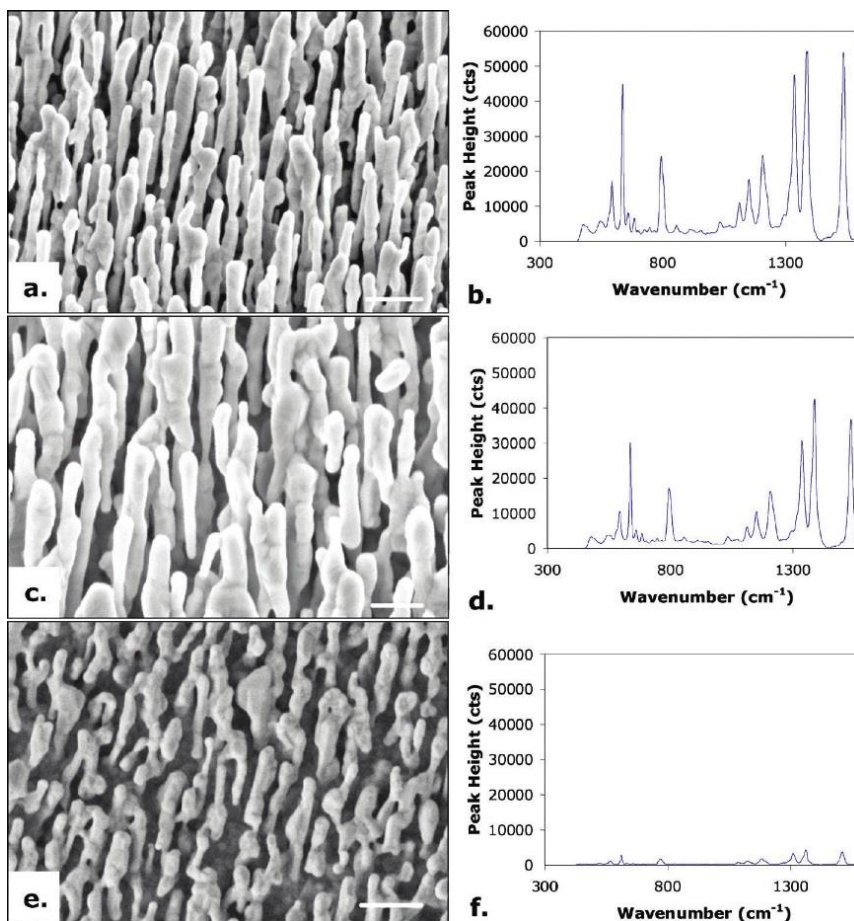
Figure 11: Surface Degradation of Ag nanorods due to elevated temperature. Before (a) and after (c) Ag nanorods are heated to 125°C for 5 minutes and their respective R6G Raman spectra (b, d). Ag nanorods heated to 150°C for 5 minutes (e) and R6G Raman spectrum (f) [24]

Attempts to minimize degradation

Many attempts have been made do stop the surface degradation of SERS substrates. Some attempts include coating Ag nanorods with a thin layer of Alumina (Al_2O_3) [25] or Titanium Oxide (TiO_2) [26]. These materials are stable to high temperature, and should theoretically block surface diffusion. Some have even attempted to use a purely Al nanorods, hypothesizing that the oxide layer formed on the Al surface would provide

stability [27].   These attempts proved successful at stopping surface diffusion and subsequent Raman signal decay over the course of multiple months. However, as seen in Figure 12, the Raman signal from these coatings is significantly weaker than a purely Ag structure [25] [26].
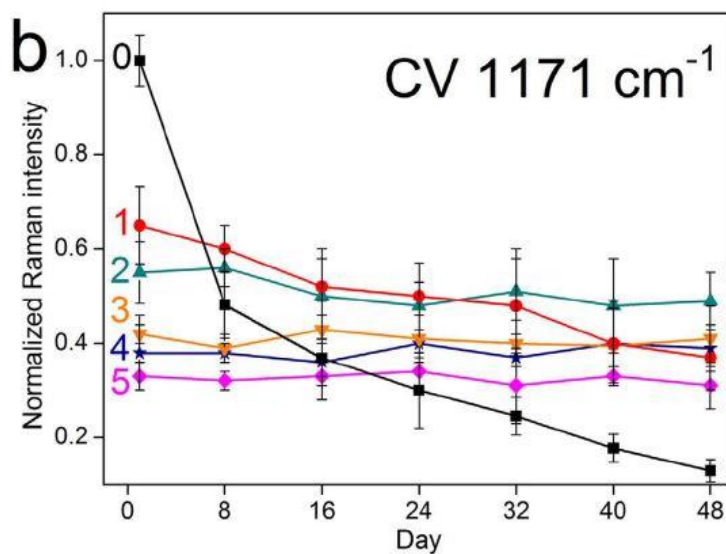
Figure 12: Normalized Raman intensity for the 1171 cm^{-1} peak for Crystal Violet dye molecule (CV). Measured over 48 days using Ag nanorods (0) and TiO2 coated Ag nanorods (1-5) [26].

CHAPTER 5: SUBSTRATE FABRICATION AND CHARACTERIZATION

With so many nano particle fabrication techniques, it becomes important to consider what techniques are available in the lab. At the time of this research, the only technique readily available to this study was thermal evaporation using a technique called oblique angle deposition, also called Glancing Angle Deposition (GLAD).

GLAD

Glancing Angle deposition is a technique to grow nanostructures that utilizes a geometric shadowing effect to grow a large array of discrete structures [28]. GLAD occurs when a collimated vapor flux nucleates and grows columns on a substrate [28]. If the incident angle between the vapor source and the substrate is oblique, then the growing columns will form 'shadows' on the substrate and prevent the formation of a complete film [28]. As the vapor continues to be deposited onto the substrate, the columns continue to grow. The nucleation on the substrate is random, as is the growth of the columns [28]. Some columns grow significantly larger than others and some columns are shadowed during the growth can become 'extinct' [28]. A depiction of the GLAD growth process is seen in Figure 13.
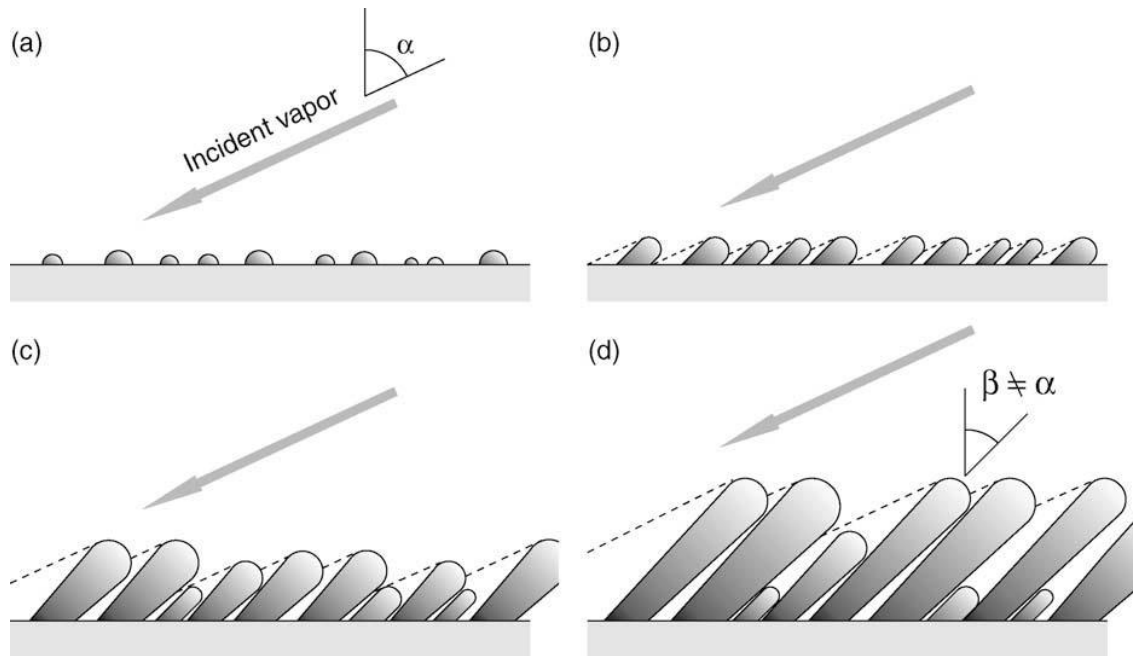
Figure 13: Glancing Angle Deposition. a) Incident vapor nucleates on substrate. b) Colomns start forming and shadowing. c) Columns grow larger, shadow smaller columns. d) Larger columns cause smaller columns to go 'extinct' [28]

Vapor Deposition

The vapor flux used in the GLAD process is a metallic vapor. In our lab, the vapor is created by thermal evaporation under a vacuum. Another technique used is arc plasma deposition, or sputtering [29, 27, 30]. Both thermal evaporation and sputtering are techniques of Physical Vapor Deposition (PVD). PVD techniques employ a physical mean of creating a vapor from source material, and is not limited to metallic materials [29, 27, 30]. Some important variables in vapor deposition are distance between source and substrate, the vacuum pressure, and the deposition rate [67].

An important concept in the deposition of materials is the mean free path of the vapor [29, 27, 30]. This is essentially the statistical distance a particle/molecule can travel before interacting with another particle/molecule [29, 27, 30]. This is governed by the

number of particles in a volume, which is essentially the pressure within the volume. Therefore, the stronger the vacuum (lower pressure), the further a molecule/particle can travel [29, 27, 30]. It becomes important to place substrates within the mean free path of the vapor to have shadowing and deposition [29, 27, 30]. In addition to the distance the vapor can travel, the pressure can also affect contaminations in the substrate [29, 27, 30]. In most cases the chamber will start at atmospheric pressure and filled with air which has a significant amount of contaminates and Oxygen and Nitrogen molecules [29, 27, 30]. If the pressure is too high, there is a possibility of contaminating the structures or the formation of oxides or nitrides [29, 27, 30]. Another important variable is the deposition rate. The formation of discrete, complete structures is reliant on the deposition rate [29, 27, 30, 31]. When the vapor lands on the surface, the atoms still have enough thermal energy to allow for surface diffusion [29, 27, 30, 31]. The atoms can land on the surface then move around until they settle or are locked into place by the next layer of deposition [29, 27, 30, 31]. Therefore, it is important to have deposition rates fast enough to prevent the possibility of the diffusing atoms from forming a film instead of nanorods [29, 27, 30, 31]. However, if the deposition rate is too fast, then it becomes possible for a significant amount of vacancies to form in the structure [29, 27, 30, 31]. Multiple vacancies in a layer can be detrimental to a structure that is only dozens of atoms in diameter [29, 27, 30, 31]. A recommend rate deposition rate for Ag is 1-5Angstroms per second (A/s) and 150 A/s for Al [31]. The reason for such a high rate for Al is to prevent possible reactions between the metallic vapor and residual gas molecules in the chamber [31].

In the case of sputtering, Argon (Ar), or another inert gas, is flowed into the vacuum chamber, ionized by a magnetron sputtering system, and drawn towards the sputtering target by a difference in electrical charge [29, 27, 30]. The material being deposited, called the target, sits at the end of the magnetron and is bombarded by the accelerated ionized gas molecules. Atoms from the source target are then ejected due to the collision of the ionized gas and deposited onto a substrate [29, 27, 30]. Thermal evaporation is a similar concept, but does not involve the use of a gas, but the heating of the source material [29, 27, 30].

Most metals exhibit a phenomenon of having a lower evaporation temperature when under vacuum [29, 27, 30]. Per the Kurt J. Lesker, our main supplier, the evaporation temperatures for Al and Ag are listed out in Table 1 [32]

Table 1: Evaporation Temperatures of Al and Ag [32]

Pressure (Torr)	Temperature (°C)	
	Aluminum	Silver
10^{-4}	1010	1105
10^{-6}	821	958
10^{-8}	677	847

The research presented in this thesis used source pellets of Al or Ag. Materials were deposited by thermal evaporation under vacuum of ~10^{-5} torr using resistance heating of the material sitting in a Tungsten thermal evaporation boat or Boron Nitride crucible purchased through Kurt J. Lesker. Al source material was ¼" by ¼" pellets of 99.999%

Al from Kurt J. Lesker. Ag pellets used were 1/8" by 1/8" 99.999% purity from Kurt J. Lesker. The deposition rate and size of particles was measuring during deposition with a quartz crystal micro balance that was placed near the substrates during the deposition process. Deposition rate was maintained at either 5 or 10 A/s. The deposition system used could not supply the electrical power to deposit Al at 150 A/s, so a rate of 5 A/s was used. The nanorods were set at a glancing angle of about 87 degrees relative to the source material. Substrates used were 1" by 1" quartz (fused silica) slides. The vacuum chamber is made from stainless steel and has water cooling lines along the walls. There is the front access port door and the chamber top is removable with a pneumatic lift, which allows for easier substrate placement in the chamber. A picture of the deposition chamber can be seen as Figure 14. All ports use copper gaskets, except for the front door and lid, which use a rubber gasket. The vacuum chamber is pumped to 10^{-2} torr using a mechanical scroll pump and the pressure inside is measured with a Pirani gauge. Then a turbomolecular pump is used to reach a stronger vacuum level. After about 30mins the chamber pressure reaches between 10^{-6} and 10^{-8} torr, a hot filament ion gauge measures this pressure.

Figure 14: Deposition Chamber (left) and controls (right)

UV-Vis

UV-Vis spectroscopy for all samples was performed at UNF. Measuring the absorbance of substrates from 200 to 700 nm. Substrates were placed with the nanostructure facing the incident light.

Raman Spectroscopy

The first experiments had their Raman spectroscopy performed at the Nanoscale Research Facility at the University of Florida using a 325nm UV laser, 633nm HeNe laser, and solid-state laser with a wavelength of 532nm. Later experiments were performed at the University of North Florida with a solid-state laser with wavelength of 532nm.

The Raman characterization was performed by taking the Raman spectrum of the substrate after letting it sit in a bath of 10^{-6}M R6G solution purchased from Sigma Aldrich. The substrates sat in the R6G for 30minutes, were removed, and then allowed to dry. After drying, the substrates were placed in the Raman spectrophotometer and their Raman spectra were gathered from 240 wavenumber to 2240 wavenumber, with a total number of 1024 measurements taken for each of the spectra. Five spectra were taken at various locations on each substrate in order to get an average spectrum over the entire surface. The Raman spectra are outputted as a text files containing each wavenumber that data were gathered for, and the number of counts for that spectrum gathered. Each individual spectra acquired was a separate file; the individual files were manually condensed into a single excel workbook with each sample having its own sheet in the workbook.

To compare the spectrum from different substrates the five measurements for each sample were normalized from a scale of 0 to 1 using the formula:

$$= \frac{\left(B1 - MIN(B:B)\right)}{\left(MAX(B:B) - MIN(B:B)\right)}$$

This formula was used on all 1024 data points for each spectrum gathered. This normalization was used as an attempt to filter out the unaccountable variables during the experiments that would affect the raw measurement and provide skewed results. The

normalization removes the raw counts from the equation and brings every measurement to a comparable range, with most of the background noise close to a value of zero and the strongest peak reaching a value of one. An average of the five normalized spectra were taken, as was an average of the five raw counts spectra. Then three of the strongest Raman peaks were chosen to be compared across samples. These peaks were at wavenumbers 765, 1352, and 1640.

A few different methods were used to compare the substrates, the number of counts registered at the peaks, the normalized intensity, and the normalized 'enhancement'. The number of counts is just the raw number outputted during the Raman spectroscopy at the specific wavenumber for the substrate. Normalized intensity is the value from 0 to 1 the peak at the specific wavenumber is assigned. And the 'enhancement' is a percent difference between the peak and the average of the background noise around the peak.

SEM Imaging

Images were taken at UF's NRF using the FEI Nova Nano, with the exception of a few of the later images which were taken in MSERF at UNF on the Tescan Mira.

Images were attempted to be acquired using secondary electron imaging at 25k, 60k, and 120k magnification as reported by the SEM software, using accelerating voltages between 5-10kV, and short working distances.

CHAPTER 6: DEGRADATION RESISTANT SUBSTRATES

As mentioned previously, the first goal of this research was to develop a SERS substrate that could be ultimately be used on space missions. This involves using the substrate after they are stored low vacuum for extended periods, of time and subjecting them to extreme temperatures and high vacuum environments.

The design for a new substrate was based on having features to decrease surface mobility of a metallic nanostructure. The substrate should be stable, inert to its environment, and be SERS active to provide a strong signal from trace amounts of molecules. It was hypothesized that an Al or Titanium (Ti) oxide structure would meet these requirements.

Aluminum Nanorod Substrates

The first step to achieving this goal was the use of Al nanorods and their relative stability to surface diffusion. Some research has been performed into using Al as a SERS substrate. It was hypothesized that because of Al's rapid oxidation that the oxide layer formed on the surface of Al nanorods would prevent surface degradation of the substrates [8, 9, 11, 40, 44, 53, 57, 64, 68]. The first substrates used for the research presented in this thesis was an Al nanorod substrate. In order to test the viability of Al nanorods for SERS, various lengths of Al nanorods were grown through GLAD thermal evaporation PVD. Lengths of 25, 50, 100, and 250 nm were produced and characterized with SEM, UV-Vis, and Raman spectroscopy. SEM micrographs, such as the one in Figure 15, of the Al nanorods show domination of sharp peaks and close packed structures. This structure

should theoretically provide strong Raman enhancement for molecules adsorbed onto the surfaces. Uv-Vis characterization show a surface plasmon resonance in the UV spectrum, therefore, Raman experiments were used using a UV laser of 325nm wavelength. However, the Raman experimentation proved that although the oxide layer could provide structural stability it also severely dampens the Raman enhancement and exhibits strong fluorescence. One hypothesis for the dampened enhancement is the loss of free surface electrons when the surface forms the oxide layer.
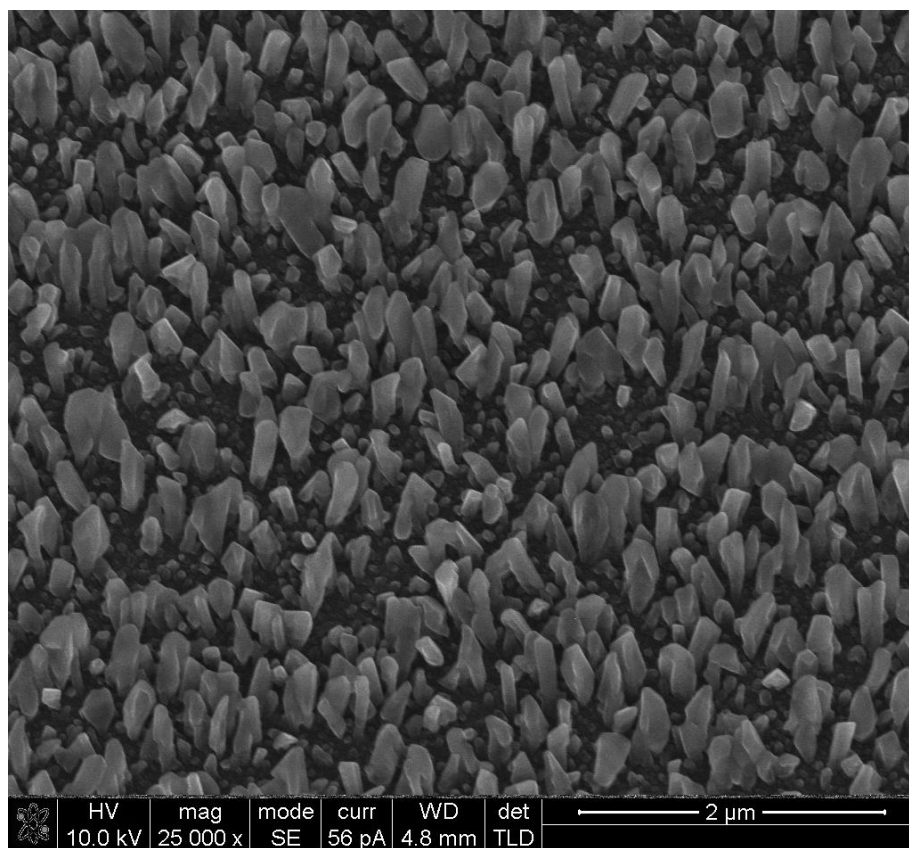
Figure 15: SEM image of 250nm Al Nanorod substrate

Further, it is hypothesized that s substrates with high surface roughness and surface area will raise the energy barrier necessary to initiate the surface mobility and will therefore prevent coalescence into bulk. Finally, it is hypothesized that annealing the structures at a

high temperature will force the particles into a low energy configuration and will become immobilized on the surface when returned to normal storage conditions.

Artificially Accelerating Surface Diffusion

These substrate's ability to withstand surface diffusion and coalescence was tested to determine if the Al nanorods could provide some benefit to future substrates by providing the stable surface and increase roughness required to slow the diffusion of an added nanostructure layer. In order to simulate the process of surface diffusion and accelerate it, the fabricated substrates were heated in air on a hotplate at 500°C for 24 hours. This was to increase the rate of surface diffusion to determine if the substrates would coalesce into a bulk film or remain as discrete particles required for SERS activity. This process would indicate if the substrates would still be viable for SERS measurements after storage for long periods of time. Heating the Al nanorods lead to the formation of a rough island film as seen in Figure 16.

| HV | mag | mode | curr | WD | det | 1 μm |
| 10.0 kV | 60 000 x | SE | 56 pA | 4.8 mm | ETD | |
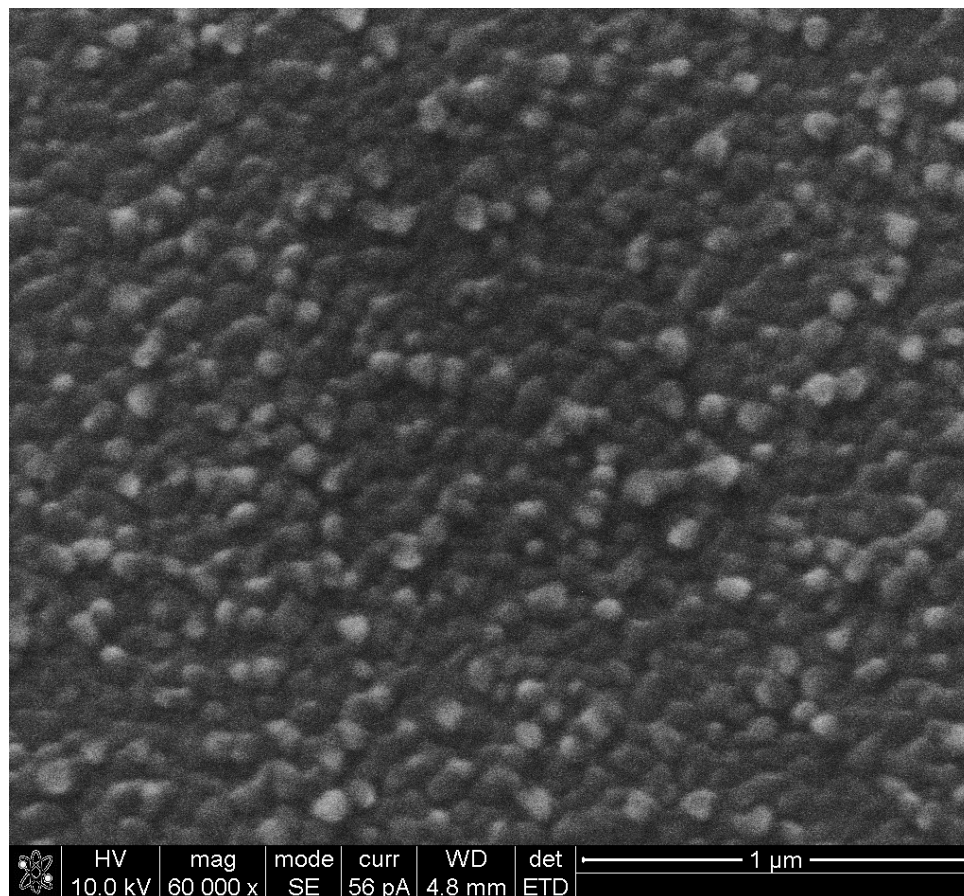
Figure 16: SEM image of 100nm Al Seed post annealing at 500°C for 24 hours

After heating the Al nanorods, the substrate visibly turned transparent. The Uv-Vis spectra in Figure 17 corroborated the transition with their absorbance. The original Al nanorods showed very little variation in absorbance over the entire spectrum except around 250nm where there was a slight bump indicating the presence of a localized surface plasmon resonance in the deep up wavelengths. After heating, the substrates lost almost all of their absorbance over the visible spectrum, with a slight bump in absorbance in the UV wavelengths. This optical transparency, along with no crystalline peaks present in x-ray diffraction, suggest that an amorphous Al oxide or mullite structure may have formed.

Mullite could have resulted from through a reaction between the Al and the fused silica substrate.
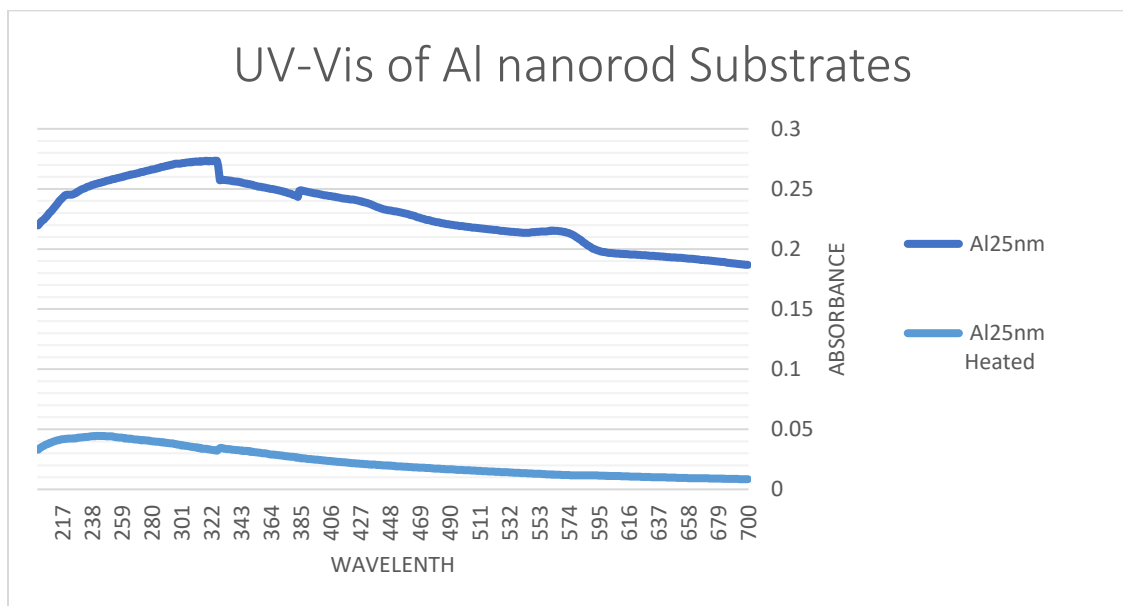
Figure 17: Uv-Vis of Al nanorod substrates

The Raman spectroscopy for the Al after heating was purely background noise with a large broad peak in the low-wave numbers for R6G with every measurement taken. Originally, a UV laser with wavelength of 325nm was used to attempt to induce a surface plasmon resonance and get some enhancement to the signal, but the difference in resonant and incident wavelengths was too great. Additionally a red HeNe laser of 633 and green Solid State diode laser of 532 nm were used; both of these returned no discernable signal apart from the background noise.

Aluminum-Silver Composite Substrates

With the failure of only Al substrates to perform as decent SERS substrates, came the idea of utilizing the stability of Al nanorods and the enhancement of Ag. Ideally, this would fulfil the requirements set by the initial hypothesis regarding substrate characteristics. The idea was to coat the heated Al substrates, given the name of Al 'seeds', with Ag; much like how it is common practice to coat SEM samples with a highly conductive metal in improve the samples conduction path to prevent charging during imaging. Ideally, this coating process would lead to discreet nanoparticles that are resistant to coalescing into a bulk due to the increased surface area and roughness of the Al while still providing a large enhancement for Raman spectroscopy from the Ag.

The 50nm heated Al nanorods, referred to as Al 'seeds', were chosen as a base for the new substrates due to their ability to be rapidly fabricated and their adequate surface roughness. Substrates comprising of lengths of 10, 25, 50, 100, and 200 nm of Ag nanorods, grown on top of the 50nm Al seeds, were fabricated through GLAD thermal evaporation. The different lengths were used to gain an understanding of how the Al seeds affect the resonance, optical properties, surface mobility, and SERS activity of the Ag nanorods on top.

The fabrication process for making these Al-Ag composite substrates starts with a clean fused silica wafer, cleaned with acetone, rinsed with isopropyl alcohol, and with a sonication bath in deionized water. Next, Al nanorods are grown at a glancing angle onto the wafer. This is done at an approximate angle of 87 degrees, at a rate of 5Angstroms per second, and for the desired thickness. Next, the Al nanorods are heated and turned into the

Al seeds by annealing in air at 500°C for 24 hours. The next step is to grown Ag nanorods onto the Al seeds using GLAD thermal evaporation. Finally, to improve stability by heating the Ag nanorod/A seeds to 500°C for a shorter time. In order to compare the stability of the resulting morphology and SERS signals, some of the samples produced are not heated for the final step. The substrate after each step to the fabrication process is pictured in Figure 18.

Figure 18: Optical picture showing the substrates after each fabrication step in the production of Al-Ag composite. From left to right: Clean quartz slide, Al nanorods, Al nano seeds (nanorods annealed in air to 500°C), Ag nanorods grown on top of Al seeds, Ag nanorod/Al nanoseeds annealed in air to 500°C.

One observation to note is the distinct color changes. The Al nanorods appear visually as a gray color, but become completely transparent to the eye when heated at 500°C for 24hours in air. The Ag nanorods appear as a yellow color on top of the Al seeds. This yellow color is from the nanorods localized surface plasmon resonance absorbing light in the blue wavelengths, this can be deduced by comparing the absorbance peak in figure 19 to the wavelength/color chart in figure 20. As the Ag nanorods are heated and begin to change shape, the color of the substrate shifts from a yellow to orange to red to purple depending on the final size of the particles. Figure 19 shows UV-Vis data to show absorbance change after heating substrates.
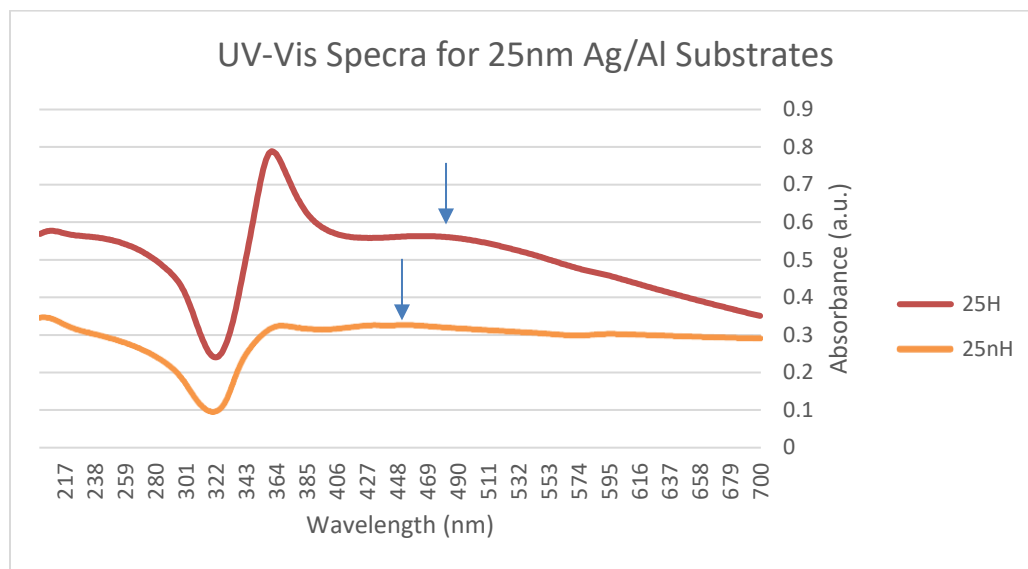
Figure 19: UV-Vis spectra for 25nm Ag nanorods on 50nm Al nanoseeds, Heated and Non heated. Slight absorbance peak around 450nm (absorbs blue, appears yellow) before heating shifts to a slight peak around 480nm (absorbs bluish-green, appears orange) after heating substrate to 500°C for 15 minutes. Also seen is the appearance of a strong absorption peak around 360nm after heating

These changes in color are an indication to the nanoparticles on the substrate are changing size/shape. As outlined previously, as a particles size changes, the wavelengths of plasmon resonance shifts. As the Ag particles grow larger from surface diffusion their absorbance red-shifts and their apparent color shifts accordingly. Figure 20 shows the apparent color for absorbed wavelengths

Figure 20: Diagram depicting absorbed colors and their complementary apparent color
[33]

Electron microscopy imaging of the Ag coated Al seed substrates before and after being heated show what has happened. The Ag nanorods as fabricated on top of Al seeds, not heated, show as a relatively normal nanorods grown by thermal evaporation except that they appear to be closer to a rough film than long nanorods. Normally, when heating Ag nanorods, they turn into a bulk film [73]. When grown on top of the Al seeds they form discrete pools of Ag. It has been hypothesized that the Ag attempts to minimize free surface energy by attempting to coalesce into bulk where particles connect to each other, but the surface roughness provided by the Al seeds prevents the Ag from having adequate mobility. Much like water droplets on a hydrophobic surface, pools of Ag form to reduce surface energy. Particles that are able to touch their neighbors after thermal reshaping are able to coalesce into larger particles through the Oswald ripening mechanism. This gives rise to a characteristic spacing and size of Ag particles for a given deposited Ag thickness. Figure 21 compares the structure before and after heating the Ag nanorods.
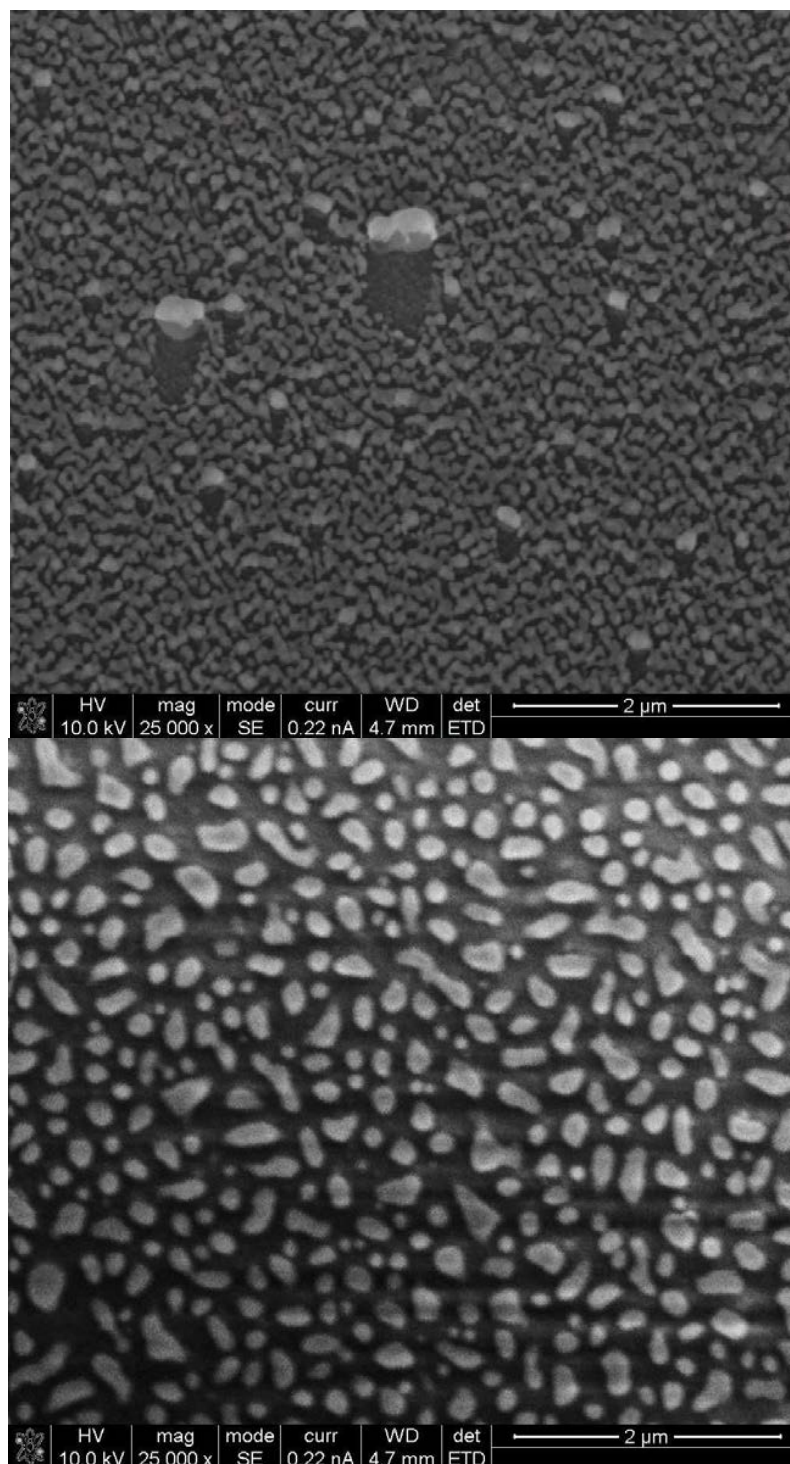
Figure 21: 50nm Ag on 50nm Al seeds as fabricated (top)
and heated to 500°C for 15mins (bottom)

Image processing was done to the SEM micrographs of the substrates to find a correlation between the nanorod thickness and the size/distribution of the Ag particles after heating. Software called Image J [74] was used to adjust the brightness and contrast of each image and to outline the particles. After the particles were distinguished, a statistical analysis on the images was performed and data were collected on the particle sizes and distance between particles. The program was able to outline the particles, count the number of particles, their average size was average distance between particles with standard deviations and standard errors were calculated for each image. Figure 22 shows an example of the program in use on a SEM micrograph. The particles are outlined and the spatial position of the pixels is returned. From the pixel threshold data, averages are numerically calculated. Figure 23 shows the relationship between the deposited nanorod size and the average particle diameter and average distance between particles that results after the annealing process. Additional statistical data for the particle size and distances can be found in Appendix E.

Some of the images of the heated substrates were unable to be analyzed. This is because of substrate charging and image drift, during imaging, preventing the images from having a uniform contrast. The lack of uniform contrast meant the image processing lost a significant number of particles or could not properly identify particle boundaries. Additionally, only heated substrates could be analyzed due to the nanorod images not having discrete boundaries between particles.
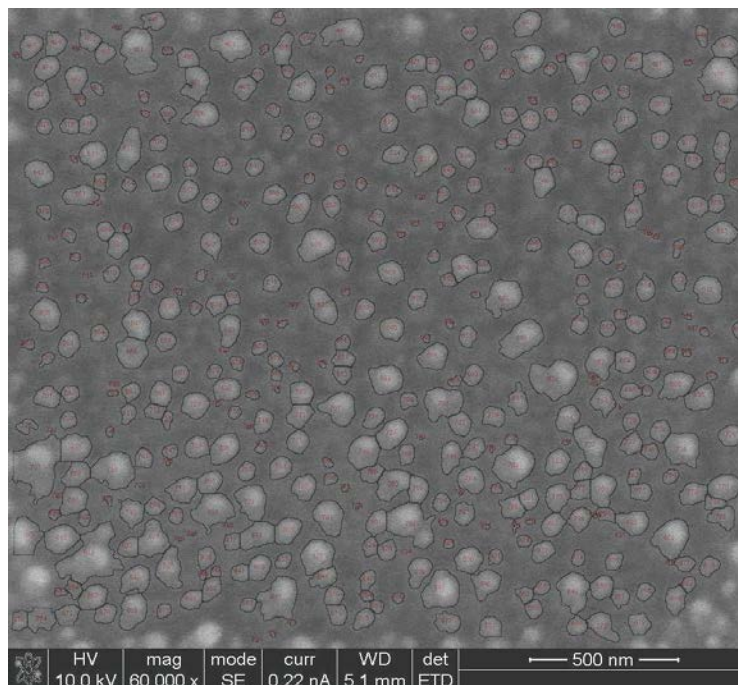
Figure 22: Particle analysis of 10nm Ag/50nm substrate. Particle outlines and number have been overlaid on the original image
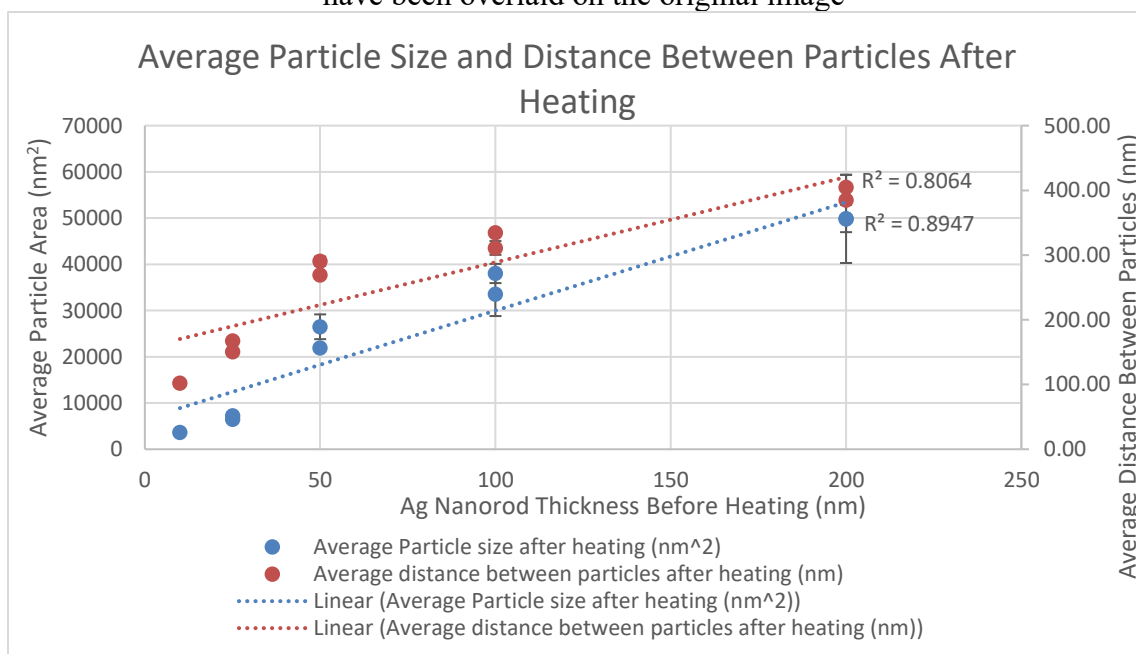
Figure 23: Average particle size and distance between particles after heating. A Near linear relationship between nanorod lengths before heating and the average particle size and average distance between particles after heating

The testing of the Al-Ag composite substrates involved depositing 50nm long Al nanorods and heating them at 500°C for 24 hours. Then various lengths of Ag nanorods were deposited. Lengths of 10, 25, 50, 100, and 200 nm were used. The Ag was then either left as fabricated or heated to 500°C for 15 minutes. This time was chosen to allow adequate surface diffusion and it was observed that diffusion occurs within seconds as noted by a visible color change in the samples. An entire set of substrates for this experiment contained 10 different samples, a heated and non-heated version of each of the 5 lengths of Ag nanorods.

Comparing the normalized Raman spectra of the heated composite substrates to the non-heated composite substrates shows little difference between them, indicating that the accelerated surface diffusion from heating the substrates still allows for enhancement as the nanostructures remain.
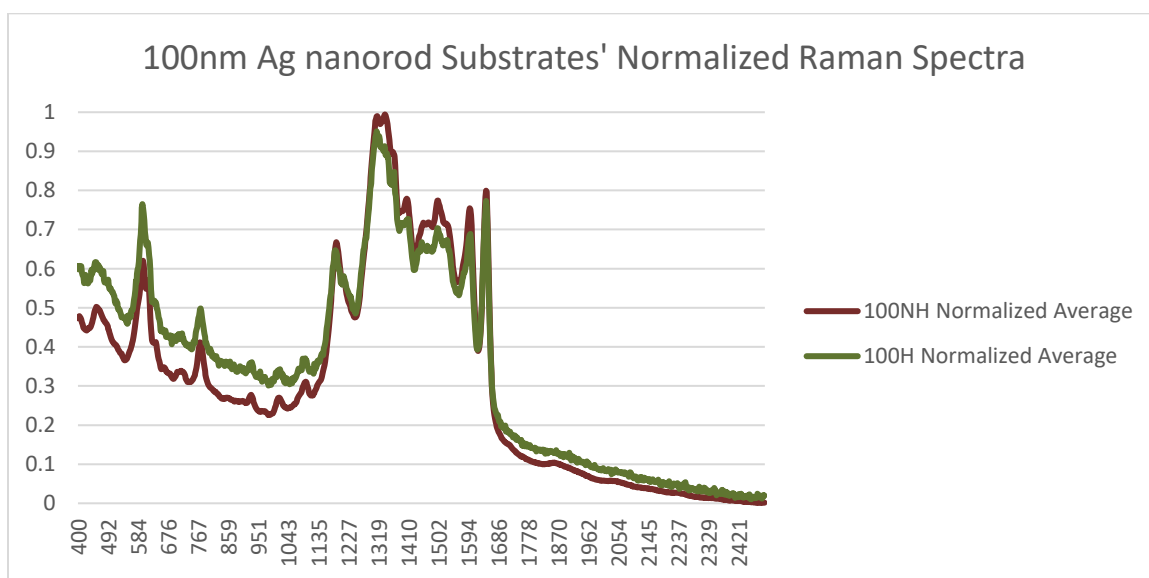
Figure 24: Raman spectra for 100nm heated and non-heated Ag nanorod/Al nanoseed substrates

Vacuum Storage

Since there are multiple possible sources from the decay in the Raman signal over the course of the substrates life time, it became necessary to attempt to separate the possible causes. The difference in signal seen was most likely from the change in surface structure, but could also be from a chemical degradation from sulfur and oxygen compounds bonding/adsorbing onto the surface. The hypothesis for this experiment was that vacuum storage may result in surface diffusion due to the lack of pressure on the surface, but prevent a chemical change to the surface.

It is widely reported in the literature that Ag quickly oxidizes in air and also reacts with Sulfur (S) from the atmosphere, both of these events would lead to a decrease in SERS effectiveness [62]. In an attempt to separate the effects due to sulfur and oxygen adsorption an experiment to store the Raman substrates under vacuum was designed. A load lock vacuum was designed in-house to accomplish this. The chamber is comprised of copper tubing, compression fittings, ball valves, needle valves, and Ball jars. Utilizing this storage system, samples were created and stored under vacuum every week for a month without the need of breaking vacuum to add additional samples to the vacuum storage. Overall, samples should be exposed to air for less than 5 minutes between fabrication and characterization. The system can be seen in Figure 25 and Figure 26, with Figure 26 showing the storage chamber sections. The components used in the vacuum storage system were mainly chosen based on their inexpensiveness and availability. The system is pumped to vacuum by a BMH 70 Dry TurboSystem, which is a turbo-molecular pump backed with a mechanical diaphragm pump. Vacuum level is measured with an Edwards WRG-s wide

range gauge and digital controller. Each section of the storage system can be isolated from the rest by closing the ball valve at the individual chamber or the needle valves along the main spine of the setup. The initial section is pumped down via the mechanical/turbo system with the rest of the chambers isolated. To add additional sections to the vacuum, the previously pumped sections are closed off at their respective ball valves, the turbo pump is stopped, the new section's needle valve is opened to the mechanical pump and allowed to pump down to ~1 torr, and then the turbo pump is turned back on. Once the new section is pumped to at least 10^{-3} torr the previously pumped sections are opened to the vacuum again. Before a section is added to the vacuum, it is filled with Argon gas to displace any oxygen in the jar in an attempt to minimize contaminating the vacuum system.
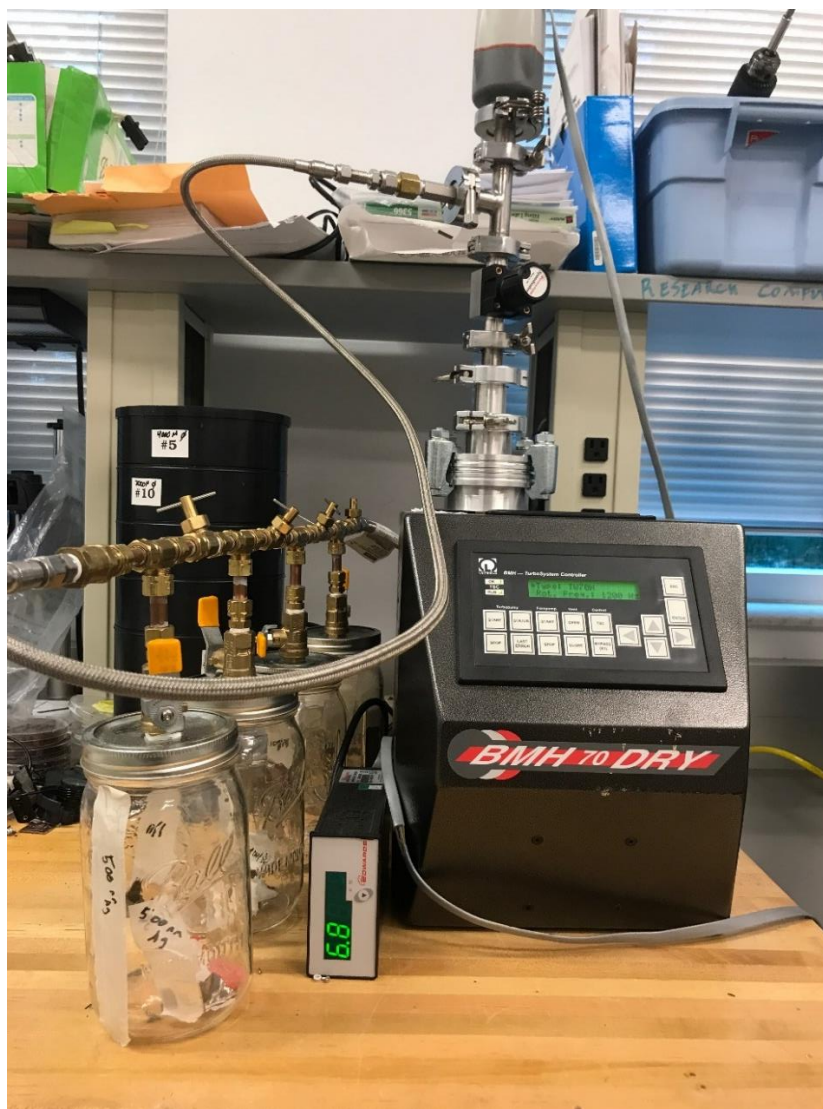
Figure 25: Load Lock Vacuum Storage Setup

Figure 26: Load Lock Vacuum Storage Containers

The 100nm Ag nanorods thickness of the Al-Ag composite substrates were chosen to be observed during the month long vacuum storage experiment due to their initially strong SERS enhancement. This length seemed the most appropriate considering the promising results and relative ease of imaging during the previous experiment.

Over the course of a month, multiple heated and non-heated versions of 100nm Ag and 50nm Al composite substrates were fabricated every week, half of the produced substrates were stored in sterile, plastic petri dishes in air while the rest were placed under vacuum storage. At the end of the month long experiment the samples stored under vacuum were compared to those stored in air.

The hypothesis going into this experiment was that the Raman enhancement would decay significantly less when the samples were stored under vacuum than those stored in air due to the oxygen and sulfur species not being able to adsorb onto the Ag surface when under vacuum. However, when testing the samples with Raman spectroscopy, those stored under air provided stronger signals than those from the vacuum as seen in Figure 27. The Raman results also indicated that each set of samples that were produced each week had large sample variation due to experimental conditions and therefore not directly comparable. The variability is due to the randomness of the experimental conditions such as overall surface geometry, exact deposition conditions, non-uniform drying rate of analyte solution, and non-uniform analyte coating the surface after drying. However, the set of substrates created for a week were fabricated in the same deposition. Therefore, the samples created in a week are directly comparable.
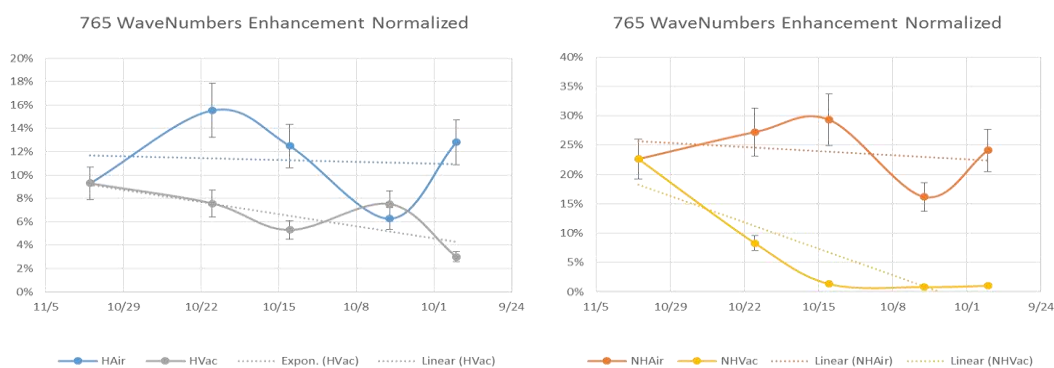
Figure 27: Normalized enhancement compared to background noise at 765 Wavenumbers for each sample over month long experiment

After the unexpected results, the working hypothesis changed to the vacuum storage accelerated surface diffusion and reshaping due to the lack of pressure at the surface. This implicates that the morphological change is strongly influences the strength of the Raman signal. At the end of the month, usable SEM micrographs of the substrates could not be taken due to issues with substrate charging and time constraints with the imaging session. However, with the opening of the MSERF lab at UNF, images of the substrates were taken nearly after nearly 6 months of storage. These images are not ideal, but still provide a great deal of information on what happens during storage. Comparing the non-heated samples, it shows that the sample stored in air looks similar to the start of the experiment, but the vacuum non-heated underwent the most significant surface diffusion. The heated samples look nearly identical to the starting image. Figure 28 shows a comparison between the start and after 6 months of storage for air stored, vacuum stored, heated, and not heated substrates.

While not the ideal outcome, this experiment still provided ample information. The surface diffusion can be understood as the Ag moving to minimize the overall surface energy. The acceleration of diffusion is hypothesized to be attributed to the lack of pressure on the surface leading to a decrease of energy required to overcome physical barriers. It became evident that the characteristic diameter and separation of the particles seen in the heated case is related to the thickness of Ag and roughness of the seeds they are resting on. Heated samples, already at a lower energy configuration, are unable to overcome diffusion barriers and remain immobile and retain their initial size.
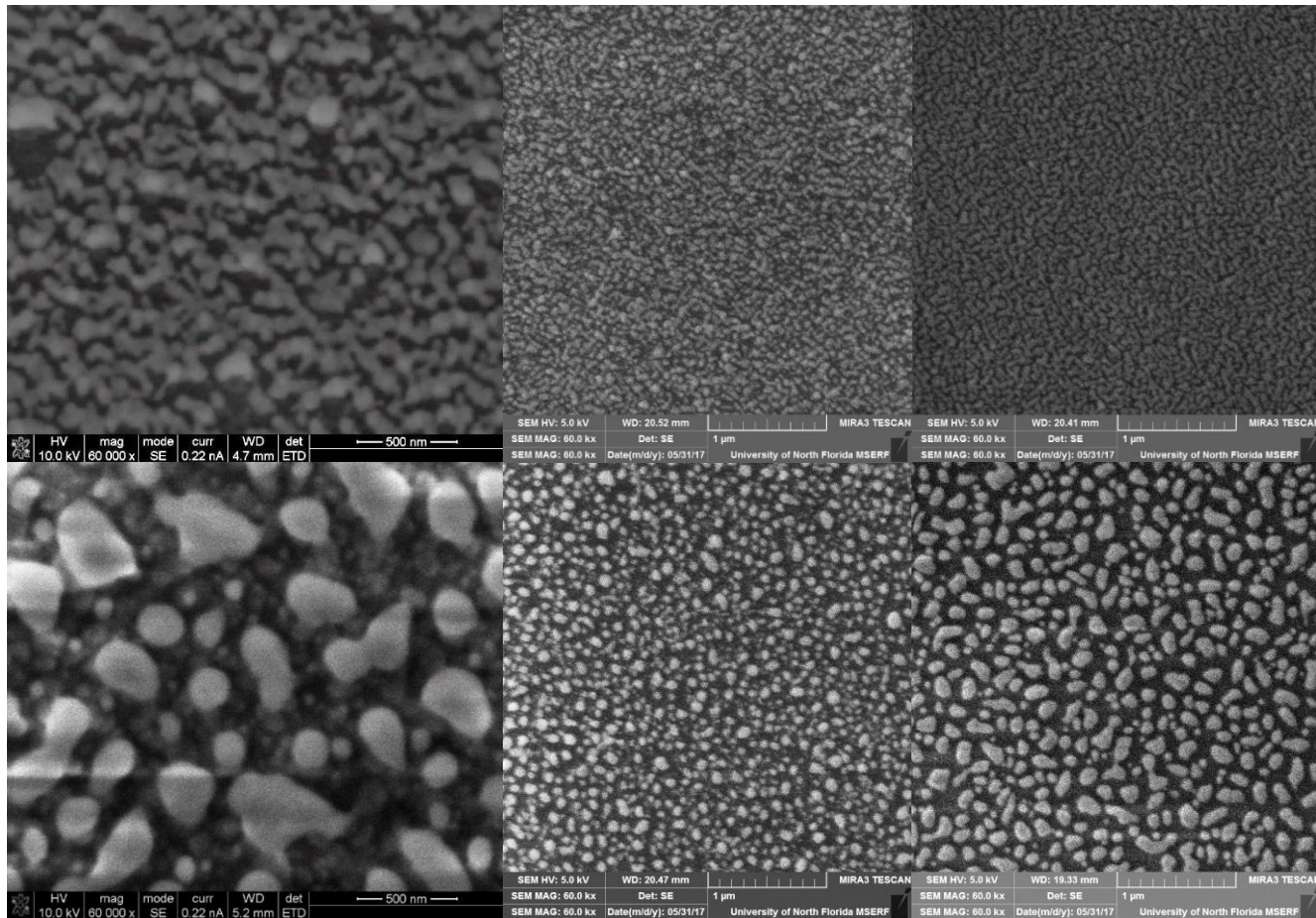
Figure 28: 100nm Ag nanorods grown on 50nm Al nanoseeds
Top left: 100nm not heated at the start. Bottom left: 100nm heated at start.
Top Middle: 100nm Air stored not heated. Bottom Middle: 100nm Air stored heated.
Top Right: 100nm Vacuum stored not heated. Bottom Right: 100nm vacuum stored heated

Stability of Au vs Ag

Having worked in the area of physical degradation resistance, the impact of chemical degradation was studied briefly during the last three months of work. In an effort to separate the chemical and physical mechanisms, SEM microscopy, FTIR spectroscopy, and SERS measurements were taken on arrays of Ag and Au nanorods grown using physical vapor deposition. Here, the hypothesis is that Au rods may have some morphological change over the course of extended storage in air, but should be chemically inert. The lack of the chemical component of degradation would give an insight to the effects of chemical degradation of Ag.

Ag and Au nanorods, shown in Figure 29, were grown to lengths of 500 nm nominal at a deposition rate of 0.5 nm / s onto solvent cleaned Si <100> wafer chips using electron beam physical vapor deposition at Northeastern University. Samples were maintained at a source to substrate distance of 50 cm and at an incidence angle of 87 °. Substrate temperatures were not controlled but remained below 40°C. Immediately after, samples were expedited to UNF, overnight, in a vacuum sealed bag.
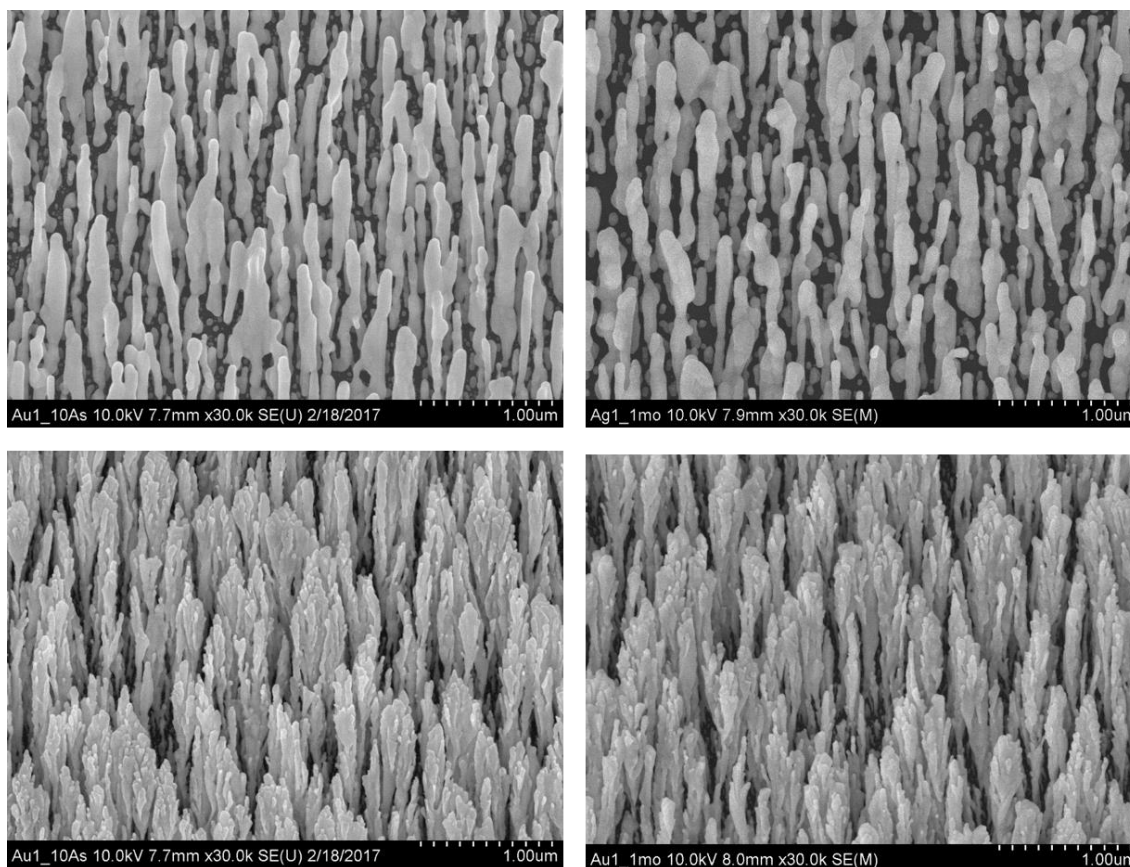
Figure 29: SEM images of fresh Ag nanorods (Top left), Ag nanorods after 28 days in air (Top right), fresh Au nanorods (Bottom left), and Au nanorods after 28 days in air (Bottom right).

SEM images were taken within 12 hours of growth and again 28 days after growth. As shown in the SEM images included in Figure 29, the morphological change is apparently absent in the Ag structure, however, in the Ag structure there is a significant loss of particles even though overall structure and diameter remaining the same for both cases. Some coarsening through diffusion is likely in the Ag, but is not evident in Au. The lack of Au coarsening is evident through the small, sharp details of the structure persisting over the course of the 28 days.

FTIR spectra were taken on day 1 and again on day 28, Figure 30. On day 28, new peaks emerged for Ag and Au that were not visible on day 1. On day 1, no peaks were visible throughout the spectra, as expected for clean metallic surfaces. Hydrocarbon peaks are visible for Ag around wavenumber 2800 and 1600. These peaks are substantially stronger for Ag that for Au, which has only a minute trace of these peaks. The sequestration of some material from the air is expected for any nanostructured material. Interestingly, the greater sequestration of Ag than Au may be due to greater reactivity, or the activation of the surface through a change of termination. The change of termination of the immediate surface may be understood through the peak at 520 wavenumber, seen amplified in the inset. This peak designates the vibrational mode of AgS and shows that there is S binding to the surface. The active AgS compound may then act to attract additional materials out of the air.
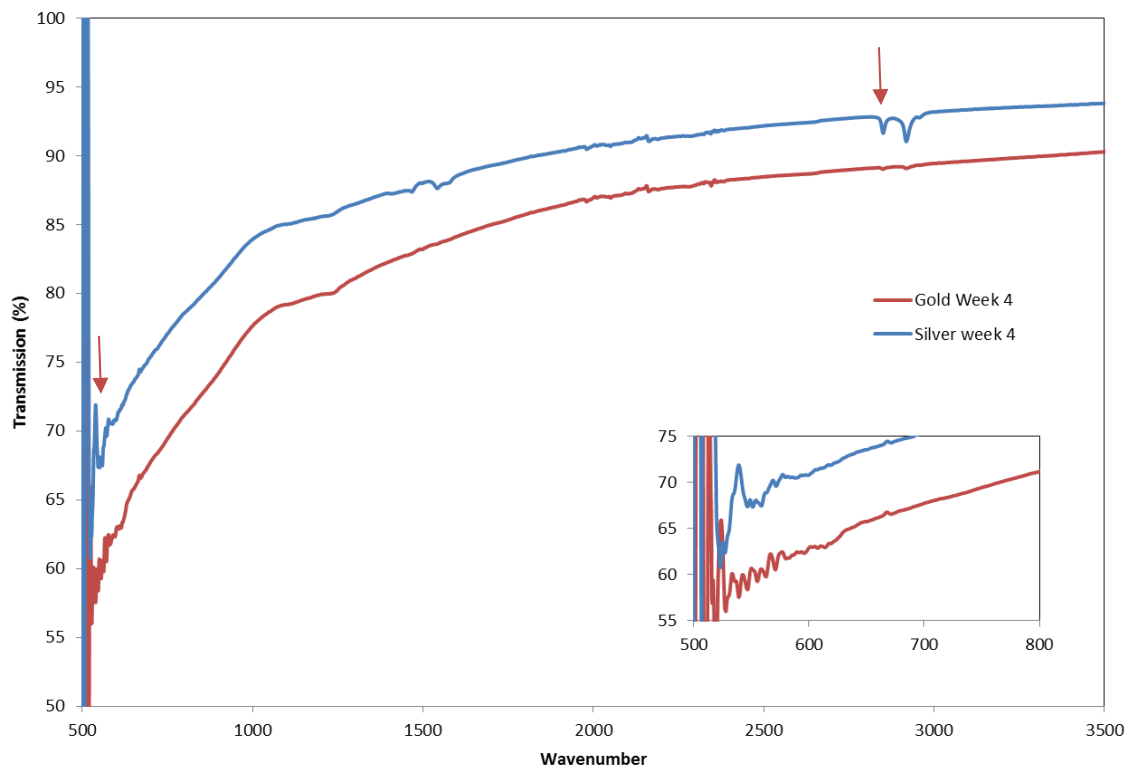
Figure 30: FTIR spectra of Au and Ag nanorods after 28 days storage in air. Peaks for AgS and hydrocarbons can be seen at around 520 and 2800 respectivly. Contamination is more pronounced on the Ag substrate.

When SERS is performed to detect aqueous 1×10^{-6} M R6G on both of the substrates on day 1, the Ag sample outperforms the Au sample by a factor of 20, as shown in Figure 31. Representative R6G peaks are shown for both Ag and Au, while Au demonstrates a flatter signal. This experimental set is of interest for two reasons, first, the use of Au rods from PVD has never before been shown in the literature for SERS. Second, Au is shown to have a strong enhancement, as Ag in this configuration has a tremendous enhancement for R6G. It is possible that the use of a wavelength closer to the resonance wavelength of Au would lead to stronger Raman signals. For comparison, when the same

concentration of R6G is used on a Corning Glass slide, there is no distinguishable Raman signal.
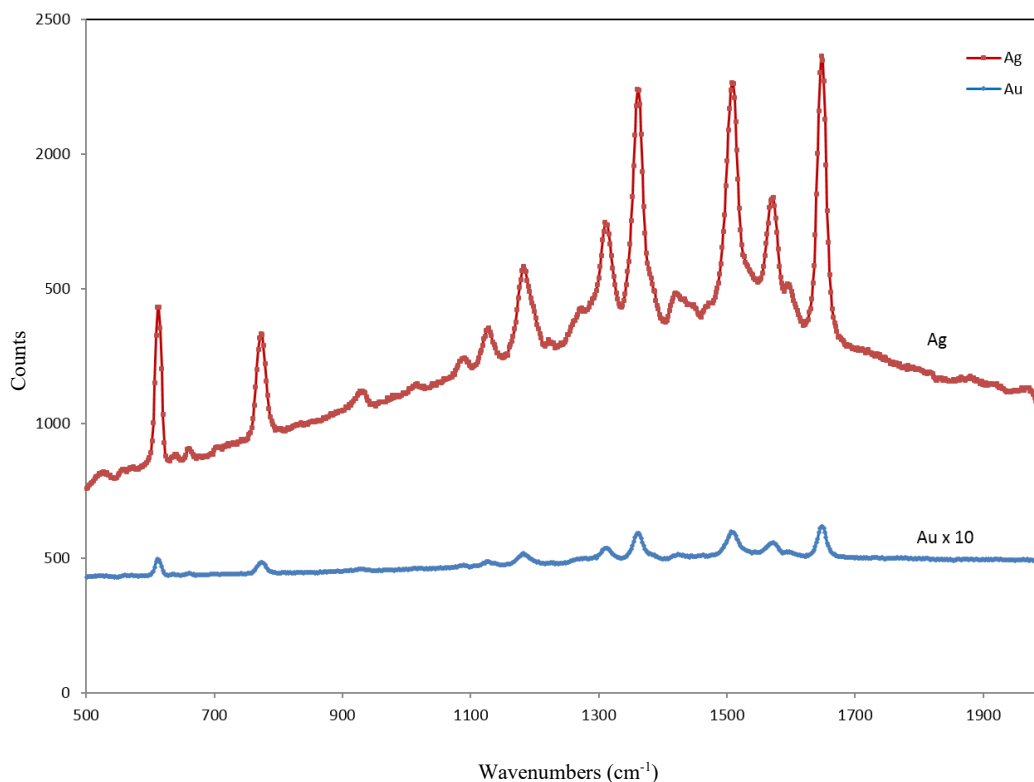
Figure 31: Raman spectra taken on day 1 for Ag and Au substrates. Spectrum for Au has been multiplied by a factor of 10 to compare to the significantly stronger signal of Ag

When this test is repeated weekly on samples from the same substrate with fresh R6G solution, the results show that Au is remarkably stable when compared to Ag, Figure 32. To compare the relative stability of the two samples, signal to noise ratio is taken for wavenumber 1650 and plotted against the day this measurement was taken. While Ag shows a markedly negative trend over 28 days, Au remains nearly perfectly stable. Spread in the signal to noise from day to day can be attributed to the expected spread between spots on an individual substrate.
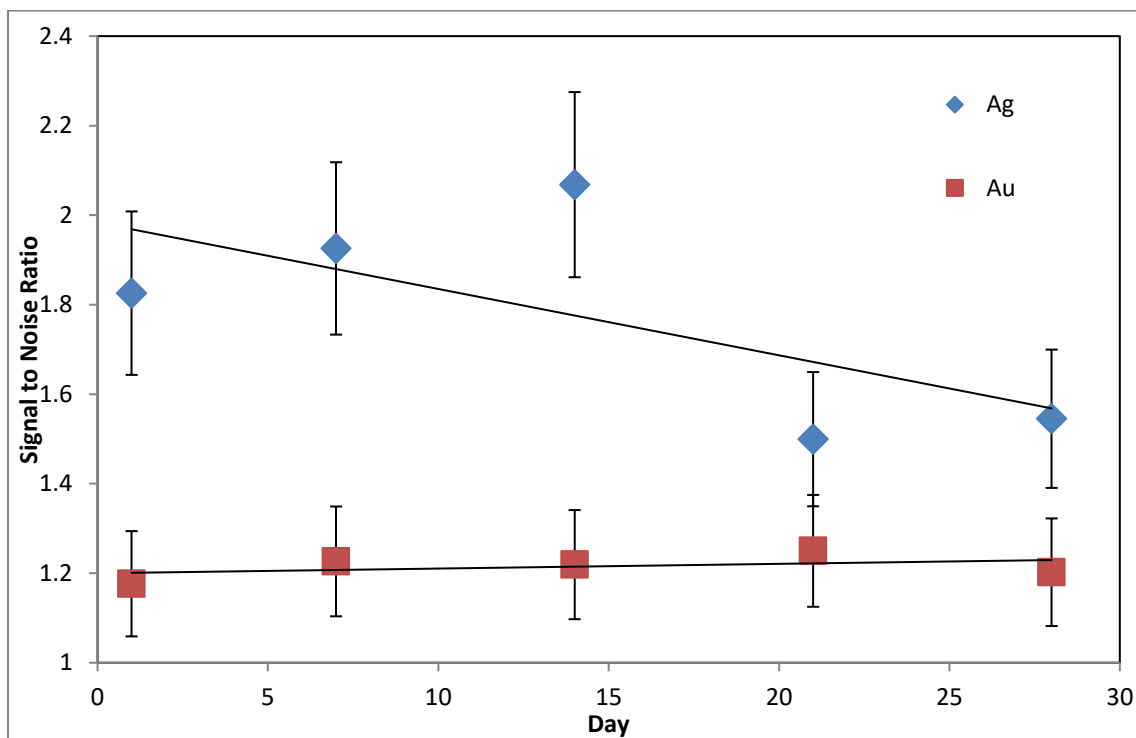
Figure 32: Comparison of signal to noise ratios for Au and Ag nanorods substrates stored in air over 28 day period

Discussing these results, two salient features arise. First, the physical degradation of Ag nanorods in air over the length scale of days could be due to oxidation and sulphurization from the ambient atmosphere causing the morphological changes. This is supported by the fact that Ag has clearly distinguishable AgS and hydrocarbon peaks in the FTIR spectra at 28 days alongside the notable loss of structure. When compared to the lack of change on the Au structure alongside the lack of absorbance peaks in the Au FTIR spectrum, it is evident to the possibility of contaminates accelerating surface diffusion. The second salient feature is the implication of the stability of Au. For shear enhancement factor, Ag nanorods will of course remain king. However, if someone wants to sell a commercial Raman spectroscopy substrate with good shelf life or study the degradation of the analyte over time, Au affords this ability.

Since no morphological change is evident in Au, this experiment will be replicated in the future with heating of the Au and Ag nanorods to drive morphological changes to a more stable configuration as seen in previous experiments. This will allow effects of chemical degradation of Au and Ag to be directly comparable.

CONCLUSION

This work reports on two areas of study: 1) the design of a degradation resistant SERS substrate; 2) A scientific ingestion into the mechanism of Raman signal degradation.

The novel Ag/Al composite SERS substrate showed interesting results. The unusual structure shown after heating and surface diffusion happening is the result of mobile Ag structures, partially immobilized by the rough surface provided by the Al seed underlayer. It was hypothesized that the Al layer provided a sufficiently large energy barrier to prevent the entire coalescence of the Ag particles. Particles that were close enough to each other coalesced into larger particles through Ostwald ripening where they could touch during thermal reshaping.

Vacuum storage of these substrates also provided interesting results, with the Ag structure going through more surface diffusion than the substrates stored at atmospheric pressure. The vacuum stored substrates had significantly more loss to their Raman signal than the substrates stored under air. This suggests that surface diffusion may contribute more to the decay in signal than surface contamination for Ag

When testing Ag nanorods against Ag nanorods over the course of 28 days in air, the Au nanorods exhibit almost no degradation to the Raman signal while Ag nanorods have a significant loss in structure and Raman signal. While neither substrate appears to have experience dramatic surface diffusion, Ag shows about a 20% loss of structure, and the FTIR spectra show the binding of sulfur and adsorption of hydrocarbons to the Ag. This contamination explains the decay in signal for the Ag substrate while the Au substrate

experienced little loss in signal and could possibly be the cause of the loss of structure in Ag.

Additional experiments to consider performing are a comparison between storage at atmosphere, under vacuum, and above atmospheric pressure. An experiment involving the entire fabrication of the substrates without breaking vacuum to study the mobility of the Ag nanoparticles and its effect on coalescence. Additionally, an experiment comparing nanorods surface diffusion across different fabrication methods, i.e. Thermal evaporation vs e-beam. Finally, performing experiments with Au nanorods grown on top of Al nanoseeds to utilize the restrictions on surface mobility the structure provides alongside the chemical stability seen in Au samples.

REFERENCES

[1] H. Watanabe, N. Hayazawa, Y. Inouye and S. Kawata, "DFT Vibrational Calculations of Rhodamine 6G Adsorbed on Silver: Analysis of Tip-Enhanced Raman Spectroscopy," J. Phs. Chem. B, pp. 5012-5020, 2005.

[2] E. C. l. Ru, E. Blackie, M. Meyer and P. G. Etchegoin, "Surface Enhanced Raman Scatering Enhancement Factors: A Compreshensive Study," J. Phys. Chem. C 111.37, pp. 13794-3803, 2007.

[3] K. Kneipp, Y. Wang, H. Kneipp, L. T. Perelman, I. Itzkan, R. R. Dasari and M. S. Feld, "Single Molecule Detection Using Surface-Enhanced Raman Scattering (SERS)," Phys. Rev. Lett. 78.9, pp. 1667-670, 1997.

[4] E. C. Le Ru and P. G. Etchegoin, Principles of Surface-Enhanced Raman Spectroscopy and related plasmonic effects, Amsterdam: Elsevier, 2009.

[5] P. L. Stiles, J. A. Dieringer, N. C. Shah and R. P. Van Duyne, "Surface-Enhanced Raman Spectroscopy," Annu. Rev. Anal. Chem. 1, pp. 601-26, 2008.

[6] M. Moskovits, "Surface-Enhanced Spectroscopy," Rev. Mod. Phys. 57, pp. 783-826, 1985.

[7] B. E. Billinghurst, S. A. Oladepo and G. R. Loppnow, "PH-Dependent UV Resonance Raman Spectra of Cytosine and Uracil," J. Phys. Chem. B 113.20, pp. 7392-397, 2009.

[8] T. Dörfer, M. Schmitt and J. Popp, "Deep-UV Surface-enhanced Raman Scattering," J. Raman Spectrosc. 38.11, pp. 1379-382, 2007.

[9] S. K. Jha, Z. Ahmed, M. Agio, Y. Ekinci and J. F. Löffler, "Deep-UV Surface-Enhanced Resonance Raman Scattering of Adenine on Aluminum Nanoparticle Arrays," J. Am. Chem. Soc. 134.4, pp. 1966-969, 2012.

[10] M. A. Ordal, L. L. Long, R. J. Bell, S. E. Bell, R. R. Bell, R. W. J. Alexander and C. A. Ward, "Optical Properties of the Metals Al, Co, Cu, Au, Fe, Pb, Ni, Pd, Pt, Ag, Ti, and W in the infrared and far infrared," Applied Optics 22-7, pp. 1099-120, 1983.

[11] K. Ray, M. H. Chowdhury and J. R. Lakowicz, "Aluminum Nanostructured Films as Substrates for Enhanced Fluorescence in the Ultraviolet-Blue Spectal Region," Anal. Chem. 79.17, pp. 6480-487, 2007.

[12] A. Taguchi, Y. Saito, K. Watanabe, S. Yijan and S. Kawata, "Tailoring Plasmon Resonaces in the Deep-ultraviolet by Size-tunable Fabrication of Aluminum Nanostructures," Appl. Phys. Lett. 101.8, p. 081110, 2012.

[13] J. D. Gelder, K. D. Gussem, P. Vandenabeele and L. Moens, "Reference database of Raman Spectra of Biological Molecules," J. Raman Spectrosc. 38, pp. 1133-1147, 2007.

[14] K. Kneipp, H. V. Kneipp, B. Kartha, R. Manoharan, G. Deinum, I. Itzkan, R. R. Dasari and M. S. Feld, "Detection and Identification of a Single DNA Base Molecule Using Surface-enhanced Raman Scattering (SERS)," Phys. Rev. E 57.6, p. n. pag., 1998.

[15]   C. Otto, T. J. J. van den Tweel, F. F. M. de Mul and J. Greve, "Surface-Enhanced Raman Spectroscopy of DNA Bases," J. Raman Spec. 17, pp. 289-298, 1986.

[16]   H. Xu, E. J. Bjerneld, M. Käll and L. Börjesson, "Spectroscopy of Single Hemoglobin Molecules by Surface Enhanced Raman Scattering," Phys. Rev. Lett 83.21, pp. 4357-360, 1999.

[17]   S. Link and M. A. El-Sayed, "Spectral Properties and Relaxation Dynamics of Surface Plasmon Electronic Oscillations in Gold and Silver Nanodots and Nanorods," J. Phys. Chem. B 103.40, pp. 8410-426, 1990.

[18]   Y. Maruyama and M. Futamata, "Elastic Scattering and Emission Correlated with Singe-molecule SERS," J. Raman Spectrosc. 36.6-7, pp. 581-92, 2005.

[19]   [Online]. Available: http://www.chem.umd.edu/wp-content/uploads/2014/01/RamanSpectroscopy.jpg.

[20]   P. C. Pinheiro, S. Fateixa, H. I. S. Nogueira and T. Trindade, "SERS Studies of DNA Nucleobases Using New Silver Poly(Methyl Methacrylate) nanocomposites as Analytical Platforms," J. Raman Spectrosc. 46, pp. 47-53, 2015.

[21]   H. Lin, Q. Shao, F. Hu, H. Wang and M. Shao, "A Direct Detection of Amino Acids with Surface-enhanced Rman Scattering: Cu Nanoparticle-coated Copper Vanadate Nanoribbons from Mechanochemistry," Thin Solid Films 558, pp. 385-90, 2014.

[22]   C. E. Amri, M.-H. Baron and M.-C. Maurel, "Adenine and RNA in Mineral Samples," Spectrochimica Acta Part A: Molecular and Biomolecular Spectroscopy, pp. 2645-654, 2003.

[23]   H. Xu, J. Aizpurua, M. Käll and P. Apell, "Electromagnetic Contributions to Single-molecule Sensitivity in Surface-enhanced Raman Scattering," Phys. Rev. E 62.3, pp. 4318-324, 2000.

[24]   J. Jiang, K. Bosnick, M. Maillard and L. Brus, "Single Molecule Raman Spectroscopy at teh Junctions of Large Ag Nanocrystals," J. Phys. Chem. B 107, pp. 9964-9972, 2003.

[25]   A. M. Michaels, J. Jiang and L. Brus, "Ag Nanocrystal Junctions as the Site for Surface-Enahanced Raman Scattering of Single Rhodamine 6G Molecules," J. Phys. Chem. B 104, pp. 11965-11971, 2000.

[26]   K. A. Bosnick, J. Jiang and L. E. Brus, "Fluctuations and Local Symmetry in Single-Molecule Rhodamine 6G Raman Scattering on Silver Nanocrystal Aggregates," J. Phys. Chem. B 106, pp. 8096-8099, 2002.

[27]   X. Xu, K. Kim, C. Liu and D. Fan, "Fabrication and Robotization of Ultrasensitive Plasmonic Nanosensors for Molecule Detection with Raman Scattering," Sensors 15.5, pp. 10422-0451, 2015.

[28]   A. Weiss and G. Haran, "Time-Dependent Single-Molecule Raman Scattering as a Probe of Surface Dynamics," J. Phys. Chem. B 105, pp. 12348-12354, 2001.

[29]   R. A. Halvorson and P. J. Vikesland, "Surface-Enhanced Raman SPectroscopy (SERS) for Environmental Analyses," Environ. Sci. Technol. 44, pp. 7749-7755, 2010.

[30]   X. Qian, X.-H. Peng, D. O. Ansari, Q. Yin-Goen, G. Z. Chen, D. M. Shin, L. Yang, A. N. Young, M. D. Wang and S. Nie, "In Vivo Tumor Targeting and Spectroscopic Detection with Surface-Enhanced Raman Nanoparticle Tags," Nat. Biotechnol. 26, pp. 83-90, 2008.

[31]   J. Gersten and A. Nitzan, "Electromagnetic Theory of Enhanced Raman Scattering by Molecules Adsorbed on Rough Surfaces," J. Chem. Phys 73, pp. 3024-037, 1980.

[32]   E. Hao and G. C. Schatz, "Electromagnetic Fields Around SIlver Nanoparticles and Dimers," J. Chem. Phys. 120, pp. 357-366, 2004.

[33]   K. Kneipp, M. Moskovits, H. Kneipp and (Eds.), Surface-Enhanced Raman Scattering: Physics and Applications, Springer, 2006.

[34]   E. J. Zeman and G. C. Schatz, "An Accurate Electromagnetic Theory Study of Surface Enhancement Factors for Ag, Au, Cu, Li, Na, Al, Ga, In, Zn, and Cd," J. Phys. Chem. 91, pp. 634-643, 1987.

[35]   K. L. Kelly, E. Coronado, L. L. Zhao and G. C. Schatz, "The Optical Properties of Metal Nanoparticles: The Influence of Size, Shape, and DIelectric Environment," J. Phys. Chem. B 107, pp. 668-677, 2003.

[36]   R. P. Kooyman, "Chapter 2: Physics of Surface Plasmon Resonance," in N.A., N.A., pp. 15-34.

[37]   M. E. Abdelsalam, S. Mahajan, P. N. Bartlett, J. J. Baumberg and A. E. Russell, "SERS at Structured Palladium and Platinum Surfaces," J. Am. Chem. Soc, pp. 7399-406, 2007.

[38]   S. B. Chaney, S. Shanmukh, R. A. Dluhy and Y.-P. Zhao, "ALigned Silver Nanorod Arrays Produce High Sensitivity Surface-Enhanced Raman Spectroscopy Substrates," Appl. Phys. Lett. 87, pp. 031908-1-3, 2005.

[39]   Y.-X. Chen and A. Otto, "Electronic Effects in SERS by Liquid Water," J. Raman Spectrosc. 36.6-7, pp. 736-47, 2005.

[40]   Y. Ekinci, H. H. Solak and J. F. Löffler, "Plasmon Resonances of ALuminum Nanoparticles and Nanorods," J. Appl. Phys. 104.8, pp. 083107-1-83107-6, 2008.

[41]   S. Eustis and M. A. El-Sayed, "Why Gold Nanoparticles are More Precious Than Pretty Gold: Noble Metal Surface Plasmon Resonance and its Enhancement of the Radiative and Nonradiative Properties of Nanocrystals of Different Shapes," Chem. Soc. Rev. 35, pp. 209-217, 2006.

[42]   M. Futamata, Y. Maruyama and M. Ishikawa, "Adsorbed Sites of Individual Molecules on Ag Nanoparticles in Single Molecule Sensitivity- Surface-Enhanced Raman Scattering," J. Phys. Chem. B 108, pp. 13119-13127, 2004.

[43]   D. H. Jeong, Y. X. Zhang and M. Moskovits, "Polarized Surface Enhanced Raman Scattering from ALigned Silver Nanowire Rafts," J. Phys. Chem. B 108, pp. 12724-12728, 2004.

[44] M. W. Knight, L. Liu, Y. Wang, L. Brow, S. Mukherjee, N. S. King, H. O. Everitt, P. Norlander and N. J. Halas, "Aluminum Plasmonic Nanoantennas," Nano Lett. 12.11, pp. 6000-04, 2012.

[45] D. L. Stokes and T. Vo-Dinh, "Development of an Integrated Single-Fiber SERS Sensor," Sensors and Actuators B 69, pp. 28-36, 2000.

[46] A. R. Tao and P. Yang, "Polarized Surface- Enhanced Raman Spectroscopy on Coupled Metallic Nanowires," J. Phys. Chem. B Letters 109, pp. 15687-15690, 2005.

[47] R. A. Tripp, R. A. Dluhy and Z. Yiping, "Novel Nanostructures for SERS Biosensing," Nano Today 3.3-4, pp. 31-37, 2008.

[48] J. Yang, F. Ren, X. Chong, D. Fan, S. Chakravarty, Z. Wang, R. T. Chen and A. X. Wang, "Guided-Mode Resonance Grating with Self-Assembled Silver Nanoparticles for Surface-Enhanced Raman Scattering Spectroscopy," Photonics, pp. 380-389, 2014.

[49] Q. Zhou, Z. Li, Y. Yang and Z. Zhang, "Arrays of Aligned, Single Crystalline Silver Nanorods for Trace Amount Detection," J. Phys. D: Appl. Phys. 41, pp. 152007-1-4, 2008.

[50] N.A., "7 Plasmonics," in N.A., N.A., pp. 208-239.

[51] N.A., "Chapter 3: Mie Theory," in N.A., N.A., pp. 23-65.

[52] R. Sundararaman, P. Narang, A. S. Jermyn, W. A. I. Goddard and H. A. Atwater, "Theoretical Predictions for Hot-Carrier Generation from Surface Plasmon Decay," Nat. Commun. 5:5788 , pp. 1-8, 2014.

[53] Z.-Q. Tian, Z.-L. Yang, B. Ren and D.-Y. Wu, "SERS From Transition Metals and Excited by Ultraviolet Light," Surface-Enhanced Raman Scattering Topics and Applied Physics, pp. 125-46, n.d..

[54] H. Wei and H. Xu, "Plasmonics in Composite Nanostructures," Materials Today 17-8, pp. 372-380, 2014.

[55] M. W. Knight, L. Liu, Y. Wang, L. Brow, S. Mukherjee, N. S. King, H. O. Everitt, P. Norlander and N. J. Halas, "Correlating Nanorod Structure with Experimentally Measured and Theoretically Predicted Surface Plasmon Resonance," ACS Nano 4.9, pp. 5453-463, 2010.

[56] NanoHybrids, "NanoHybrids," 2017. [Online]. Available: https://nanohybrids.net/pages/plasmonics.

[57] C. Li, W. Ji, J. Chen and Z. Tao, "Metallic Aluminum Nanorods: Synthesis via Vapor-Deposition and APplications in Al/air Batteries," Chem. Mater. 19.24, pp. 5812-814, 2007.

[58] K. R. Beavers, N. E. Marotta and L. A. Bottomley, "Thermal Stability of Silver Nanorod Arrays," Chem. Mater. 22, pp. 2184-2189, 2010.

[59] R. A. Andrievski, "Review: Stability of Nanostructured Materials," J. Mat. Sci. 38, pp. 1367-1375, 2003.

[60] S. Link, Z. L. Wang and M. A. El-Sayed, "How Does a Gold Nanorod Melt?," J. Phys. Chem. B 104, pp. 7867-7870, 2000.

[61] M. Jose´-Yacama´n, C. Gutierrex-Wing, M. Miki, D.-Q. Yang, K. N. Piyakis and E. Sacher, "Surface Diffusion and Coalescence of Mobile Metal Nanoparticles," J. Phys. Chem. B 109, pp. 9703-9711, 2005.

[62] V. A. Lavrenko, A. I. Malyshevskaya, L. I. Kuznetsova, V. F. Litvinenko and V. N. Pavlikov, "Features of High-Temperature Oxidation in Air of Silver and Alloy Ag-Cu, and Adsorption of Oxygen on Silver," Powd. Metallurg. Metal Ceram. 45, pp. 476-480, 2006.

[63] C. L. Kou and K. C. Hwang, "DOes Morphology of a Metal Nanoparticle Play a Role in Ostwald Ripening Processes?," Chem. Mater. 25, pp. 365-371, 2013.

[64] X. Zhang, J. Zhao, A. V. Whitney, J. W. Elam and R. P. Van Duyne, "Ultrastable Substrates for Surface-Enhanced Raman Spectrscopy: Al2O3 Overlayers Fabricated by Atomic Layer Deposition Yield Improved Anthrax Biomarker Detection," J. Am. Chem. Soc. 128.31, pp. 10304-0309, 2006.

[65] L. Ma, Y. Huang, M. Hou, Z. Xie and Z. Zhang, "Ag Nanorods Coated with Ultrathin TiO2 Shells as Stable and Recyclable SERS Substrates," Sci. Rep. 5, pp. 1-8, 2015.

[66] S. P. Stagon, T. Xuefei, Y. Liu and H. Huang, "Controllable Growth of Al Nanorods for Inexpensive and Degradation-Resistant Surface Enhanced Raman Spectroscopy".

[67] M. M. Hawkeye, M. T. Taschuk and M. J. Brett, "Chapter 13- Glancing Angle Deposition," in Glancing Angle Deposition of Thin Films: Engineering the Nanoscale, pp. 621-78.

[68] S. P. Stagon and H. Huang, "Controllable Growth of Aluminum Nanorods Using Physical Vapor Deposition," Nanoscale Res Lett 9.1, p. 400, 2014.

[69] M. T. Taschuk, M. M. Hawkeye and M. J. Brett, "Chapter 13: Glancing Angle Deposition," in N.A., Elsevier Inc., 2010, pp. 621-678.

[70] K. M. McPeak, S. V. Jayanti, S. J. P. Kress, S. Meyer, S. Iotti, A. Rossinelli and D. J. Norris, "Plasmonic Films Can Easily Be Better: Rules and Recipes," ACS Photonics 2, pp. 326-333, 2015.

[71] Kurt J. Lesker, "Kurt. J. Lesker Deposition Materials," [Online]. Available: http://www.lesker.com/newweb/menu_depositionmaterials.cfm?section=evapmats&init= skip.

[72] D. A. Owen, "Tutorial on UV-Visible Spectroscopy," Agilent Technologies, 2000. [Online]. Available: http://www.agilent.com/cs/Satellite?assetid=1404943754587&assettype=GSA_C&d=To uch&formassembly=false&pagename=Agilent%2FGSA_C%2FGenericInnerTemplateWi thFourZones_New.

[73] S. P. Stagon and H. Huang, "Airtight metallic sealing at room temperature under small mechanical pressure," Sci. Rep. 3, pp 3066, 2013

[74] NIH, "Image J image Processing and Analysis in Java," [Online] Available: https://imagej.nih.gov/ij/

APPENDIX A: WATANABE'S CALCULATED DATA FOR R6G VIBRATIONAL MODES

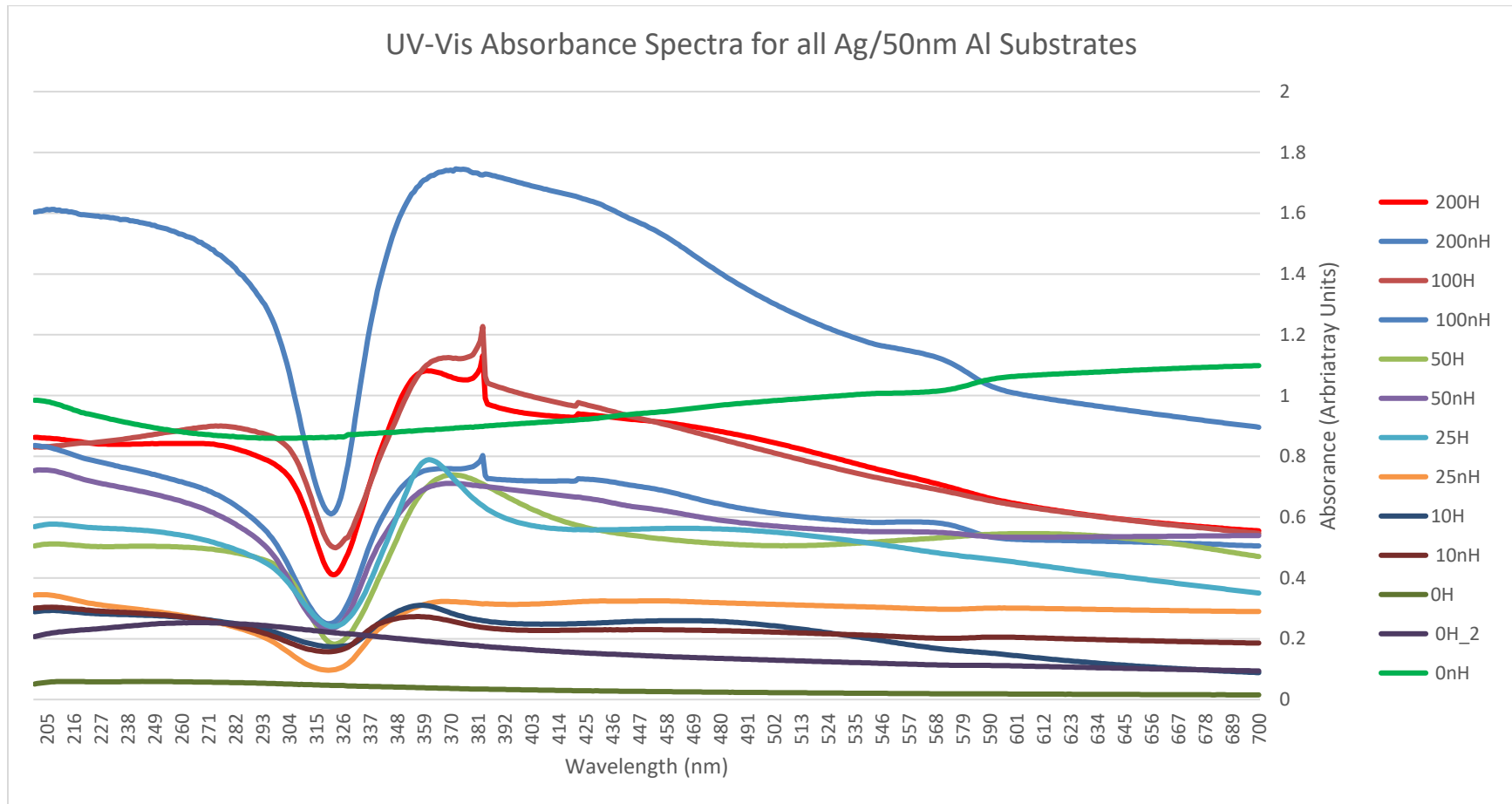Table 2: Calculated and Experimental Vibrational Frequencies for R6G [1]

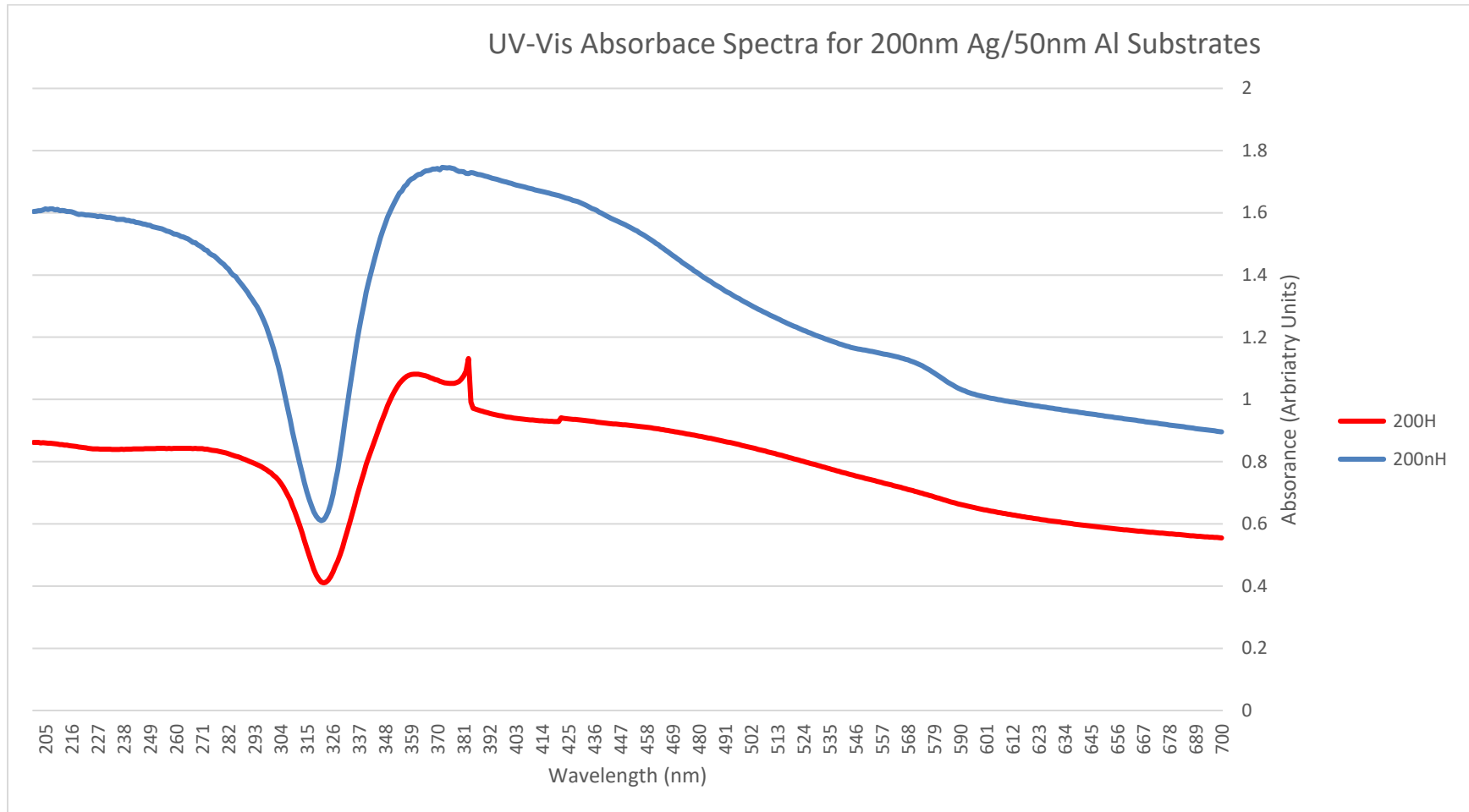| mode	B3LYP/6-311++G(d,p)[a] v (cm^{-1})	Raman int.	IR int.	experimental v (cm^{-1}) Raman	IR	PED%[b] X,A,M,P	mode	B3LYP/6-311++G(d,p)[a] v (cm^{-1})	Raman int.	IR int.	experimental v (cm^{-1}) Raman	IR	PED%[b] X,A,M,P
52	610	1.9	43.8		611	X(65),A(20),P(12	104	1191	26.2	43.9		1181	X(88),A(11)
53	615	9.7	12.1	613	615	X(49),P(48)	105	1192	135.7	10.4	1202		X(40),A(10),P(47)
54	631	14.4	3.9	639		X(85),P(14)	106	1239	12.0	177.5		1235	A(13),P(87)
55	664	7.9	5.6	660		X(20),P(80)	107	1259	37.8	380.8		1250	X(39),P(55)
56	673	0.1	2.0	679		X(93)	108	1263	20.6	241.3		1255	X(42),A(11),P(47)
57	697	2.0	1.0			X(86)	109	1265	5.4	27.0			X(71),A(28)
58	702	2.7	0.6	705		X(46),P(52)	110	1271	3.5	4.1			P(95)
59	705	1.6	9.9	705		X(11),P(83)	111	1273	5.2	2.4	1278		P(100)
60	714	1.0	2.1			X(95)	112	1291	149.6	16.2	1294		X(53),A(40)
61	723	1.9	27.0	725	730	X(57),A(33)	113	1301	10.5	38.2			A(17),P(76)
62	737	1.5	17.7	735	740	X(42),P(39)	114	1301	5.9	188.4		1296	X(28),A(72)
63	753	18.5	7.4	741		X(92)	115	1307	119.1	26.9	1312		X(30),A(48),P(21)
64	757	16.6	0.0	746		X(41),A(52)	116	1314	13.9	1197.8		1313	X(59),A(38)
65	771	12.4	0.9	775		X(75),A(11),M(12)	117	1351	351.7	1.4	1364		X(70),A(17)
66	778	1.4	11.1			X(20),A(14),P(60)	118	1360	61.4	93.1		1367	X(17),A(80)
67	794	0.2	0.1			P(98)	119	1365	6.5	11.5			X(43),A(53)
68	803	0.4	14.2			X(16),A(62),P(22)	120	1373	4.7	9.6			P(100)
69	810	0.4	0.1			P(89)	121	1373	20.0	16.4			X(57),A(40)
70	819	6.2	1.7	833		X(35),A(45),P(11)	122	1388	68.0	19.6	1389	1387	A(94)
71	830	0.1	0.2			X(98)	123	1388	23.1	2.6	1389		A(99)
72	830	0.3	42.8		845	X(97)	124	1390	65.0	1.9	1389		M(87)
73	851	11.6	6.2	856		P(95)	125	1392	19.3	2.8	1389		M(95)
74	865	5.1	7.1			P(92)	126	1400	7.0	10.3			P(100)
75	887	11.3	0.3	885		A(86)	127	1419	141.1	119.1	1422	1421	X(69),M(17)
76	891	2.7	4.6			X(10),A(86)	128	1432	17.1	71.0		1446	X(55),A(26),M(17)
77	895	0.4	0.1			X(40),P(51)	129	1445	10.4	7.0			P(96)
78	895	2.7	17.0	903		X(93)	130	1457	9.1	9.0			P(100)
79	897	0.4	0.1			X(54),P(42)	131	1458	37.9	40.4	1450	1452	X(16),A(42),M(42)
80	923	3.8	2.6	936		X(54),A(14),P(32)	132	1458	8.1	16.2			M(97)
81	952	1.3	1.9			X(66),M(20)	133	1459	28.7	21.7			A(15),M(77)
82	978	0.0	0.3			P(97)	134	1462	3.5	1.8			A(95)
83	1004	21.2	1.7	1013		M(79),X(20)	135	1464	5.8	4.9			X(10),A(53),M(37)
84	1007	2.4	46.6		1019	P(100)	136	1466	9.0	29.6			A(94)
85	1011	0.3	2.4			P(98)	137	1467	24.8	0.5	1472		A(97)
86	1014	11.7	94.2	1022	1027	M(58),A(11),P(28)	138	1468	9.8	3.8			P(100)
87	1036	67.8	4.8	1042		X(20),A(68),P(10)	139	1476	2.7	56.3		1477	X(49),A(30),M(21)
88	1042	0.3	1.2			X(21),M(78)	140	1480	46.2	6.5	1490		X(19),M(54),P(20)
89	1042	0.3	0.0			X(21),M(78)	141	1482	44.6	13.0	1490		A(91)
90	1047	20.8	5.2	1061		P(91)	142	1482	4.7	22.8			X(11),A(89)
91	1049	37.7	6.1	1061		X(20),A(78)	143	1486	8.8	11.7			X(10),M(13),P(77)
92	1077	12.1	65.8		1081	A(54),P(36)	144	1488	14.4	3.8			P(94)
93	1084	19.3	130.9	1091		A(37),P(57)	145	1500	7.0	768.8		1501	X(80),M(13)
94	1085	9.0	60.9			A(92)	146	1505	692.0	32.8	1512		X(69),A(25)
95	1110	8.9	8.0	1121	1119	P(98)	147	1530	109.3	369.4	1533	1529	X(87),A(12)
96	1125	47.3	5.7	1130	1129	X(44),A(32),P(14)	148	1554	16.2	77.8			X(72),A(26)
97	1131	3.3	8.0			X(31),A(67)	149	1559	8.2	377.0		1566	X(46),A(54)
98	1137	7.9	17.7	1141		X(21),A(70)	150	1567	89.3	197.1	1559	1557	X(66),A(33)
99	1148	4.1	111.0		1142	P(99)	151	1577	39.0	17.9	1577		P(99)
100	1151	0.3	2.3			P(100)	152	1601	95.0	5.0	1599		P(100)
101	1160	17.8	1.2	1168		X(62),A(22),M(16)	153	1615	103.4	1105.5	1609	1608	X(96)
102	1170	7.9	2.4			P(100)	154	1652	67.7	312.7	1651	1647	X(98)
103	1175	45.4	1.6	1184		X(82),A(14)	155	1716	50.3	292.5	1722	1718	P(100)

[a] Vibrational frequencies scaled by a single factor of 0.9982 are given. Raman intensities are given in units of Å^4 amu$_{-1}$, and infrared intensities in units of km mol$_{-1}$. [b] Percentage of potential energy distribution (PED%) of normal mode of vibration is given. X refers to the motion of the xanthene ring. A refers to the motion of the NHC$_2$H$_5$ groups. M refers to that of a pair of methyl group adjacent to the xanthene ring. P refers to that of the phenyl ring with the COOC$_2$H$_5$ group. PED% less than 10% is omitted.
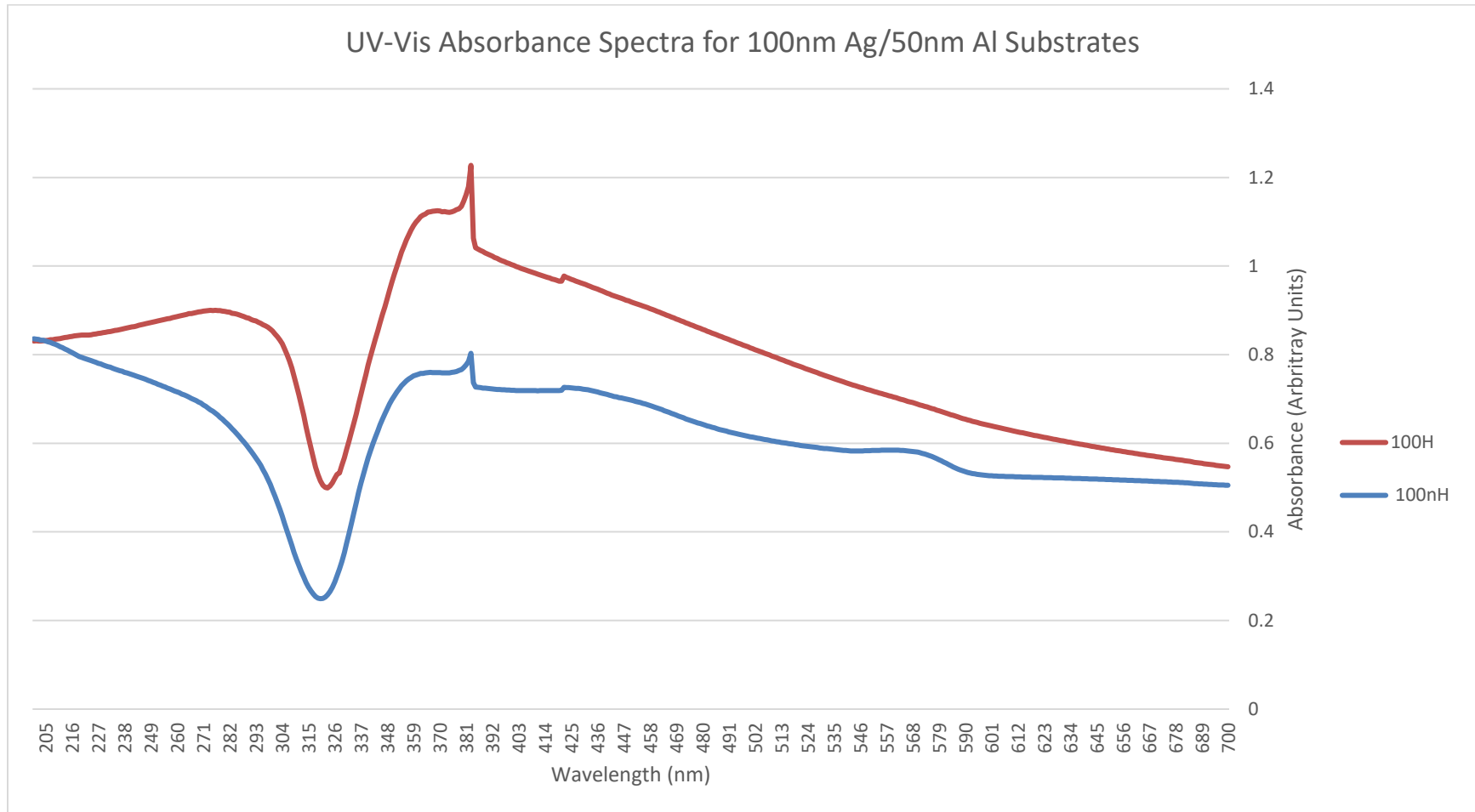
Table 3: Various calculated and experimental vibrational modes for R6G for off resonant Raman, Resonant Raman, Surface Enhanced Raman, and Tip Enhanced

Raman Spectroscopies [1]

|		experiment[b]								
	calc[a]	off-res Raman		RRS		SERRS		TERS	
mode	ν (cm^{-1})	ν (cm^{-1})	rel int	ν (cm^{-1})	rel int	ν (cm^{-1})	rel int	ν (cm^{-1})	rel int
53	615	613	0.32	611	1.00	612	0.87	608	0.30
54	631	639	0.00	641	0.00	637	0.03		
55	664	660	0.03	657	0.13	660	0.04		
56	673	679	0.07	675	0.03				
58	702 }	705	0.09	712	0.11	704	0.02	702	0.15
59	705 }								
65	771	775	0.16	775	0.58	772	0.33	766	0.30
70	819	833	0.01	826	0.03	830	0.01	808	0.03
78	895	903	0.01	912	0.05	902	0.01		
80	923	936	0.00	934	0.03	931	0.04	919	0.04
86	1014	1022	0.00	1025	0.03	1022	0.01	1027	0.30
90	1047 }	1061	0.01			1054	0.002	1054	0.35
91	1049 }								
93	1084	1091	0.03			1090	0.07	1084	0.05
96	1125	1130	0.04	1127	0.06	1127	0.08	1120	0.35
103	1175	1184	0.25	1178	0.51	1185	0.31	1185	0.40
105	1192	1202	0.07	1200	0.07				
111	1273	1278	0.03	1275	0.04	1275	0.05	1269	0.90
112	1291	1294	0.07	1284	0.06				
115	1307	1312	0.47	1310	0.38	1311	0.31	1308	0.30
117	1351	1364	0.80	1361	0.88	1361	0.82	1359	0.70
122	1388 }	1389	0.07	1385	0.08	1383	0.08		
124	1390 }								
127	1419	1422	0.04	1422	0.10	1420	0.05		
131	1458	1450	0.04	1450	0.15	1448	0.07	1457	0.65
146	1505	1512	1.00	1505	0.50	1508	0.44	1503	0.30
147	1530	1533	0.11	1536	0.22	1538	0.33	1532	0.45
151	1577	1577	0.07	1577	0.41	1575	0.60	1570	0.70
152	1601	1599	0.09	1600	0.09	1598	0.10	1596	0.03
153	1615	1609	0.08	1612	0.06				
154	1652	1651	0.13	1649	1.00	1650	1.00	1647	1.00
155	1716	1722	0.04	1720	0.03				

APPENDIX B: UV-VIS SPECRA

UV-Vis Absorbance Spectra for all Ag/50nm Al Substrates

UV-Vis Absorbace Spectra for 200nm Ag/50nm Al Substrates

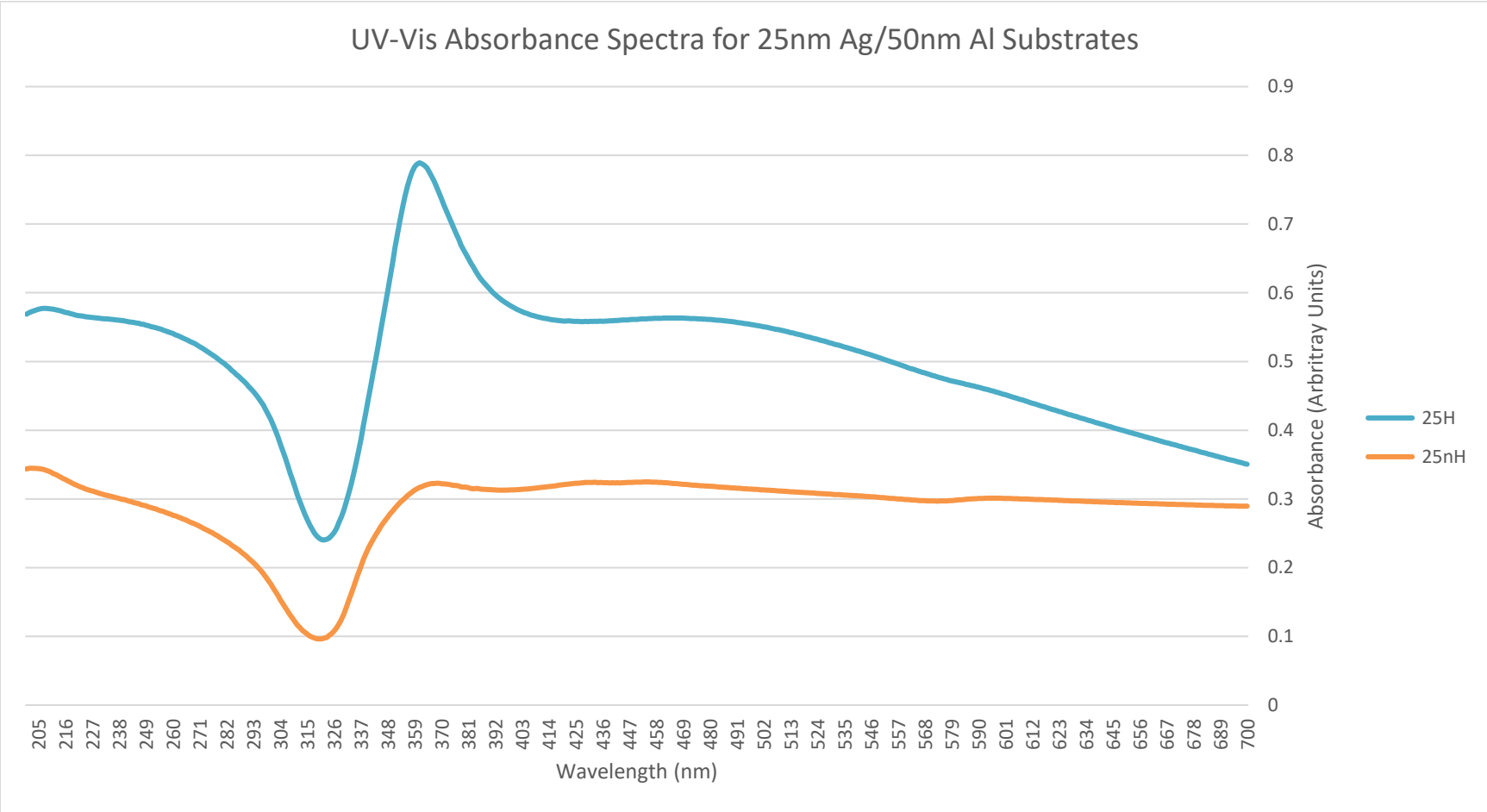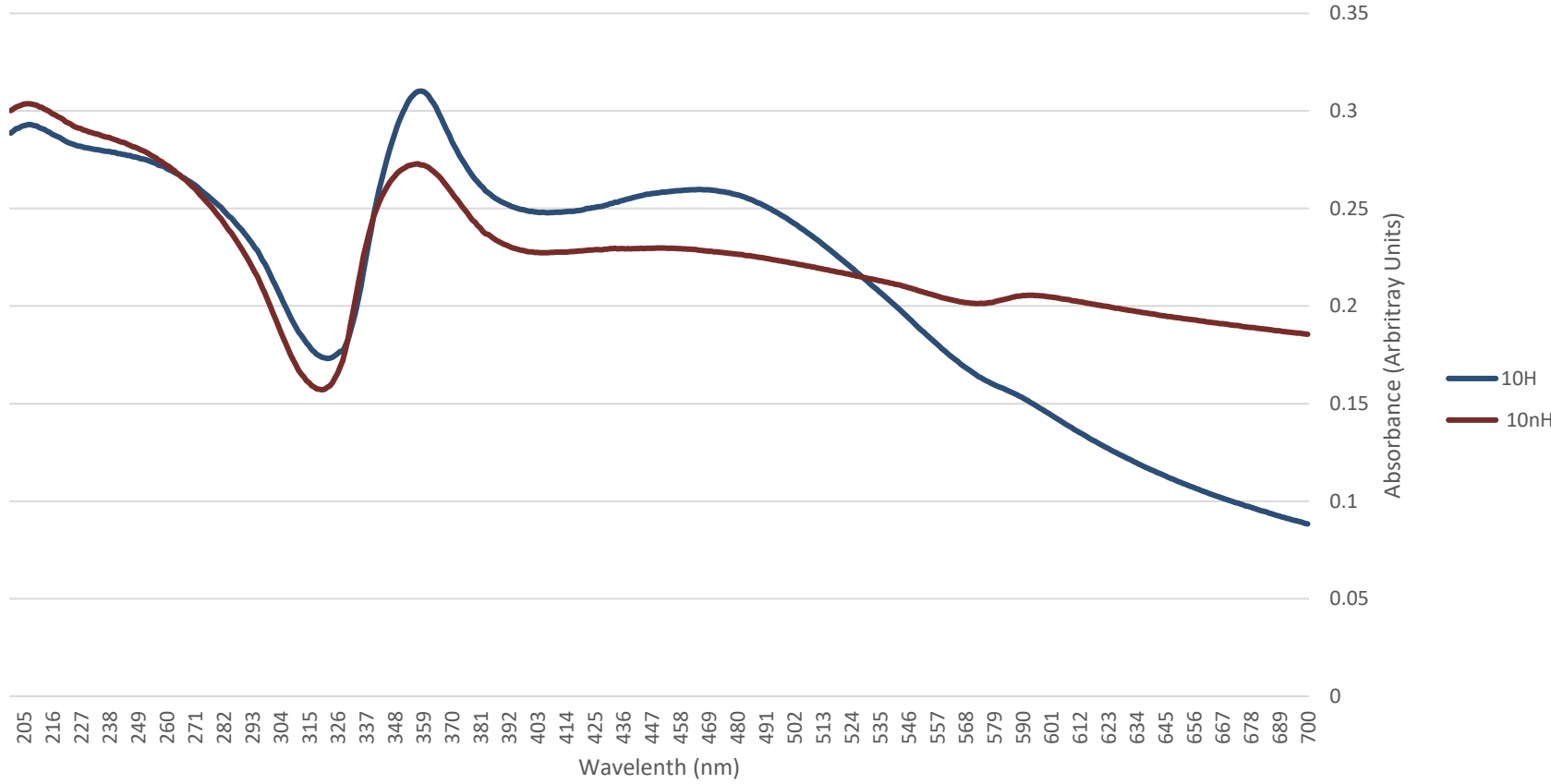UV-Vis Absorbance Spectra for 100nm Ag/50nm Al Substrates

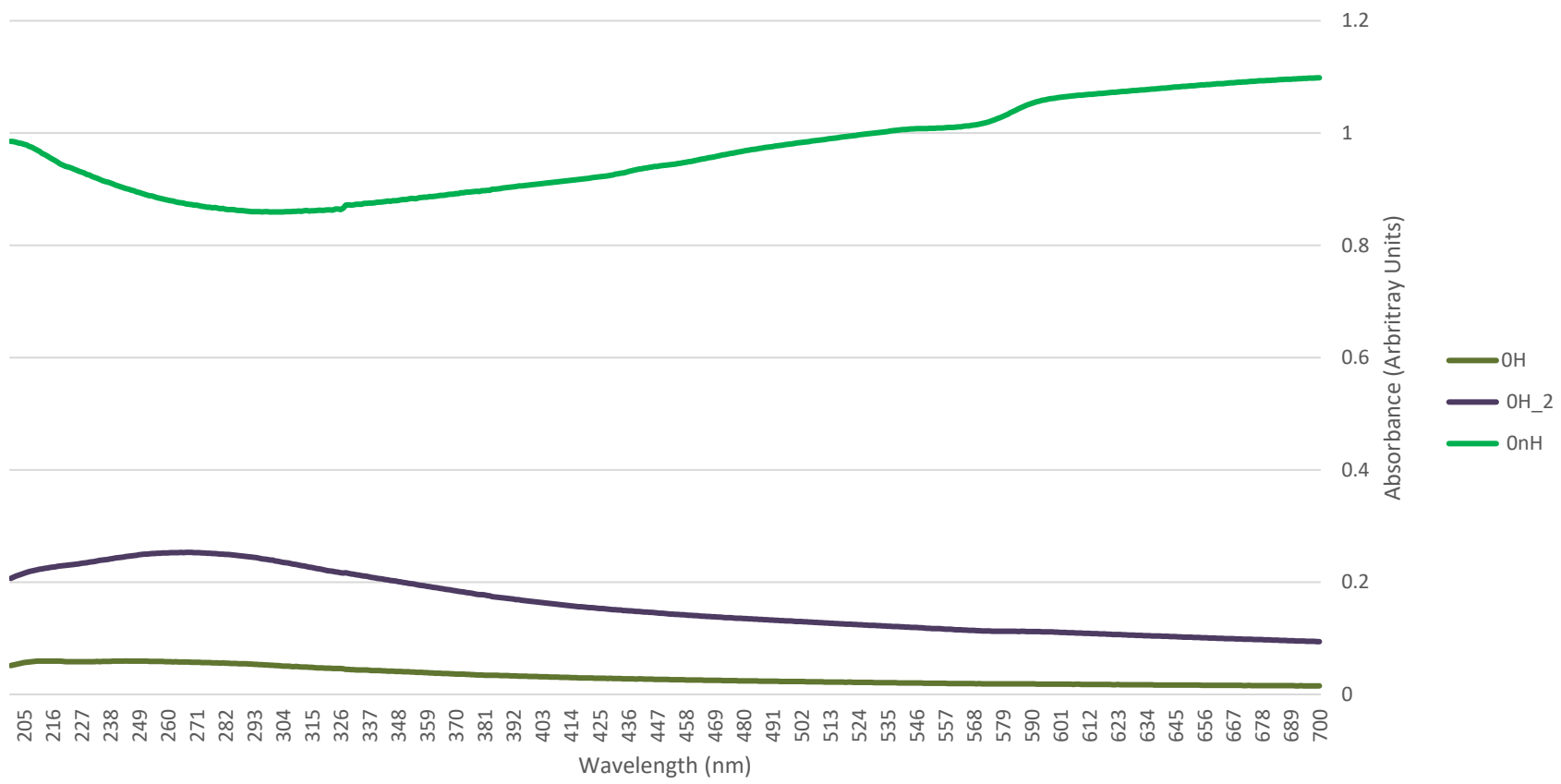UV-Vis Absorbance Spectra for 50nm Ag/50nm Al Substrates
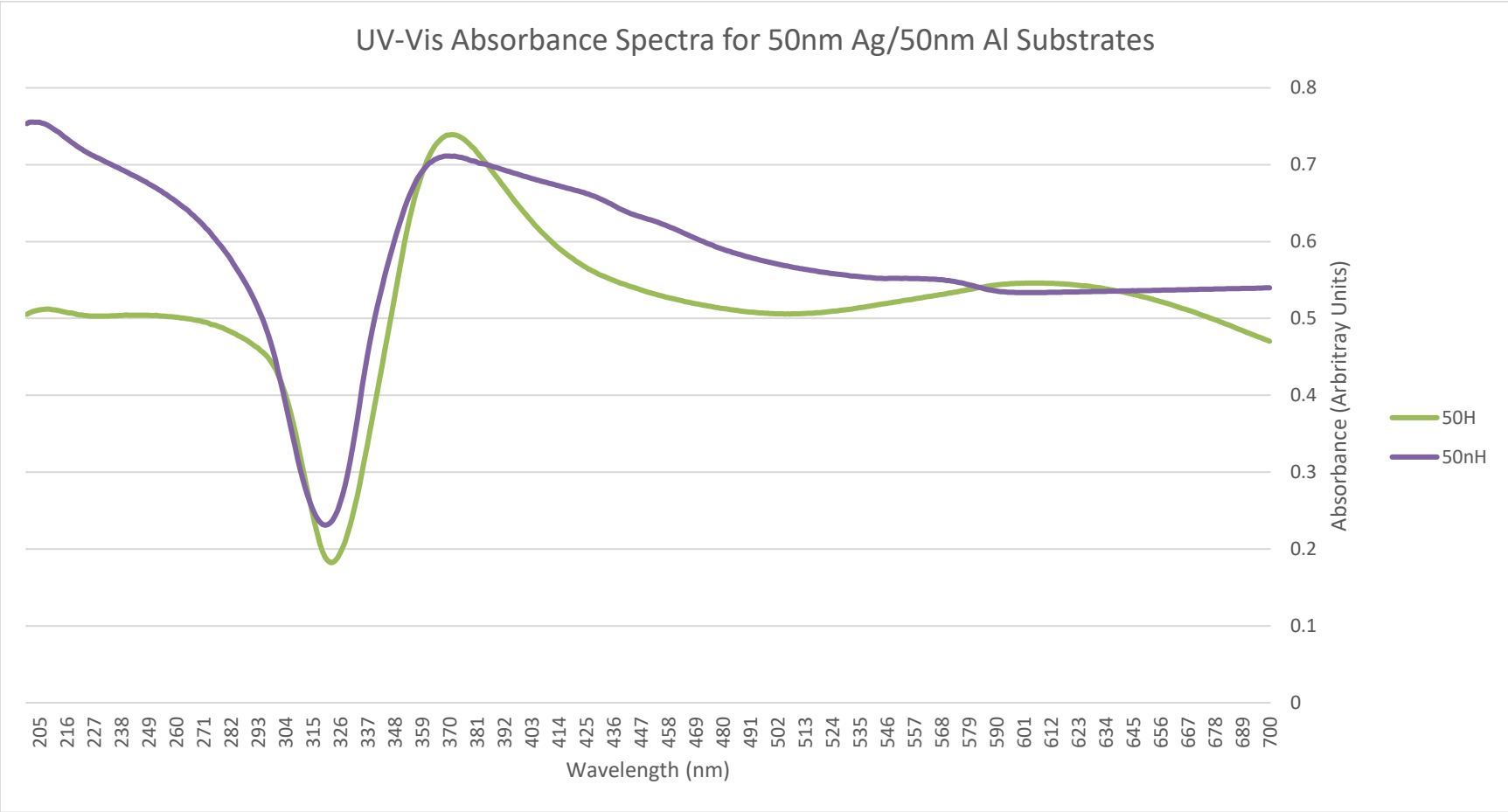
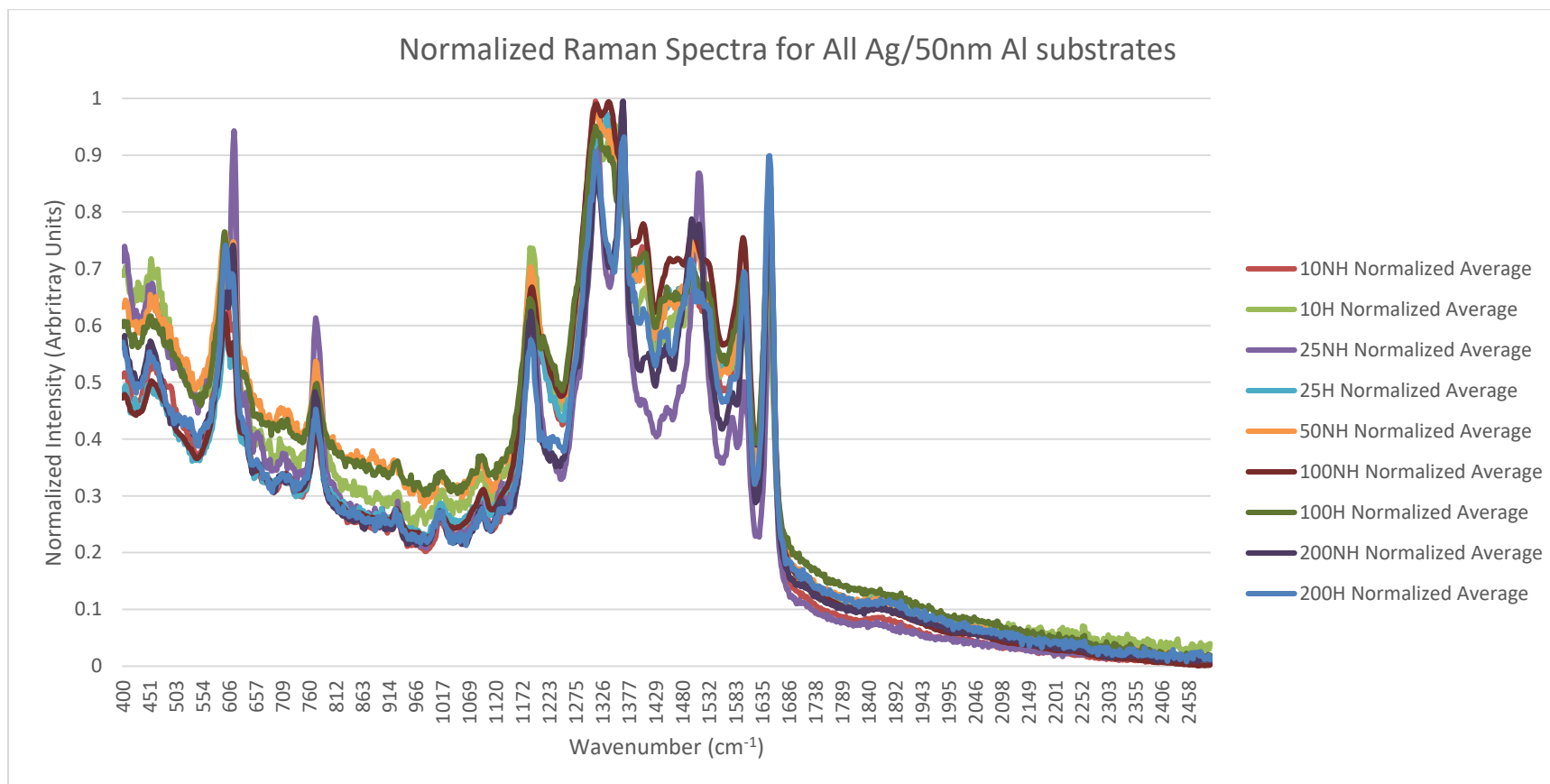UV-Vis Absorbance Spectra for 25nm Ag/50nm Al Substrates
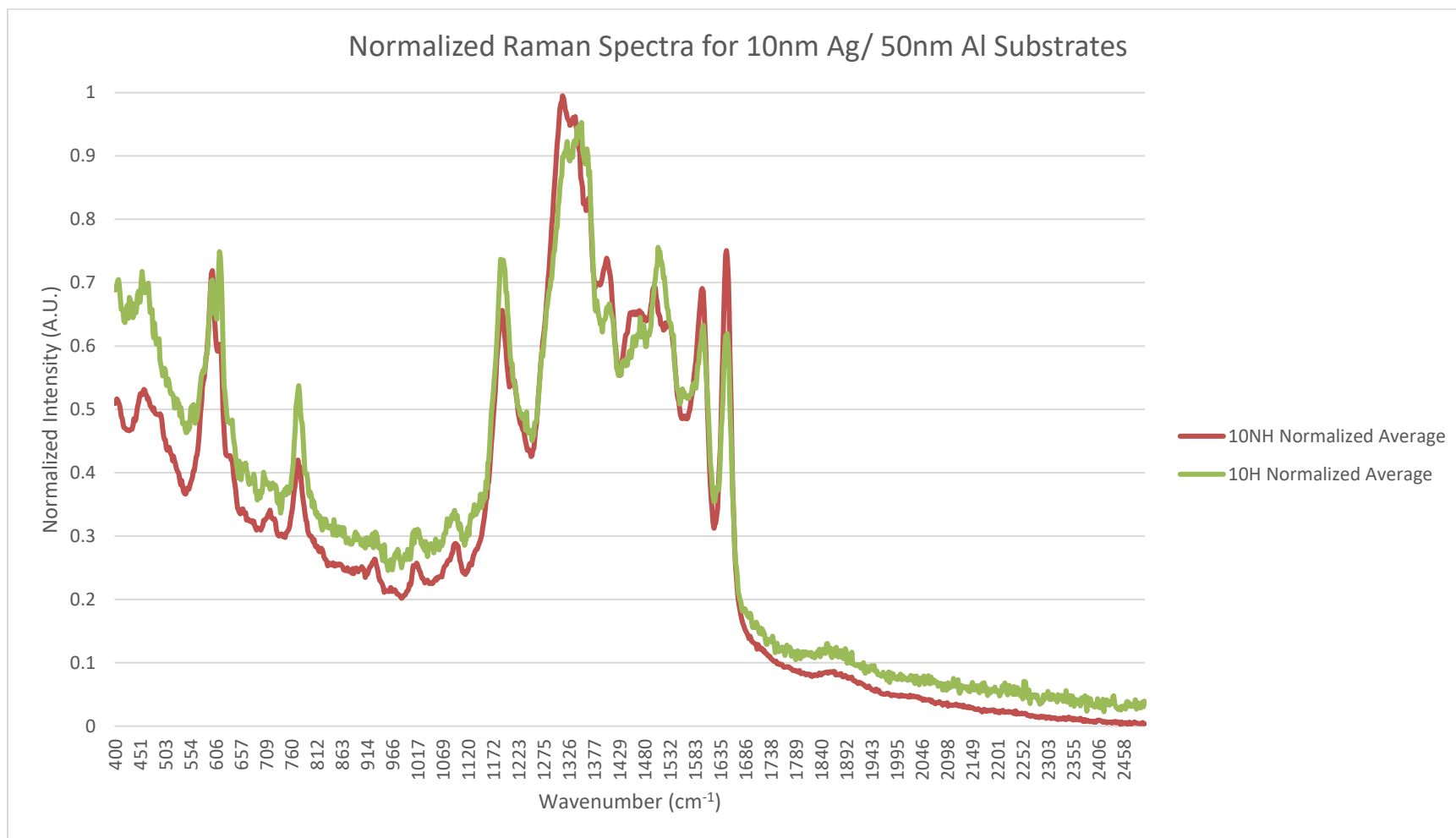
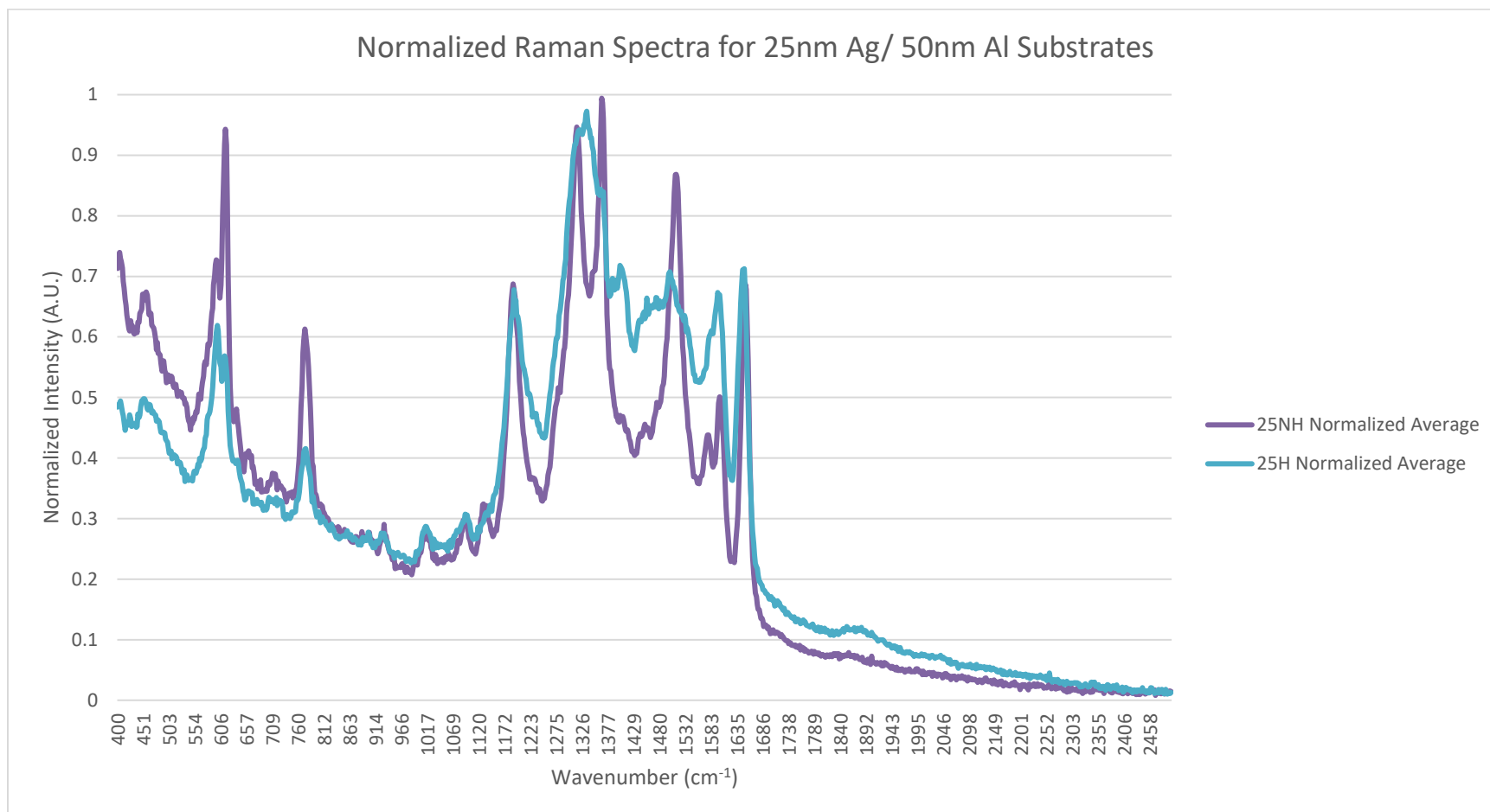UV-Vis Absorbance Spectra for 10nm Ag/50nm Al Substrates
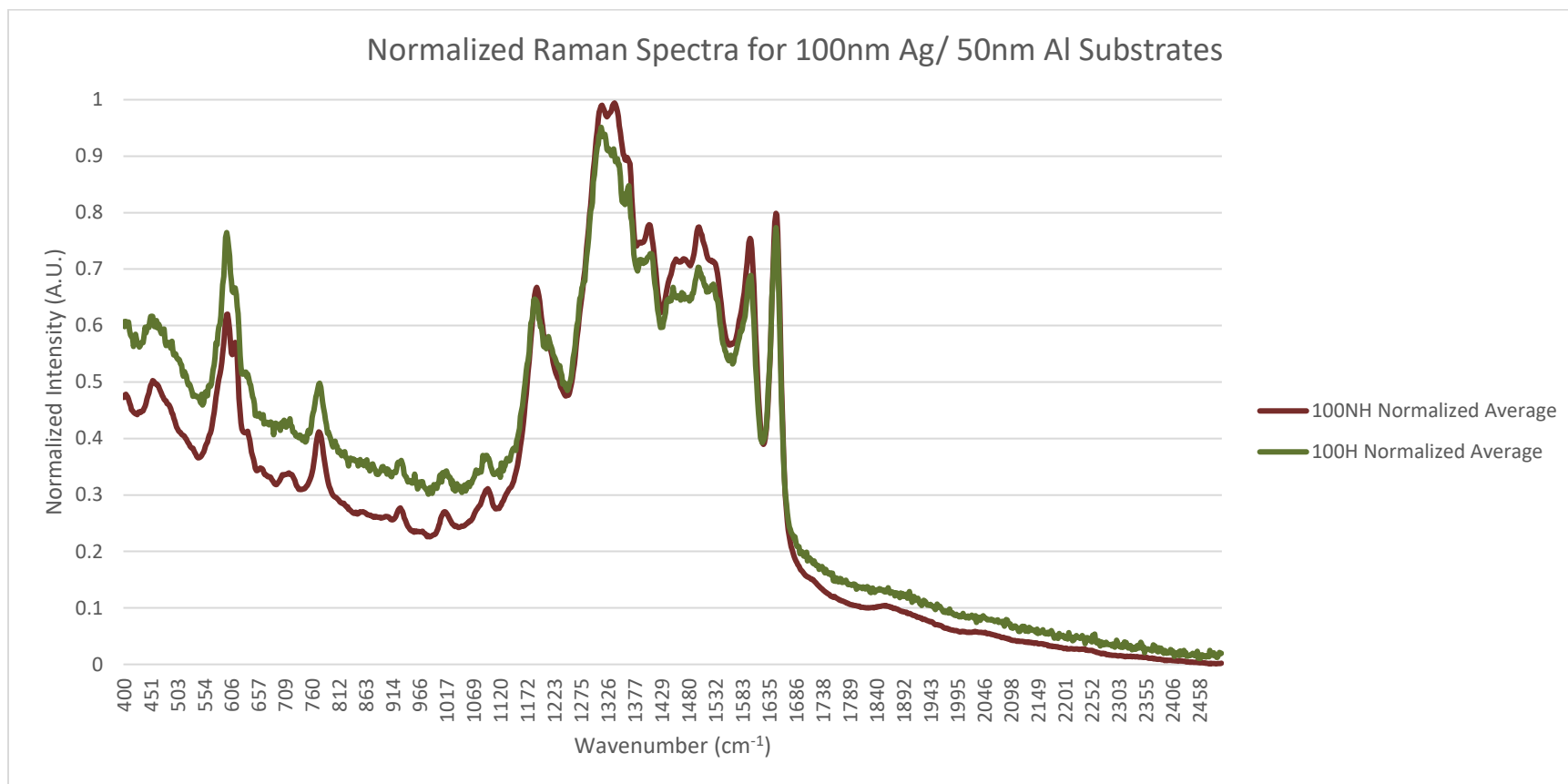
UV-Vis Absorbance Spectra for 50nm Al Substrates

APPENDIX C: RAMAN DATA FOR ALUMINUM/SILVER COMPOSITE SUBSTRATES

Normalized Raman Spectra for 10nm Ag/ 50nm Al Substrates

Normalized Raman Spectra for 25nm Ag/ 50nm Al Substrates

Normalized Raman Spectra for 50nm Ag/ 50nm Al Substrates

Normalized Raman Spectra for 100nm Ag/ 50nm Al Substrates

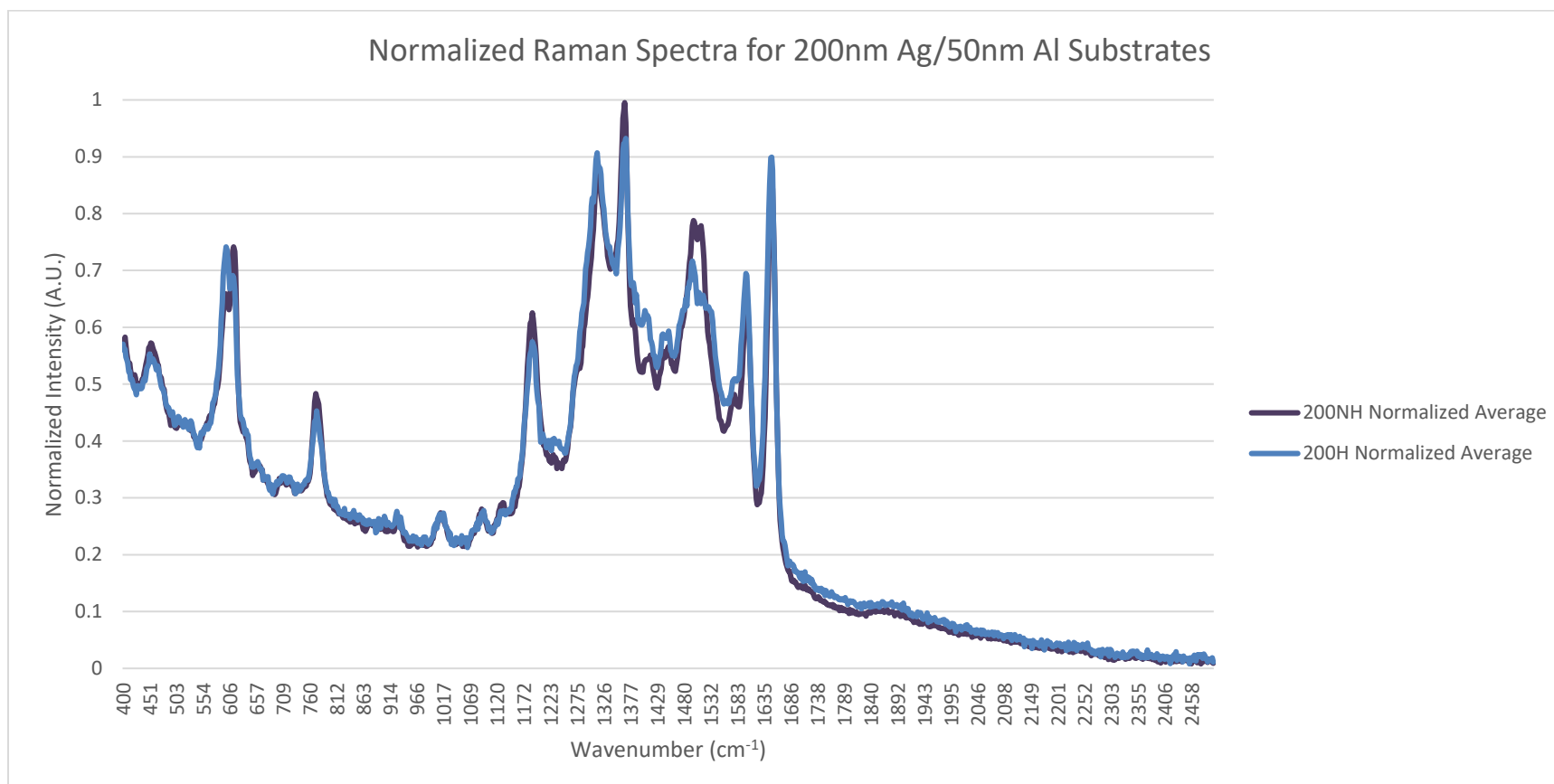Normalized Raman Spectra for 200nm Ag/50nm Al Substrates
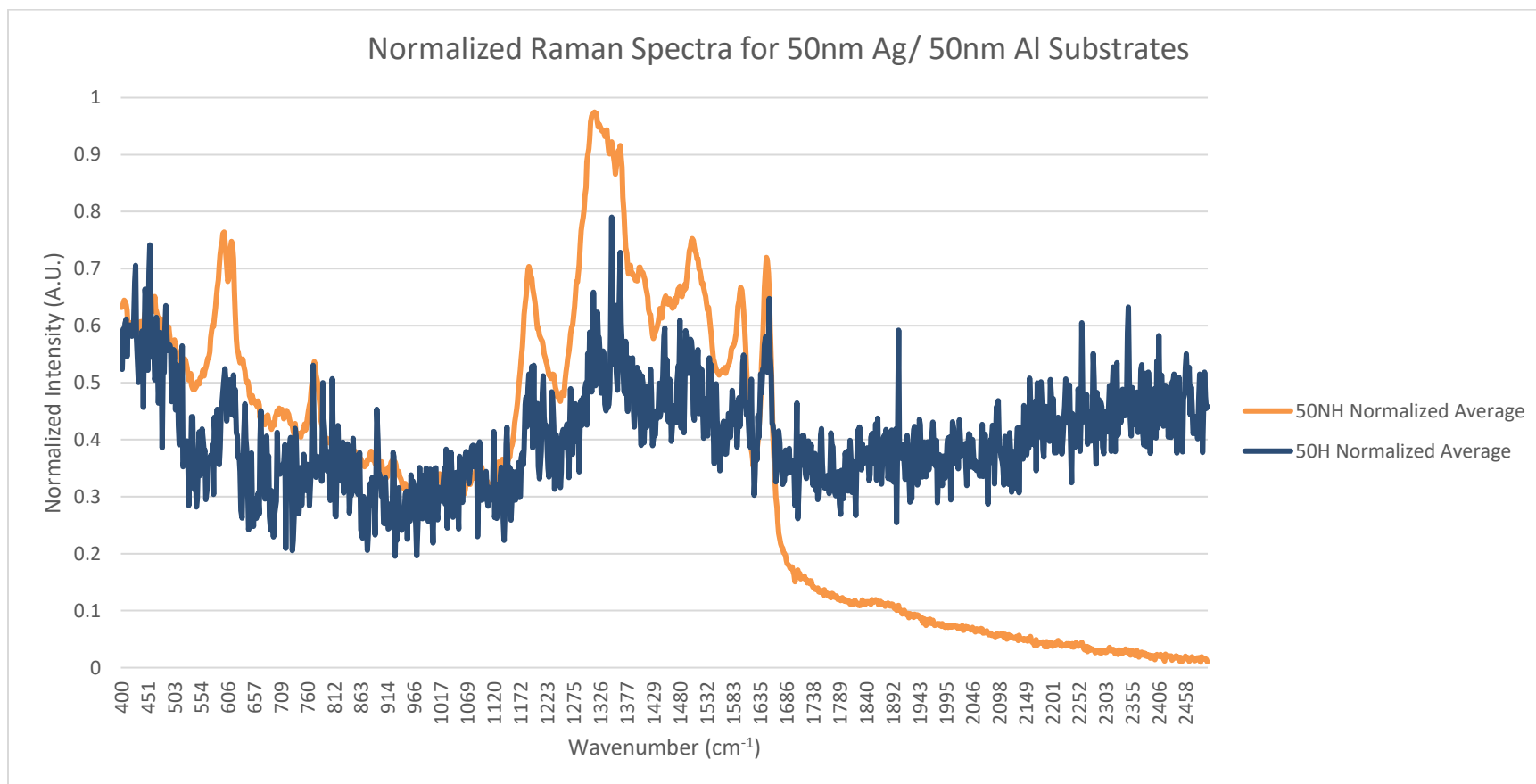
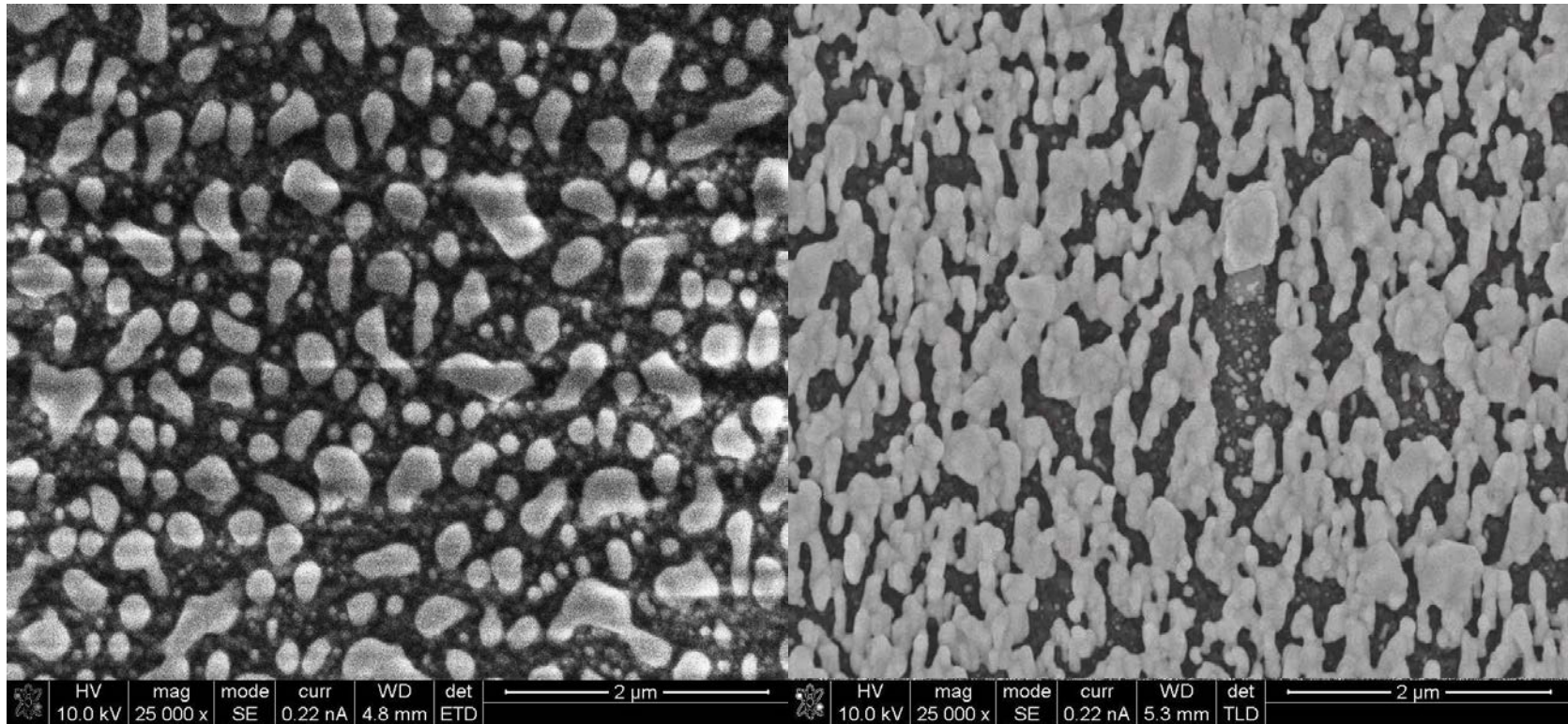APPENDIX D: SEM IMAGES FOR ALUMINUM/SILVER COMPOSITE SUBSTRATES

Figure 33: 200nm Silver nanorods on 50nm Aluminum seeds. Heated(left) and non-heated (right)
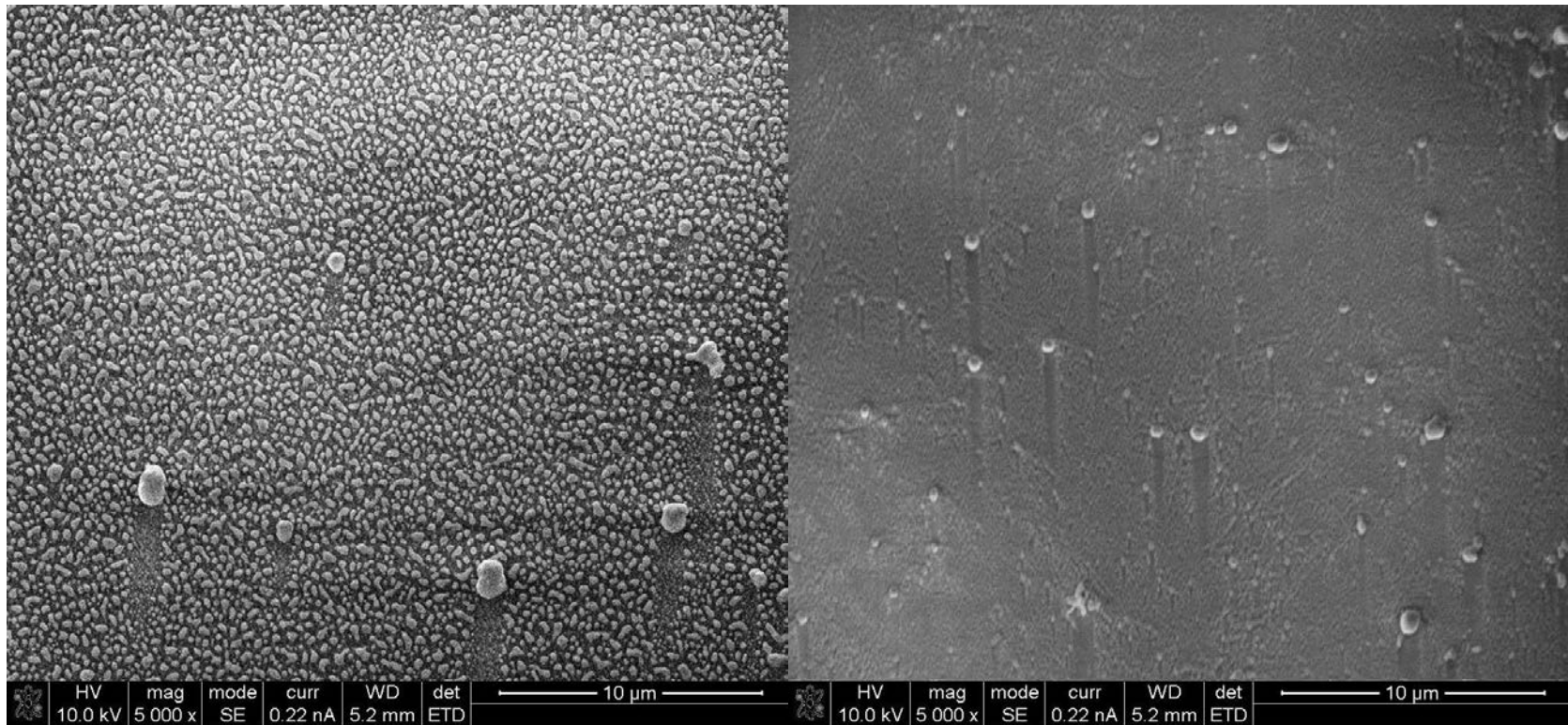
Figure 34:100nm Silver nanorods on 50nm Aluminum seeds. Heated(left) and non-heated (right)

Figure 35:100nm Silver nanorods on 50nm Aluminum seeds. Heated(left) and non-heated (right)

Figure 36:50nm Silver nanorods on 50nm Aluminum seeds. Heated (left) and non-heated (right)

Figure 37: 25nm Silver nanorods on 50nm Aluminum seeds. Heated (left) and non-heated (right)

Figure 38: 10nm Silver nanorods on 50nm Aluminum seeds. Heated (left) and non-heated (right)
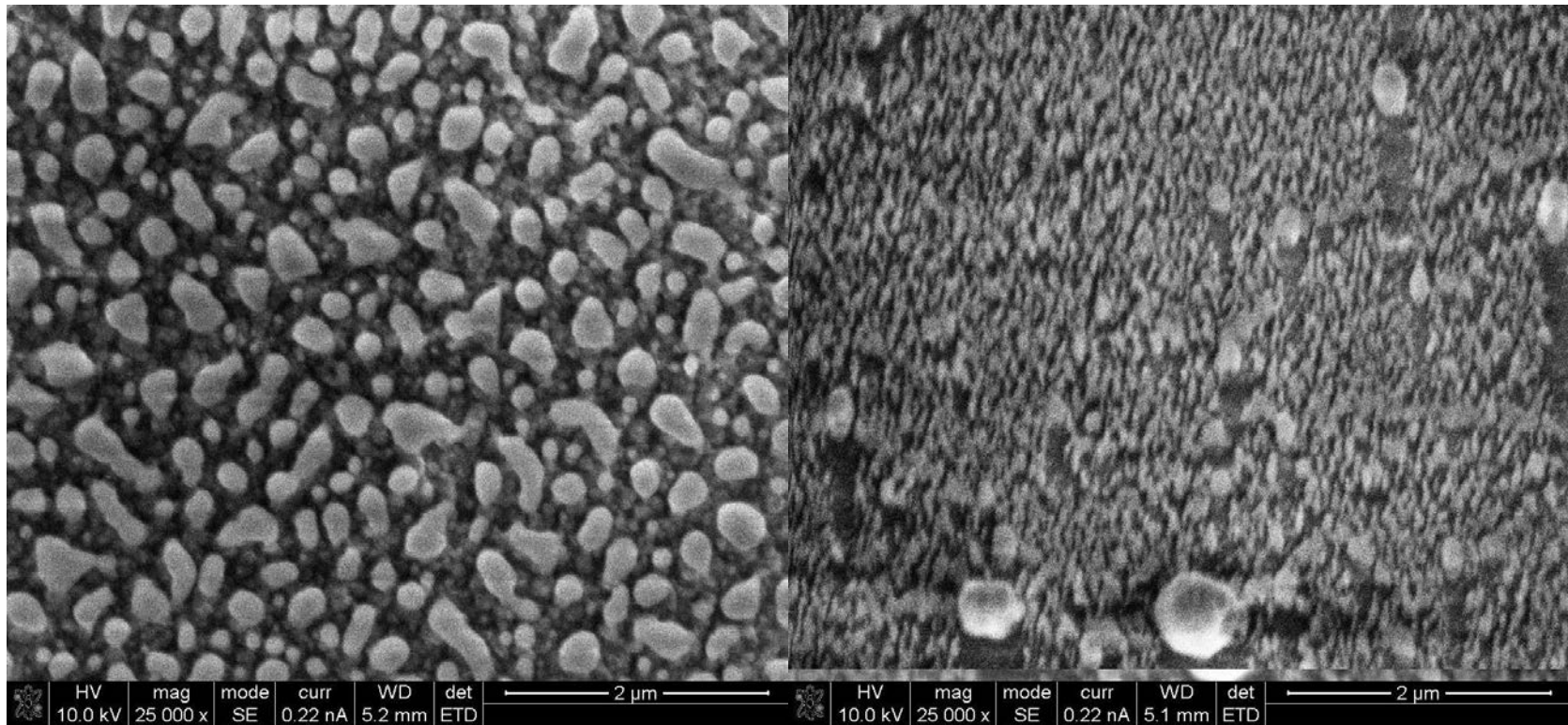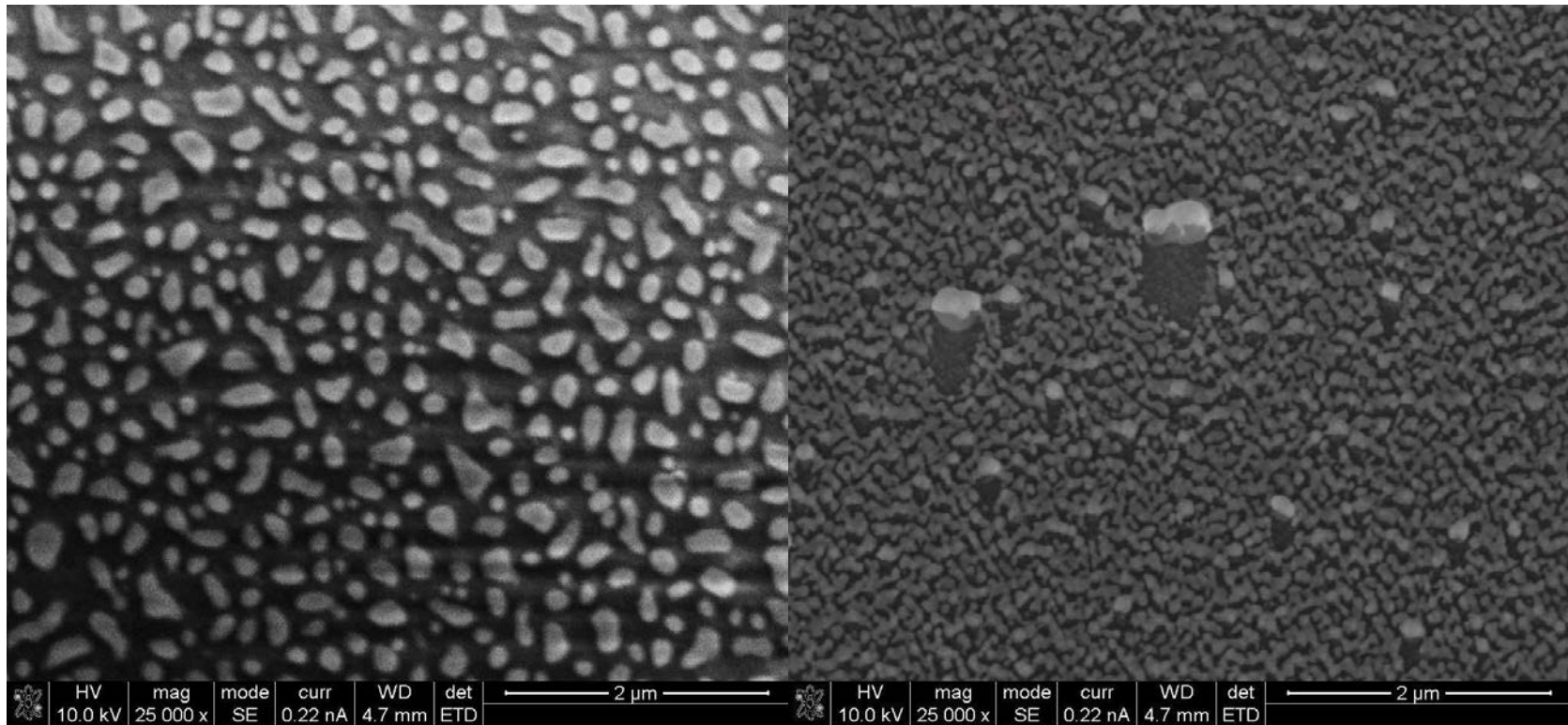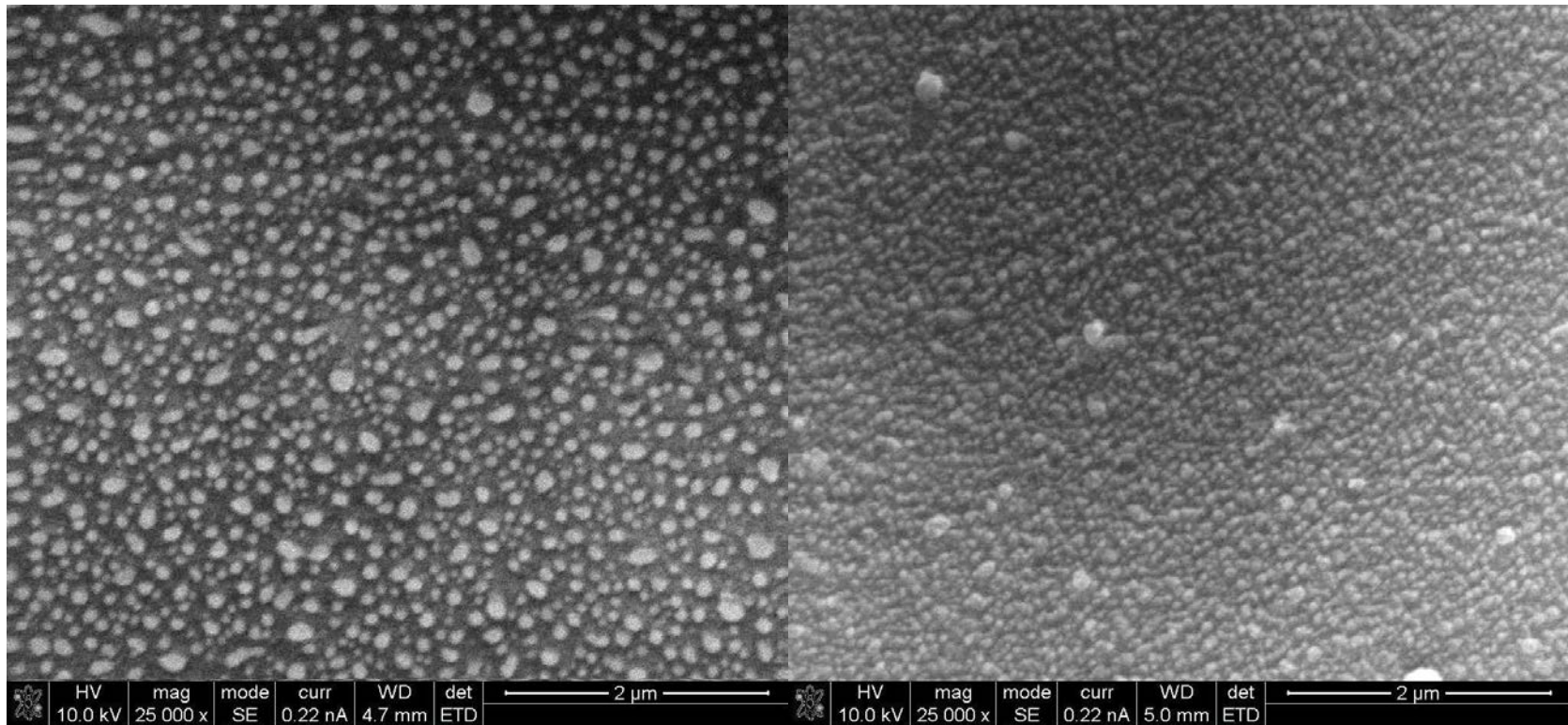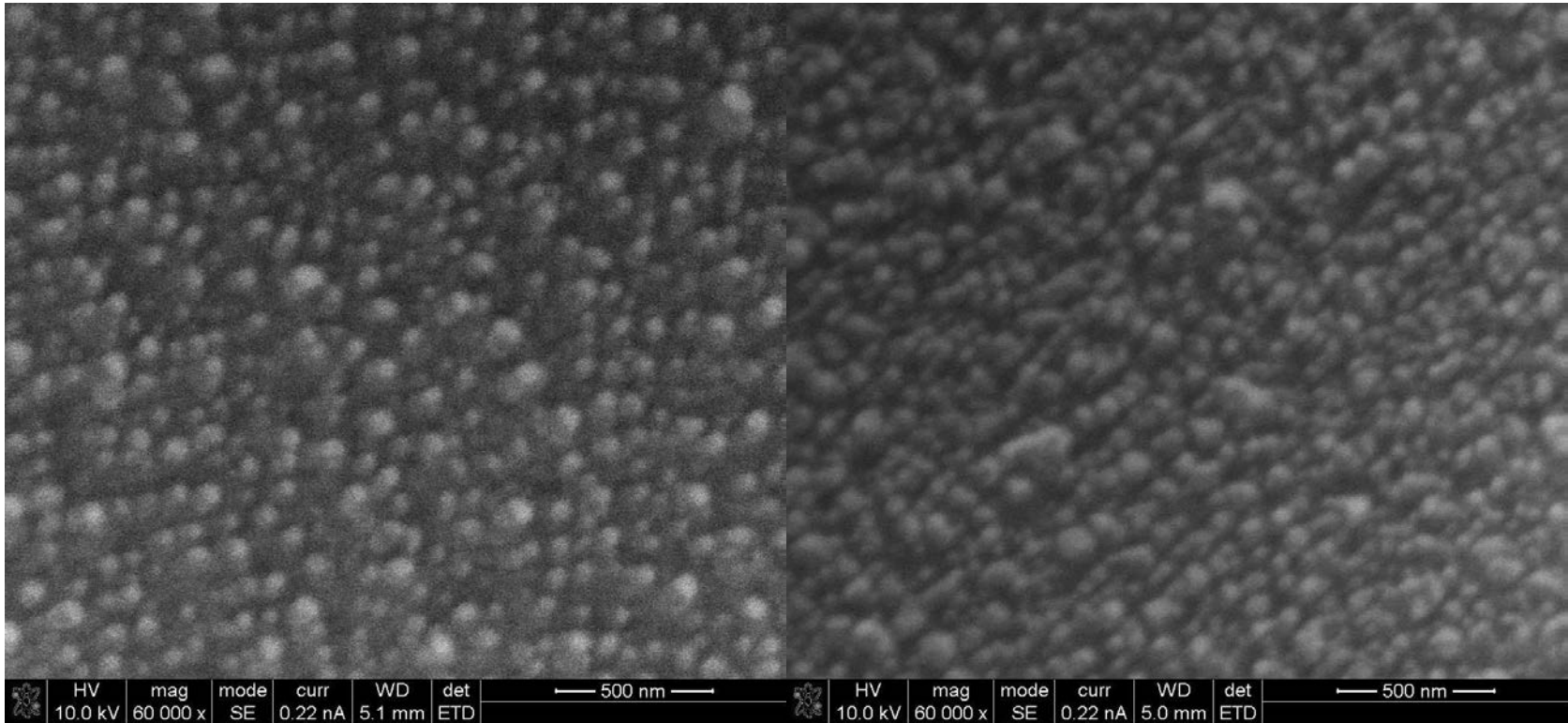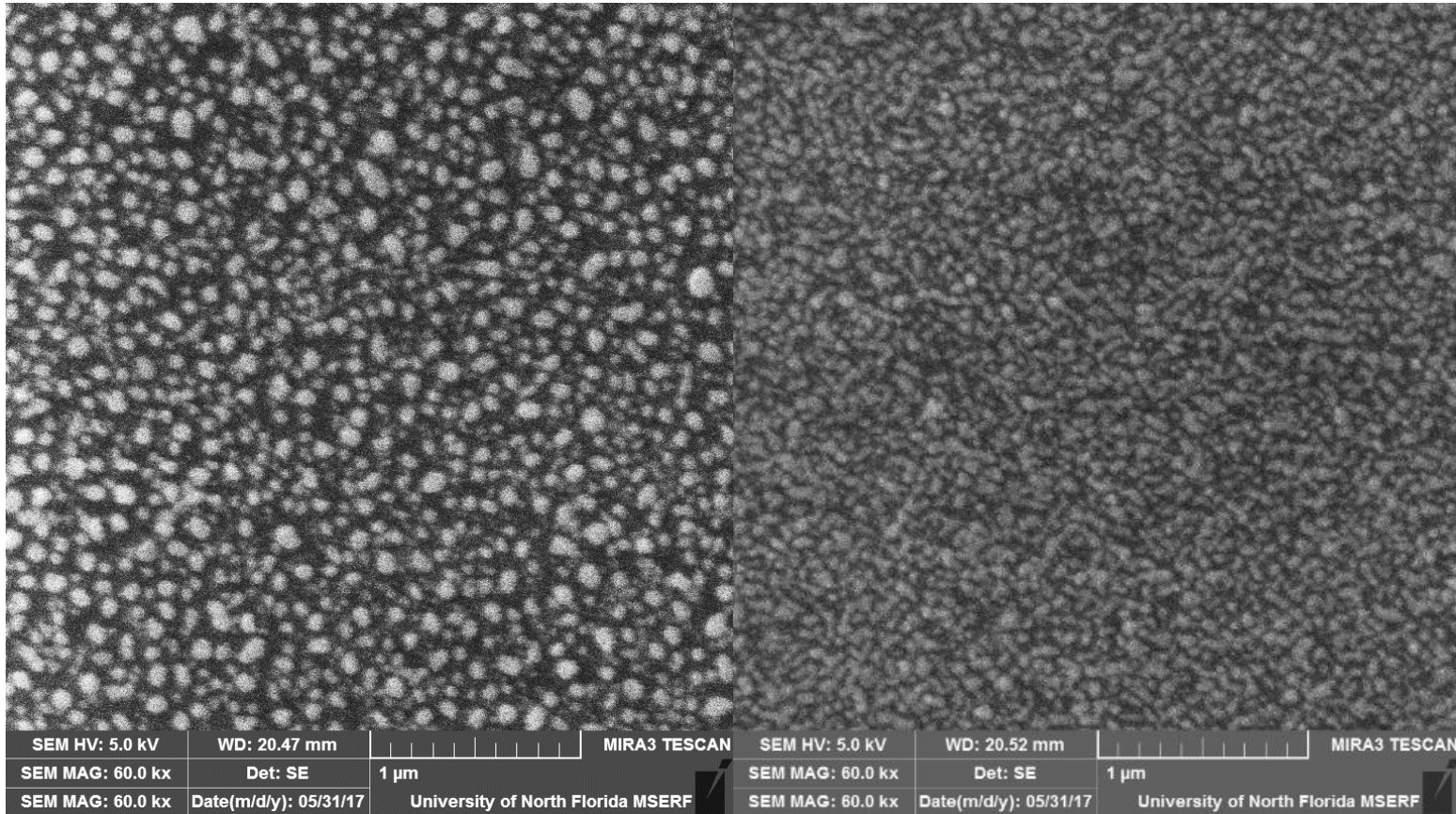
Figure 39: 100nm Ag nanorods on 50nm Al seeds. After 6months storage in air. Heated (left) and not heated (right)
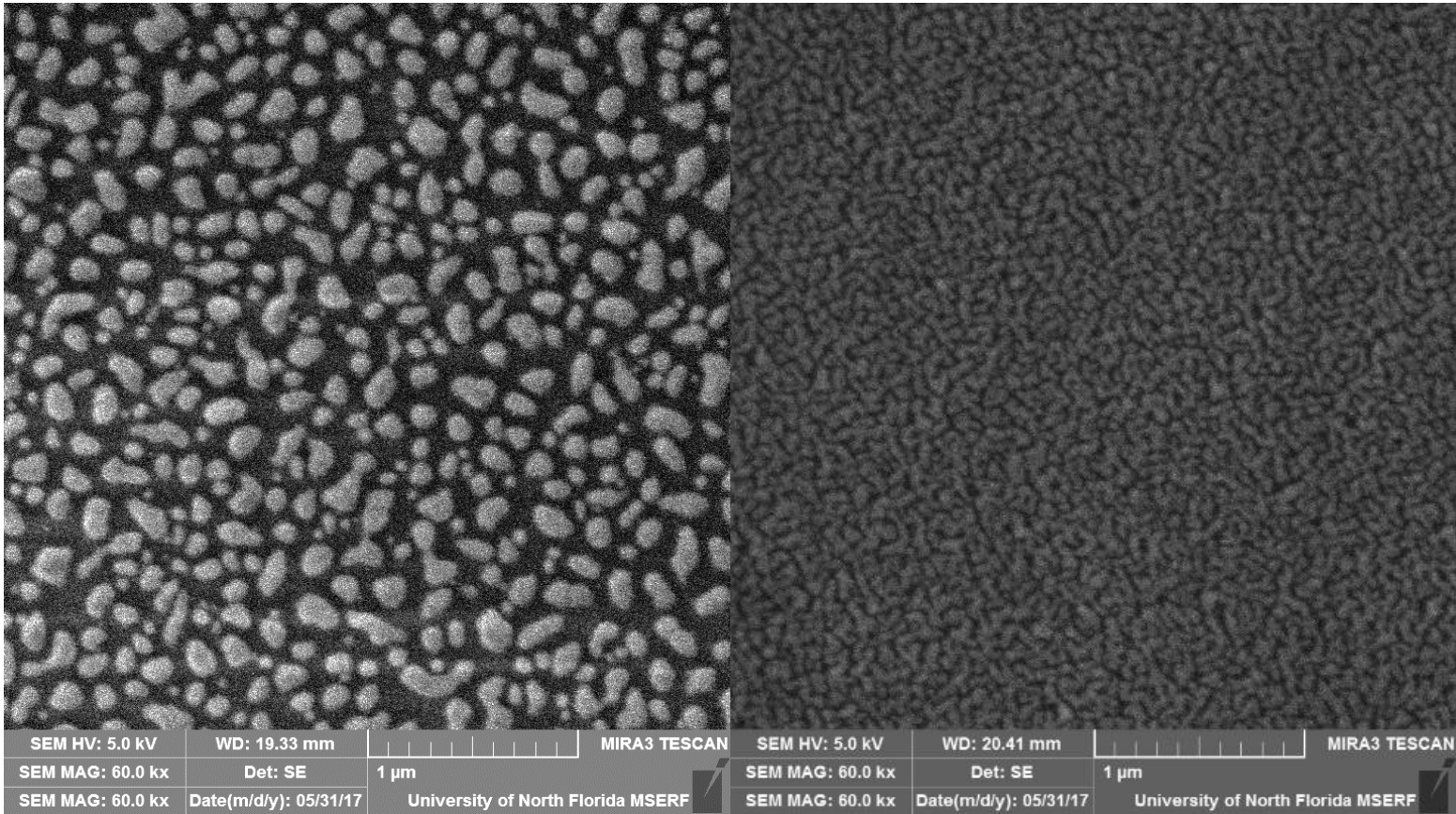
Figure 40:100nm Ag nanorods on 50nm Al seeds. After 6months storage in vacuum. Heated (left) and not heated (right)

APPENDIX E: STATISTICAL DATA FOR AVERAGE PARTICLE SIZE AND DISTANCE BETWEEN PARTICLES

Nanorod Length	Average Particle size after heating (nm^2)	STDev size	STD Error	N	Max	Min
10	3651	3365	160	442	25110.05	11.898
25	7269	5446	376	210	33783.46	59.488
25	6454	5175	165	986	44165.27	169.997
50	26492	20053	2680	56	93503.87	618.679
50	21911	14435	439	1082	79598.16	379.491
100	33569	33970	4757	51	166888.2	358.266
100	38016	32797	2078	249	163503.3	33.999
200	49838	49614	9548	27	225820.6	1958.381
200	49909	39307	2955	177	222594.3	237.996
Nanorod Length	Average distance between particles after heating (nm)	STDeviation	STD Error	N		
10	101.94	18.47	0.88	442		
25	150.49	29.29	2.02	210		
25	167.29	28.59	0.91	986		
50	290.54	53.32	7.12	56		
50	269.14	40.10	1.22	1082		
100	310.97	76.00	10.64	51		
100	334.78	62.77	3.98	249		
200	404.66	99.71	19.19	27		
200	385.04	61.83	4.65	177		

APPENDIX F: RAMAN DATA FOR VACUUM STORAGE

Normalized Enhancement			
765 WaveNumbers			
Date	HAir	NHAir	HVac	NHVac
9/29/2016	12.80%	24.11%	3.01%	1.02%
10/5/2016	6.27%	16.17%	7.53%	0.82%
10/14/2016	12.48%	29.31%	5.30%	1.34%
10/21/2016	15.53%	27.22%	7.57%	8.28%
11/1/2016	9.29%	22.63%	9.29%	22.63%
1352 WaveNumbers			
Date	HAir	NHAir	HVac	NHVac
9/29/2016	16.35%	36.12%	2.98%	0.53%
10/5/2016	9.34%	28.46%	11.49%	0.24%
10/14/2016	22.54%	43.73%	6.90%	1.18%
10/21/2016	22.99%	49.23%	9.99%	13.15%
11/1/2016	17.23%	40.63%	17.23%	40.63%
1640 WaveNumbers			
Date	HAir	NHAir	HVac	NHVac
9/29/2016	20.04%	49.75%	3.97%	1.02%
10/5/2016	12.86%	39.83%	15.76%	0.46%
10/14/2016	33.35%	64.90%	8.74%	1.56%
10/21/2016	29.85%	78.29%	12.76%	18.49%
11/1/2016	25.04%	55.58%	25.04%	55.58%

765 WaveNumbers Enhancement Normalized
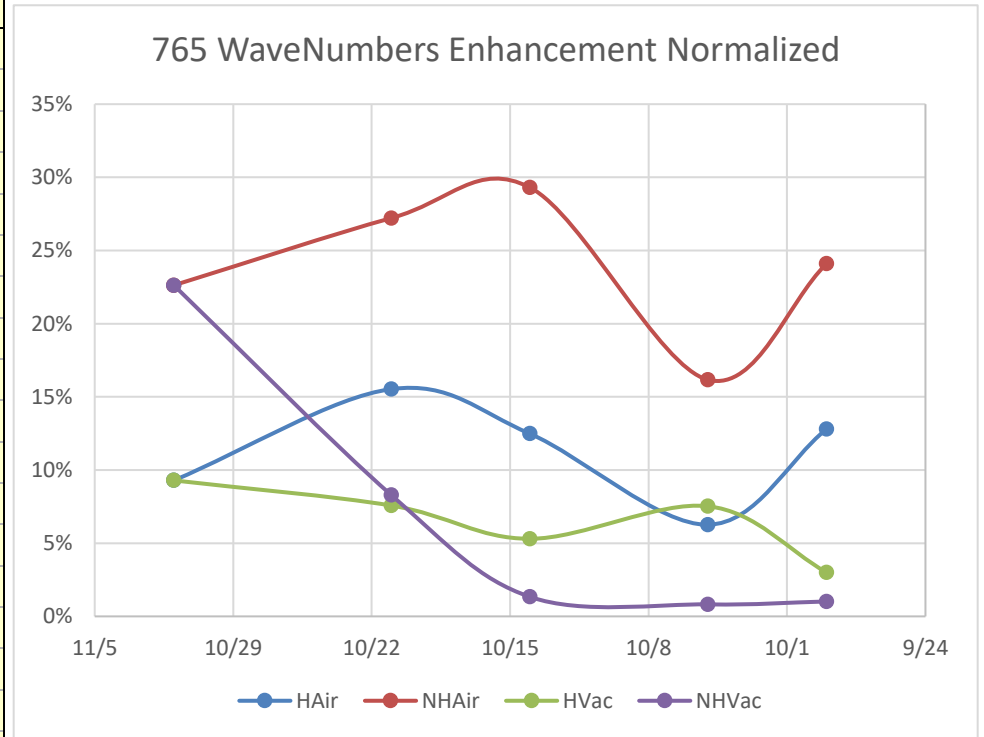
Normalized Intensity				
765 WaveNumbers				
Date	HAir	NHAir	HVac	NHVac
9/29/2016	0.933529	0.752234	0.999876	0.999336
10/5/2016	0.992818	0.774358	0.99673	0.99916
10/14/2016	0.982413	0.655446	0.99581	0.994792
10/21/2016	0.96009	0.721883	0.952386	0.995731
11/1/2016	0.978514	0.856981	0.978514	0.856981
1352 WaveNumbers				
Date	HAir	NHAir	HVac	NHVac
9/29/2016	0.990011	1	0.747832	0.661989
10/5/2016	0.743548	1	0.744996	0.602181
10/14/2016	0.935018	0.976874	0.779112	0.708103
10/21/2016	0.966028	0.991504	0.80662	0.979563
11/1/2016	0.809129	1	0.809129	1
1640 WaveNumbers				
Date	HAir	NHAir	HVac	NHVac
9/29/2016	0.862134	0.935354	0.554908	0.481504
10/5/2016	0.562018	0.938372	0.55649	0.405722
10/14/2016	0.80804	0.97705	0.601277	0.522364
10/21/2016	0.785321	0.971437	0.623623	0.824449
11/1/2016	0.652254	0.903643	0.652254	0.903643

765 WaveNumbers Normalized Intensity
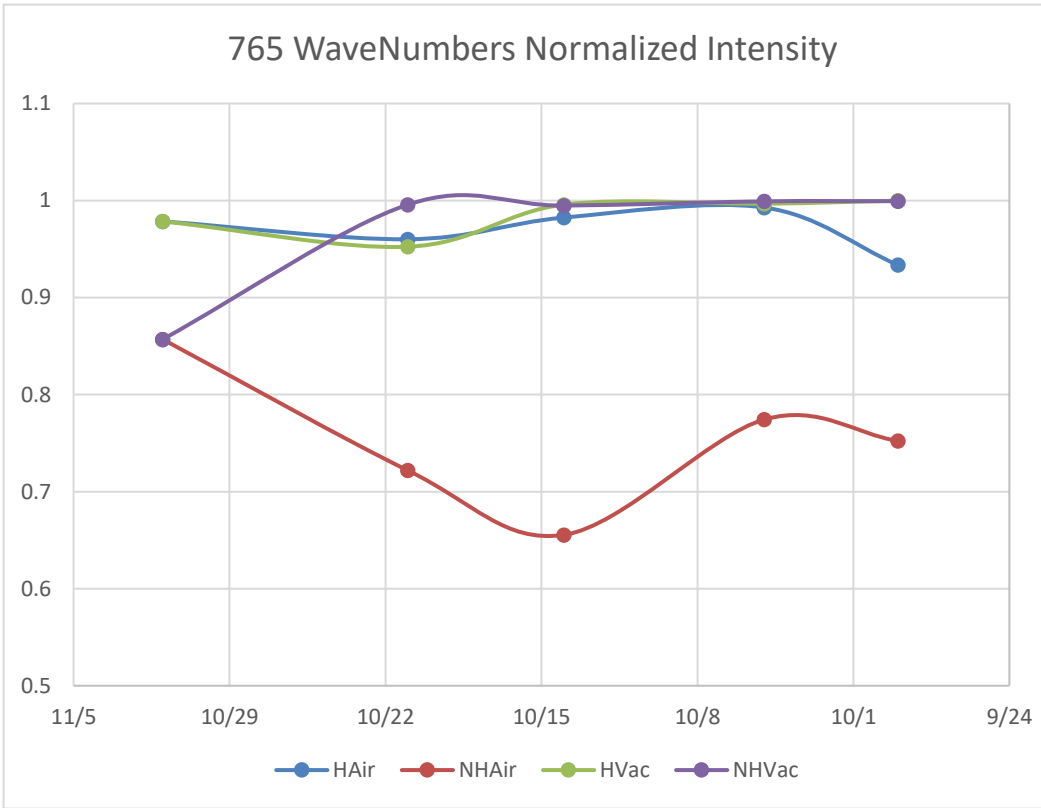
Raw Counts				
765 WaveNumbers				
Date	HAir	NHAir	HVac	NHVac
9/29/2016	15944.58	10856.53	24151.4	12161.55
10/5/2016	26251.8	18166.66	25399.98	22286.88
10/14/2016	29525.42	14948.28	28259.66	14154.36
10/21/2016	11651.21	12786.42	17734.16	8438.126
11/1/2016	23509.4	31829.3	23509.4	31829.3
1352 WaveNumbers				
Date	HAir	NHAir	HVac	NHVac
9/29/2016	16834.38	14210.14	18738.94	8809.394
10/5/2016	20389.13	22803.26	19579.7	14512.34
10/14/2016	27993.9	21825.62	22676.18	10564.74
10/21/2016	11712.88	17249.34	15020.44	8315.51
11/1/2016	19929.36	36577.3	19929.36	36577.3
1640 WaveNumbers				
Date	HAir	NHAir	HVac	NHVac
9/29/2016	14886.56	13410.54	14567.82	7000.622
10/5/2016	16121.96	21422.22	15305.28	10663.04
10/14/2016	24591.96	21941.66	18138.06	8204.046
10/21/2016	9764.876	16996.26	11928.59	7122.664
11/1/2016	16647.66	33386.82	16647.66	33386.82

765 WaveNumbers Counts
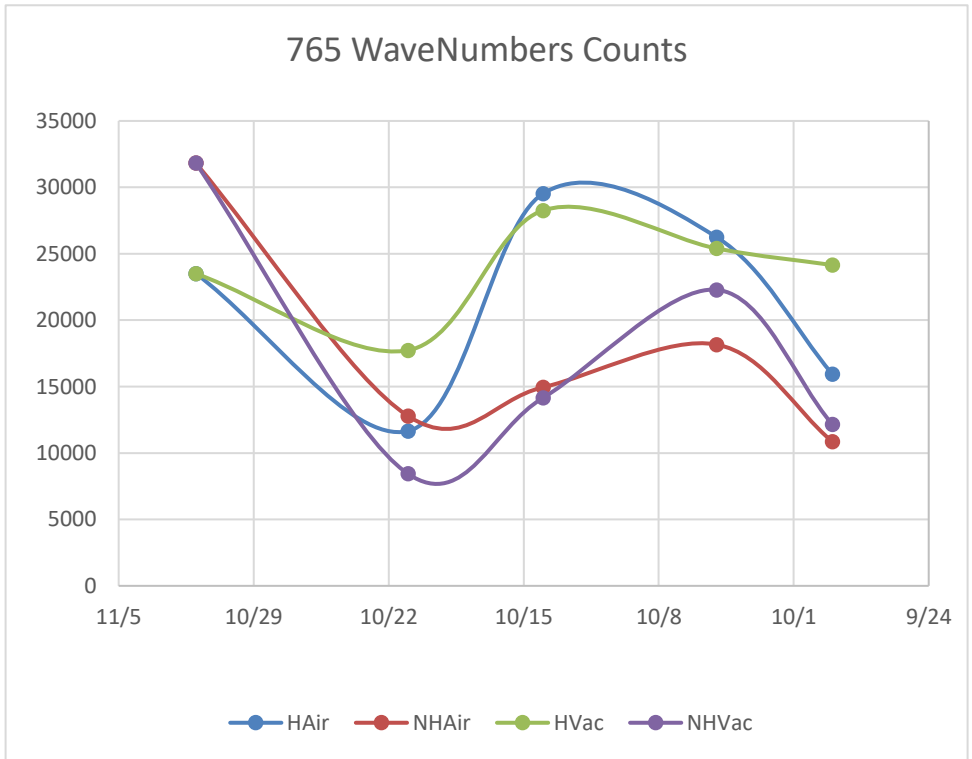
VITA

Ryan Scherzer started his undergraduate studies at the University of North Florida in the fall of 2011. During his senior year, he decided to continue his education and apply to the mechanical engineering graduate program at UNF and started in the fall of 2015. During this graduate program, he performed the research contained in this thesis and has become Author or co-author on multiple submitted journal articles pertaining to his research and is the co-inventor of two provisional patents related to 3d printing